Computational modeling of hepatic blood flow in Fontan circulations

The influence of respiration

S.F.S. van der Woude

TU Delft

Graduation report

Computational modeling of hepatic blood flow in Fontan circulations

The influence of respiration

By

Séline van der Woude

in partial fulfilment of the requirements for the degree of

Master of Science
in Biomedical Engineering

at the Delft University of Technology,
to be defended publicly on Monday September 21st, 2020 at 2.00 PM

Student number: 1543393

Supervisors:	Dr. ir. J.J. Wentzel	Erasmus University MC
	Prof.dr. P.J. French	TU Delft
Thesis committee:	Dr. ir. J.J. Wentzel	Erasmus University MC
	Prof.dr. P.J. French	TU Delft
	Prof. dr. S. Kenjereš, Dipl.-Ing.	TU Delft
	Dr. A.A.W. Roest, pediatric cardiologist	LUMC
	Dr.ir. A. Bossche	TU Delft

My master thesis project is part of a large collaborative project (better known as the TOP-FLOW project) between Department of Cardiology, Biomechanics laboratory, at Erasmus MC Rotterdam , the Pediatric Cardiology Department at Leiden University Medical Center and the Department of Chemical Engineering at the faculty of Applied Sciences of Delft University of Technology.

Acknowledgement

First and foremost, I would like to thank my daily supervisor Dr. ir. J.J. Wentzel of the Department of Cardiology, Biomechanics laboratory, at Erasmus MC Rotterdam for providing me with the opportunity to do an internship in the field of computational fluid dynamics on congenital heart defects. Your enthusiasm and passion for science and engineering is contagious. Thank you for believing in me, your kindness, technical discussions and guidance throughout this master thesis project.

Dear Prof. dr. P.J. French of the Department of Microelectronics at Faculty of Electrical Engineering, Mathematics, and Computer Science of Delft University of Technology, thank you for being my TU Delft supervisor. I am grateful for the continued accessible support. Thank you for always being there for me.

Dear Dr. A.A.W. Roest of the Pediatric Cardiology Department at Leiden University Medical Center, thank you for your clinical judgments in this project. Your expertise and our regular meetings have enormously contributed to this master thesis.

Dear Prof. dr. S. Kenjereš, Dipl.-Ing. of Department of Chemical Engineering at the faculty of Applied Sciences of Delft University of Technology, thank you for sharing your computational modeling knowledge during the TOP-FLOW meetings.

Dear Dr.ir. A. Bossche of the Department of Microelectronics at Faculty of Electrical Engineering, Mathematics, and Computer Science of Delft University of Technology, thank you for being a master thesis committee member.

Dear Drs. F.M. Rijnberg of Departments of Cardiothoracic Surgery and Pediatric Cardiology at Leiden University Medical Center, I appreciate your incredibly dedicated efforts on this TOP-FLOW project. I think our corporation was very fruitful. Keep up the great work.

Dear Dr.ir. S.A. Korteland of the Department of Cardiology, Biomechanics laboratory, at Erasmus MC Rotterdam, thank you for your technical support on programming challenges.

Dear Dr.ir. F.J.H. Gijsen of the Department of Cardiology, Biomechanics laboratory, at Erasmus MC Rotterdam, thank you for sharing your expertise and thoughts on computational fluid dynamics issues.

I would also like to thank Gaëlle Marzin, Duco Gaillard, Dr.ir. P. Eslami, Dr.ir. G. De Nisco and Ir. J.F. Juffermans for their consultations and recommendations.

Lieve Mam en Pap, dank voor jullie onvoorwaardelijke steun en dat jullie altijd achter mijn keuzes hebben gestaan, ook toen ik zei dat ik nog een tweede master wilde gaan doen. Van jullie heb ik geleerd dat je met hard werken en in jezelf blijven geloven, alles kan bereiken.

Lieve Thaïsa en Bram, dank dat ik altijd bij jullie terecht kon ook als het even tegen zat en jullie mij dan weer konden opvrolijken zodat ik weer met volle moed verder kon.

Lieve Eline, dank voor jouw steun en dat je mij altijd wilde helpen met het structuren van mijn gedachten. Je hebt ontzettend veel betekend voor mij in dit afstudeerproject.

Summary

The Fontan procedure is the last of three stages of congenital heart surgery to treat children born with a single ventricle heart defect. During the Fontan procedure, the inferior vena cava is connected to the pulmonary arteries by a Fontan tunnel. In these patients, a balanced hepatic blood flow distribution (HFD) towards both lungs is important, since a lack of "hepatic factor" has been associated with the formation of pulmonary arteriovenous malformations (PAVMs). PAVMs are dysfunctional regions in the lungs resulting in poor blood oxygenation, causing hypoxia, cyanosis, and exercise intolerance. With imaging modalities and using computational fluid dynamics, the hepatic blood flow distribution can be studied.

Recent computational fluid dynamic (CFD) studies indirectly quantify HFD to the lungs' left and right pulmonary arteries by tracking 'hepatic flow' particles that are uniformly seeded in the Fontan tunnel and analyzing the distribution of these particles towards both lungs (*conventional approach*). However, this conventional approach is based on an unvalidated assumption that there is a uniform distribution of hepatic blood in the Fontan tunnel. Since Reynolds numbers in the Fontan circulation are low and thus mixing of blood flow from the hepatic veins and blood flow from the inferior vena cava (IVC) in the Fontan tunnel might be far from optimal, the question is whether this assumption is valid. Therefore, this study aimed to investigate the distribution of hepatic blood flow in the Fontan tunnel.

To achieve this, we created three-dimensional (3D) reconstructions of the patient-derived Fontan circulations based on MRI imaging that included the geometry of the hepatic veins in the computational fluid domain. CFD modeling was used to analyze the mixing between hepatic and IVC blood flow in two cross-sections at a downstream (i.e. caudal) and an upstream (i.e., caudal) level within the Fontan tunnel. One of the objective was to quantify HFD using particle tracking directly from the inlets of the hepatic veins (*novel approach)* and compare these HFD results to the conventional and previously published HFD quantification approach's outcomes. In **part A1** of this master thesis, we performed CFD simulations of 15 Fontan patients and only considered the cardiac cycle effects on blood flow. The main finding of part A1 was that hepatic blood flow was non-uniformly distributed within the Fontan tunnel. This non-uniform distribution was most noticeable in the caudal cross-section (just above the junction of hepatic veins with the IVC). There was a significantly higher degree mixing of hepatic with IVC blood flow at the cranial level (good mixing, mean 0.79±0.11) than at the caudal level in the Fontan tunnel (moderate mixing, mean 0.66±0.13, $p<0.001$). Furthermore, a significant mean absolute difference was found in HFD quantification between the conventional method, in which hepatic blood flow particles are uniformly seeded from a *caudal* cross-section in the Fontan tunnel, and the novel method, in which particles are directly seeded from the level of the hepatic veins (4.6% (95%CI 3.1-6.0)). Additionally, the mean absolute difference between the conventional HFD quantification approach, in which particles were seeded from a *cranial* cross-section, and the novel HFD quantification approach was 4.4 % (95%CI 2.2-6.5). However, although significant, these variations between the conventional and novel HFD quantification approaches were relatively small and had no clinical relevance at a

group level. Nevertheless, it should be emphasized that differences can be as high as 14.9% on an individual basis, which may have implications for the patient-specific decision-making about the need for surgical intervention.

Similar to most previous CFD models, in part A1 the respiratory effects on venous blood flow were not taken into account in the CFD simulations. However, the physiologic influence of respiration could have an important impact on the Fontan hemodynamics. Previous clinical imaging studies showed that respiration has a tremendous impact on the blood flow in the hepatic veins and Fontan tunnel in Fontan patients. These papers revealed that the flow rates in the Fontan tunnel and hepatic veins increased dramatically during inspiration, then decreased during expiration. Furthermore, these clinical imaging studies concluded that respiration was primarily responsible for the periodic flow rate changes (i.e., pulsatility) in the Fontan tunnel and hepatic veins in Fontan patients. Therefore, **in part B1** of this master thesis, we also evaluated the respiratory effects on the blood flow in three Fontan patients using real-time phase-contrast magnetic resonance imaging (PC-MRI). Even though the resolution of real-time PC-MRI is not yet good enough for the hepatic flow quantification, in this master thesis, we introduced a novel approach to indirectly measure the hepatic flow in the hepatic veins during the respiratory cycle using real-time PC-MRI. First, we measured the blood flow in the Fontan tunnel, just above the entrance of the hepatic veins. Second, we derived the IVC blood flow caudal from the hepatic veins. By subtracting these mean flows, we indirectly quantified the mean hepatic blood flow. This is the first work that used real-time PC-MRI for indirect quantification of hepatic flow to the best of our knowledge. For the sake of clarity, in part B1 we only conducted an in-depth flow analysis without the use of CFD. The key findings of part B1 were that the hepatic blood flow was 3.53 to 4.88 times higher during the inspiratory phase than during the expiratory phase. The flow in the Fontan tunnel was 1.82 and 1.97 times higher during inspiration than during expiration. Furthermore, hepatic backflow (i.e., the flow that is moving away from the heart towards the liver) only occurred during expiration. Another interesting finding was that the hepatic blood flow and Fontan tunnel flow were respectively for 56.0% up to 66.0% and 29.2% up to 32.7% dependent on inspiration. These outcomes showed that the blood flow in the hepatic veins and Fontan tunnel were heavily influenced by respiration. Furthermore, these derived hepatic flow parameters using real-time PC-MRI were in close agreement with the Doppler measurements of Hsia et al. Although future research needs to elucidate the potential of deriving hepatic blood flow from real-time PC-MRI on a clinically routine basis, this study showed the feasibility of evaluating hepatic blood flow in Fontan patients while using real-time PC-MRI.

Because respiration has a pronounced effect on the flow rates in Fontan patients, it was desirable to reexamine the mixing of hepatic with IVC blood flow in the Fontan tunnel and the HFD quantification described in part A1 when respiration is taken into account. Therefore, in **part B2**, we used the same 3D reconstructions of three Fontan circulations and their corresponding meshes as used in part A1 but incorporated boundary conditions that included both the cardiac and respiratory effects on blood flow in the CFD simulations. In part B2, we concluded that hepatic blood flow was still non-uniformly mixed in the Fontan tunnel. The degree of mixing between these three cases varied between 0.56-0.76 at the caudal level and between 0.68-0.94 at the cranial level. Although we could not perform statistical analysis, it seemed that respiration improved the overall degree of mixing between hepatic and IVC blood flow in the Fontan tunnel when comparing the findings of individual cases of part B2 to the

results of part A1 An explanation for this finding could be that respiration causes more flow pulsatility and from previous research, it is known that pulsatile flow can improve the mixing between two separate laminar streams, as we find in the Fontan circulation. In addition to the mixing assessment, differences up to 8.97% were found in HFD between the conventional and novel HFD quantification methods in the CFD models that considered respiration. Since part B2 only investigated three cases, more research is needed using the novel HFD quantification method in patient-specific CFD models that incorporate the hepatic veins to evaluate respiratory effects on the HFD.

Recent CFD studies quantify HFD by tracking massless particles that represent the hepatic blood flow. This methodology is generally known as the Lagrangian particle tracking method. Generally, we used the Lagrangian particle tracking approach for the mixing analyses and HFD quantifications in this master thesis since this method is the golden standard for HFD quantification in Fontan patients and widely used by other research groups. However, a pilot study by Prof. Dr. S. Kenjereš showed that the quantification of mixing between hepatic and IVC in the Fontan tunnel and HFD can also be evaluated with convection-diffusion modeling (The Eulerian method). The Eulerian method uses the concentration of particles and computes the overall convection and diffusion of a number of particles. Since we wanted to explore the efficiency of the Eulerian method, we compared the HFD values obtained from the Lagrangian and Eulerian method for one similar CFD case that incorporated the respiratory effects on blood flow in part B2. For both the Lagrangian and the Eulerian method, we used the hepatic veins inlet as the starting point for HFD quantification. Although we did not perform an assessment of mixing between hepatic and IVC flow within the Fontan tunnel using the Eulerian method, the HFD difference for this single case between the Lagrangian and Eulerian method was only 0.62 %. This almost identical result between both methods implies that the Eulerian method could be used as an alternative for HFD quantification; however a larger study is needed to confirm this finding.

Conclusion

In brief, the hepatic blood flow was non-uniformly distributed within the Fontan tunnel in both types of CFD models that ignored and considered respiration. This non-uniform distribution was most noticeable in the caudal cross-section of the Fontan tunnel (just above the junction of the hepatic veins with the IVC). Furthermore, both kinds of CFD models showed a substantial difference in HFD between the conventional method, in which hepatic blood flow particles are uniformly seeded from either a caudal or cranial cross-section within the Fontan tunnel, and the novel method, in which particles are directly seeded from the level of the hepatic veins. Additionally, we have demonstrated that it was feasible to indirectly measure hepatic blood flow in Fontan patients while using real-time PC-MRI. These derived flow parameters extracted from real-time PC-MRI acquisitions showed that the blood flow in the hepatic veins and Fontan tunnel were tremendously influenced by respiration. Hopefully, these novel insights will contribute to a better understanding of the hepatic flow distribution patterns and the role of respiration on blood flow in Fontan patients with the ultimate goal of providing better patient care in the future.

Contents

List of Abbreviations

2D PC-MRI	Two-dimensional phase-contrast magnetic resonance imaging in which velocity is encoded in one direction: the through-plane direction
2D-3dir PC-MRI	Two-dimensional phase-contrast magnetic resonance imaging with three directional velocity encoding
CFD	Computational fluid dynamics
ECC	Extracardiac total cavopulmonary connection
ECG	Electrocardiogram
HFD	Hepatic flow distribution
ILT	intracardiac total cavopulmonary connection (i.e., intracardiac lateral tunnel)
IVC`	Inferior vena cava
LPA	Left pulmonary artery
N-S	Navier-Stokes
PC-MRI	phase-contrast magnetic resonance imaging
RPA	Right pulmonary artery
SVC	Superior vena cava
TCPC	Total cavopulmonary connection

1. General introduction

1.1 Normal cardiovascular system

The cardiovascular system is a network of blood vessels in the human body with the primary function of providing the body with nutrients and oxygen, eliminating carbon dioxide and waste products and regulating the temperature. The heart is the main pump that drives the blood through the body using a sophisticated system of arteries, arterioles and capillaries. After passing the organs, the blood flows back to the heart via the venules and veins. The human cardiovascular system can be divided into two sub-circulations: 1. The pulmonary circulation which transports deoxygenated blood to the lungs and returns oxygenated blood from the lungs to the heart, 2. The systemic circulation that is responsible for the transport of the oxygenated blood through the rest of the body. A healthy heart has a left and right side (figure 1A). Both sides of the heart contain an atrium and ventricle; hence a healthy heart has four chambers. The atria collect the blood and pump it to the more muscular ventricles. The left and right ventricles of the heart function as a double pump. The right ventricle that is part of the pulmonary circulation pumps the blood into the pulmonary arteries to the lungs. The left ventricle that is part of the systemic circulation pumps the blood in the aorta that transports the blood to the rest of the body[1].

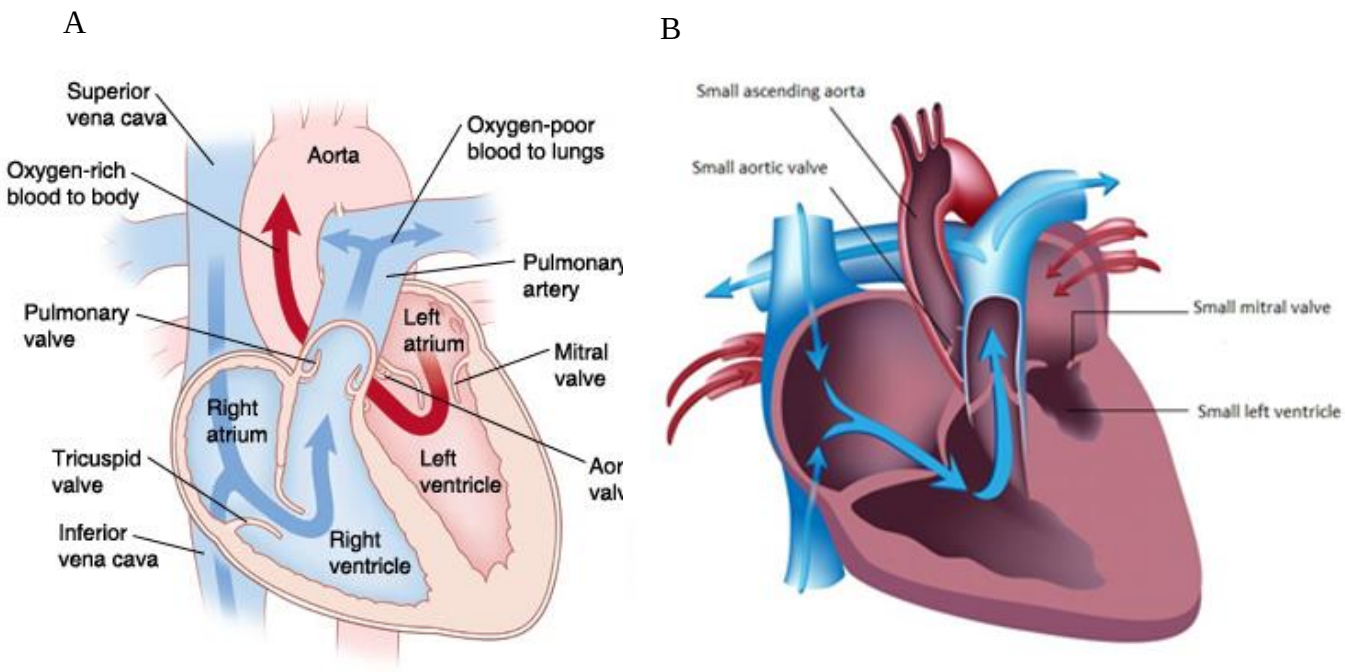

Figure 1A: Normal anatomy of the heart, 1B: Single venricle heart defect (hypoplastic left heart syndrome). *Available via http://fetaltonewborn.org/hypoplastic-left-heart-syndrome-hlhs/normalheartbloodflow/ and https://biomedadvances.com/hypoplastic-left-heart-syndrome-genes-identified/*

1.2 Single Ventricle Heart Defect

Around 0.2% of all children are born with a single ventricle heart defect[2]. Single ventricle heart defects are among the most severe categories of congenital heart diseases. In patients with a single-ventricular heart defect, one of the ventricles is not developed correctly, which results in inadequate or no pumping of blood to one of the two sub-circulations (figure 1B). The most common single heart defect is the hypoplastic left heart syndrome, in which the left ventricle is underdeveloped[3]. Besides, patients with single heart defects may also have openings in the atrial or ventricular wall. The shunts between the left and the right heart chambers cause mixing of the oxygen-poor blood and oxygen-rich blood. Because of these anatomical problems of the heart, shortly after birth newborns with a single heart defect turn cyanotic (present with a blue color skin) due to decreased amounts of oxygenated blood in the body [3].

1.3. Three-stage reconstruction

Without surgical treatment and medicines, most of the children with a single ventricle heart defect die within the first 7-10 days of life[4]. Fortunately, advances in surgery, medicine and intensive care treatment allow most patients to survive nowadays. Since the dysfunctional ventricle cannot be repaired, surgeons reconstruct parts of the heart and redirect blood flows to palliate the adverse effects of a single ventricle defect. This surgical reconstruction has to be performed in three stages since there is a need for well-controlled blood flow to the small lungs of the neonates to prevent damage to the lungs. This three-staged surgical reconstruction allows a gradual adaptation of the lungs and heart of pediatric patients, which decreases the overall perioperative morbidity and mortality[3].

1.3.1. Stage 1: Norwood procedure

The first stage of the reconstruction is the Norwood procedure, which is performed shortly after birth (figure 2). This surgical reconstruction allows the right ventricle to pump blood to both the lungs and the body. First, the surgeons enlarge the opening between the left and right atrium (which is generally known as atrial septectomy), which enables the blood from the right and left atrium to mix. The next step is to widen the hypoplastic aorta. Hereafter, the trunk of the pulmonary artery is separated from the pulmonary circulation, and incisions are made within the aorta and the pulmonary artery. Hereafter, the aorta and the pulmonary artery are stitched together with a patch to create a 'neo-aorta'. At this moment, there is a pathway generated from the heart to the body. The final step is to ensure that there is also blood flow to the lungs by creating an additional tube. There are two options for this final step: 1. The Sano shunt, which is an additional tube from the right ventricle to the remaining pulmonary artery (which has not been used for the 'neo-aorta'), 2. The Blalock-Taussig shunt, which is an additional tube from the 'neo-aorta' to the pulmonary artery. Both options ensure blood supply to the lungs. After the Norwood procedure, the right ventricle not only pumps blood to the lungs, but it also pumps blood to the rest of the body[5]. However, because the right ventricle pumps the blood to the lungs and the aorta, the arterial oxygen saturation after the Norwood procedure is usually 70-75% (healthy values 90-95%).

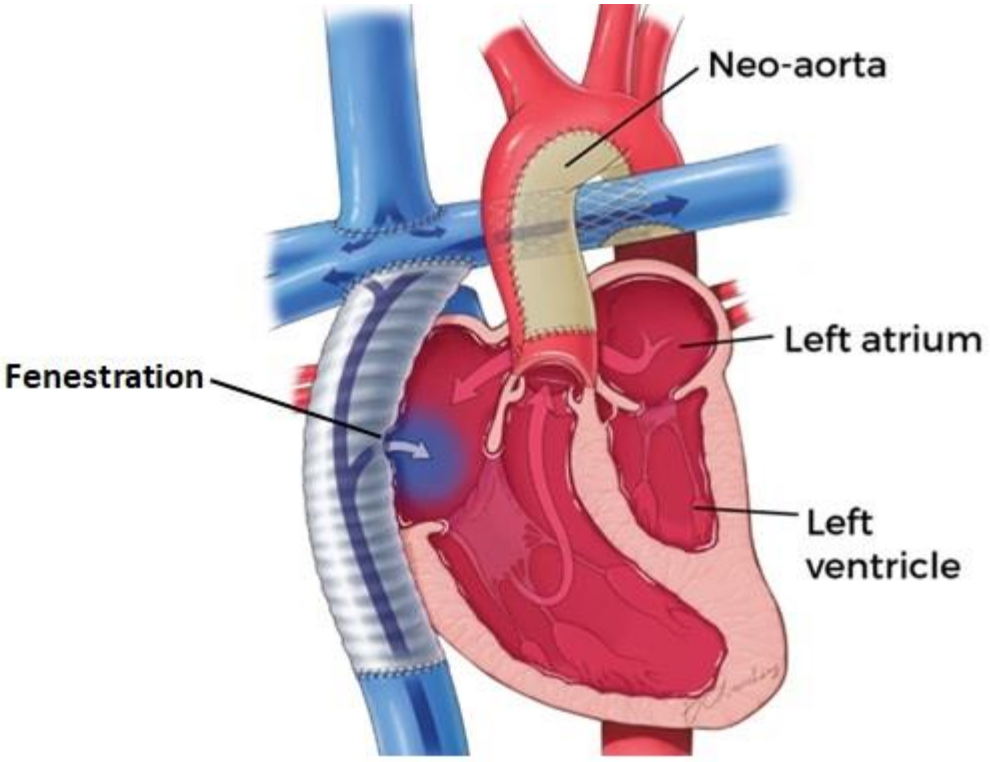

Figure 2: Norwood procedure *Available via: https://www.childrenscolorado.org/conditions-and-advice/connection/hypoplastic-left-heart-syndrome-hlhs/hlhs-surgery/*

1.3.2. Stage 2: Bi-directional Glenn procedure

Around four to six months after the Norwood procedure, the second stage of the reconstruction is carried out, which is called the bi-directional Glenn procedure (figure 3). The bi-directional Glenn procedure has two goals: 1. To reduce the amount of blood the right ventricle has to pump and 2. To enable passive blood flow from the upper body to the lungs. In this procedure, the superior vena cava (SVC) from the upper part of the body is detached from the heart and directly connected to the (right) pulmonary artery. The additional tube between the right ventricle and pulmonary artery (Sano shunt) or between the 'neo-aorta' and pulmonary artery (Blalock-Taussig shunt), placed during the Norwood procedure, is removed since the blood can now pass to the lungs via the anastomosed SVC. This second reconstruction already improves the systemic arterial oxygen saturation with usual oxygen saturations around 75-85 percent[6]. After the bi-directional Glenn procedure the right ventricle pumps blood only to the body. The blood in the right ventricle after a bi-directional Glenn procedure is still a mixture of deoxygenated blood coming from the lower part of the body via the vena cava inferior (IVC) and oxygenated blood that has entered the ventricle via the pulmonary veins and atria[7].

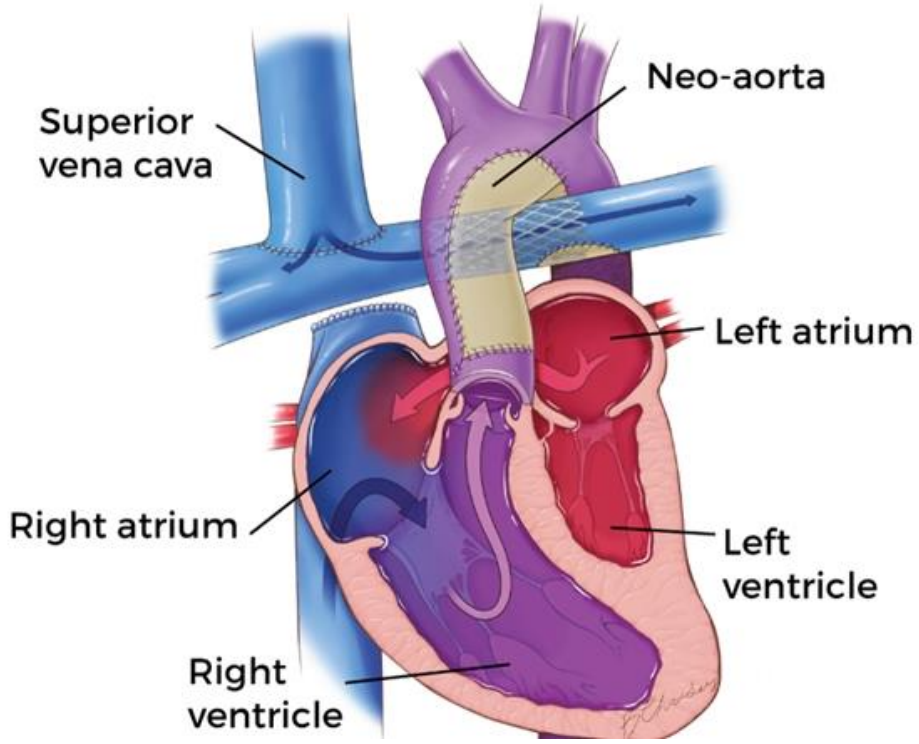

Figure 3: Bi-directional Glenn procedure *Available via: https://www.childrenscolorado.org/conditions-and-advice/connection/hypoplastic-left-heart-syndrome-hlhs/hlhs-surgery/*

1.3.3. Stage 3: Fontan procedure

The third stage of the three-stage palliative reconstruction is the Fontan procedure (figure 4), for the first time performed by Francis Fontan in 1971. In the Fontan procedure, normally completed between the ages of 18 months and four years, the IVC is detached from the heart and connected directly to pulmonary arteries by a Fontan tunnel. In a Fontan circulation, the venous blood from the upper and lower part of the body (via SVC and IVC, respectively) returns straight to the lungs to picks up oxygen (without the support of a ventricle) while the single functional ventricle is used for pumping the blood through the body[3,8]. This Fontan procedure achieves a single-ventricle circulation with saturations of near-normal levels[4]. Initially, the surgeons make a fenestration during the Fontan procedure, as illustrated in figure 4A. A fenestration is a little open connection between the Fontan tunnel and the right atrium. A fenestration is a sort of piston that prevents the development of too high pressures in pulmonary arteries, directly after the Fontan procedure. When the child becomes older, the fenestration is usually closed by a catheterization procedure[9]. The Fontan circulation without fenestration is shown in figure 4B.

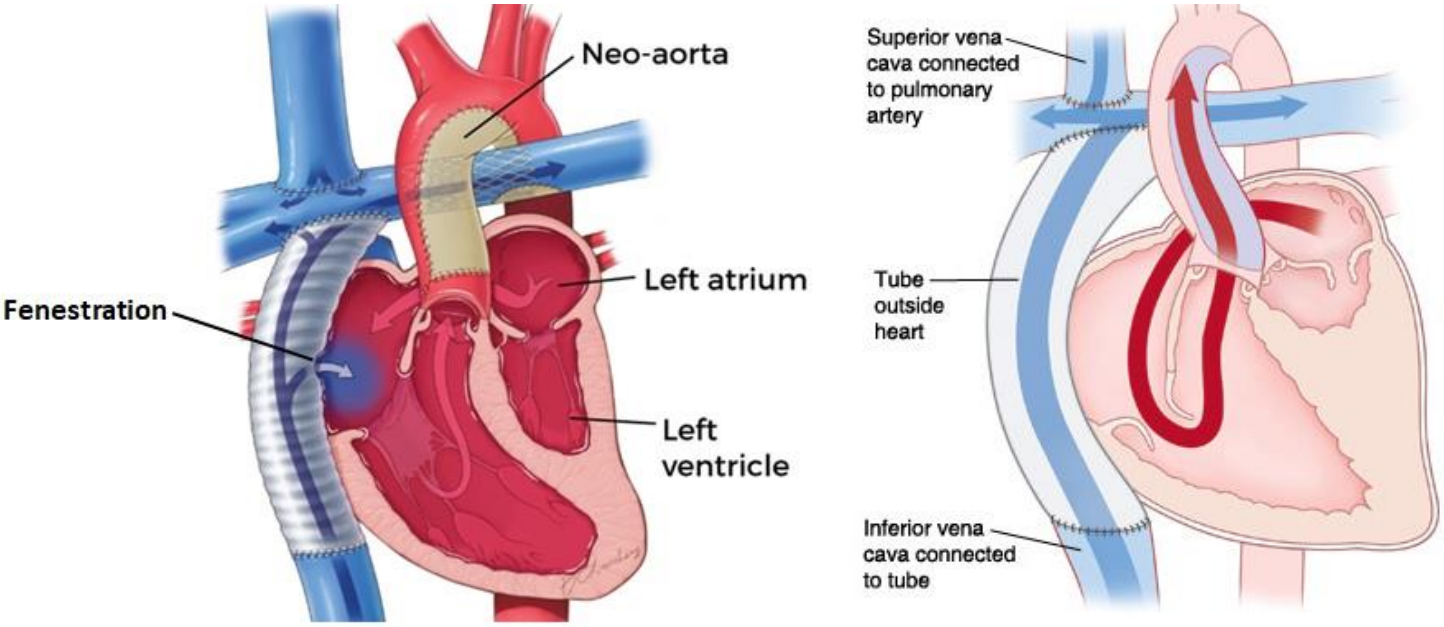

Figure 4: 4A: Fontan procedure, 4B: After Fontan procedure after closure of fenestration *Available via: https://www.childrenscolorado.org/conditions-and-advice/connection/hypoplastic-left-heart-syndrome-hlhs/hlhs-surgery/*

1.3.4. Surgical variations for the Fontan procedure

There are three surgical variations for the Fontan procedure that have been evolved over time: 1. The atriopulmonary connection (i.e. 'the classic Fontan), 2. intracardiac total cavopulmonary connection (i.e., intracardiac lateral tunnel (ILT)); and 3. extracardiac total cavopulmonary connection. In its first version, the atriopulmonary connection (figure 5A), the right atrium was isolated and anastomosed to the right pulmonary artery. This atriopulmonary connection was an attempt to utilize the right atrium as right ventricle to pump the blood to the lungs[3]. However, a major drawback of the atriopulmonary connection was the progressive dilation of the atrial chamber that causes blood flow turbulence and blood clotting problems. After that, Leval et al. invented the ILT-type connection. In this ILT method (figure 5B), the IVC is coupled to the pulmonary arteries via an isolated intra-atrial lateral tunnel constructed with native tissue (the right atrial posterior wall) and prosthetic material[10]. The idea behind the ILT connection is that it would prevent progressive dilation of the atrium. The extracardiac total cavopulmonary connection (ECC) (figure 5C) makes use of a conduit that is entirely located outside the atrium and attaches the IVC to the pulmonary arteries[11,12]. It is assumed that the ECC provides more favorable fluid dynamics with lower right atrial pressures and lower risk of thromboembolism due to the absence of prosthetic material in the atrium compared to the ILT method. Therefore, most pediatric cardiology centers use the ECC method nowadays[12]. Both the ECC and ILT connections are generally labeled as the total cavopulmonary connection (TCPC). Research has demonstrated that the TCPC, especially the ECC-variant, had lower mortality and improved outcomes compared to the old-fashion atriopulmonary connection[3].

In brief, the Fontan circulation allows venous blood to return passively to both lungs, while the single functional ventricle actively pumps the blood into the body. The returning

venous blood is generally called (systemic) venous return in literature. Venous return from the lower part of the body travels via the IVC, which is a vessel that collects venous blood from veins of different organs along its way. Figure 6 shows an overview of the Fontan circulation, including the three hepatic veins from the liver that drain into the IVC.

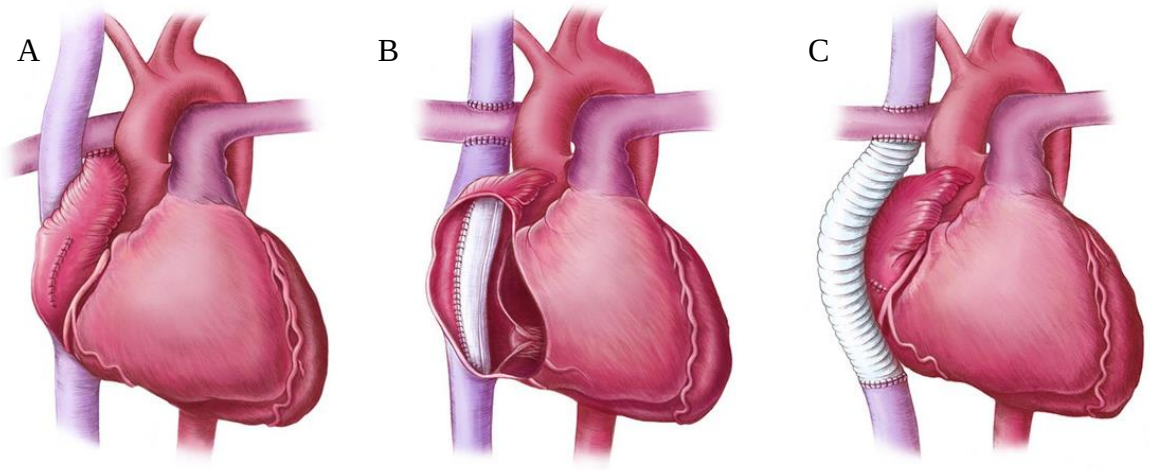

Figure 5: 5A: atriopulmonary connection, 5B: intracardiac total cavopulmonary connection (i.e. intracardiac lateral tunnel (ILT)), 5C: extracardiac total cavopulmonary connection (ECC). *Available via: https://kidshealth.org/en/parents/hypoplastic-heart.html and https://www.behance.net/gallery/56145349/Fontan-Procedure-published-in-EMJ-Cardiology*

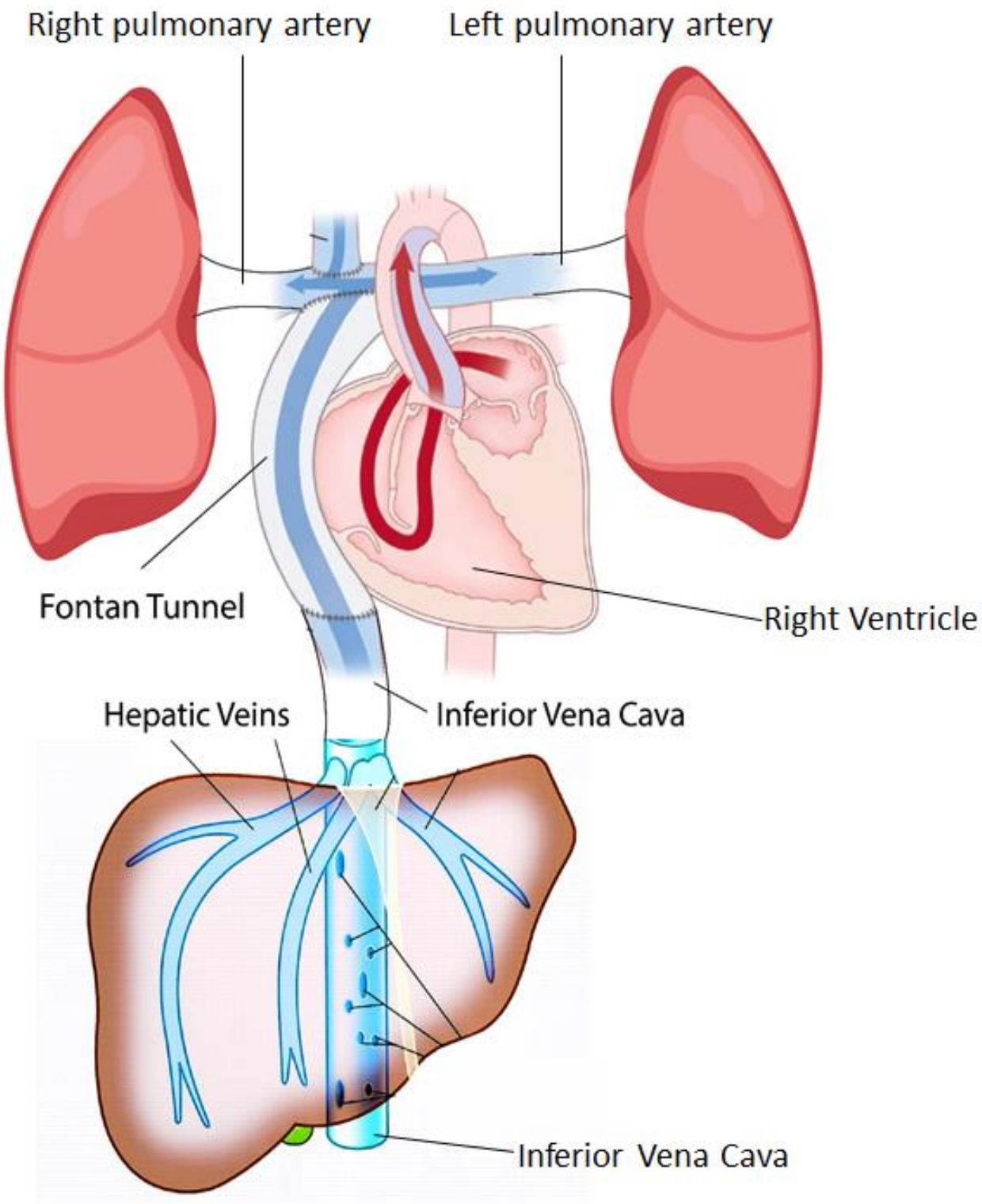

Figure 6: Overview of the Fontan circulation including the three hepatic veins from the liver that drain into the inferior vena cava

1.4. Unbalanced hepatic flow distribution

Although the Fontan procedure has been modified over time, leading to the ECC-type connection that is most in use nowadays, patients with a Fontan circulation still suffer from long-term complications. The most important long term complication is end-stage heart failure leading to exercise intolerance, pulmonary hypertension and arrythmia[11]. Another long-term complication is the development of pulmonary arteriovenous malformations (PAVMs). PAVMs are abnormal connections between the capillaries of the pulmonary arteries and pulmonary veins and are responsible for insufficient oxygenation of the blood. Insufficient oxygenation of the blood could result in progressive hypoxemia, cyanosis and exercise intolerance. The exact pathogenesis of PAVMs is still unknown, but it is assumed that hepatic blood flow contains a group of molecules 'the hepatic factors' which are crucial for the prevention of the development of PAVMs[13–15]. In other words, a lack of hepatic factors in one of the lungs is associated with PAVMs formation. The liver secretes the hepatic factors into the hepatic blood flow. The hepatic blood flow drains into IVC and is via the Fontan tunnel distributed in both lungs. In a healthy cardiovascular system, the right ventricle adequately pumps the hepatic blood flow to both lungs, however studies showed patients with a Fontan circulation usually have an unequal distribution of hepatic blood flow towards both lungs [13,15]. Therefore, the hepatic flow distribution (HFD) towards both lungs is an important parameter and used by clinicians to evaluate the Fontan performances.

Computational fluid dynamics (CFD) is a special field of fluid mechanics and can help to understand the behavior of complex fluid flows in Fontan geometries. CFD is a widely used method for retrospective and prospective patient studies to investigate unmeasurable hemodynamic parameters such as HFD[16,17]. For the quantification of HFD, you need to investigate the trajectories of individual fluid particles representing the hepatic blood flow, which is difficult to achieve in vivo. A way to overcome this obstacle is the usage of a computer model that simulates the hepatic blood flow within a Fontan circulation. Recent CFD studies indirectly quantified HFD to the left pulmonary artery and right pulmonary artery by tracking 'hepatic flow' particles that are uniformly seeded in the Fontan tunnel and analyzing the distribution of these particles towards both lungs (the *conventional approach*) [18–22]. However, this conventional approach is based on an unvalidated assumption that there is a uniform distribution of hepatic blood in the Fontan tunnel. Because Reynolds numbers in the Fontan tunnel are low, the blood flow in the Fontan tunnel behaves laminar. Due to this laminar flow behavior, the mixing of blood from the hepatic veins and the IVC might be far from optimal contrary to what is generally assumed and so the question rises whether this assumption of uniform hepatic flow distribution within the Fontan tunnel is correct. Moreover, using this assumption of even distribution of hepatic flow in the Fontan tunnel could potentially cause inaccuracies in HFD quantification. Therefore, this study aimed to test this assumption of uniform distribution of hepatic blood flow within the Fontan tunnel. To achieve this, we created patient-specific CFD models that included the geometry of the hepatic veins into the computational fluid domain. These CFD models that incorporated the hepatic veins made it possible to seed 'hepatic flow' particles directly from the level of the hepatic veins (*the novel approach*). We supposed that seeding 'hepatic flow 'particles directly from the level of the hepatic veins would provide physiologically more realistic hepatic blood flow patterns. Another objective was to quantify and compare the HFD outcomes when particles were

uniformly seeded from a cross-section within the Fontan tunnel (the conventional approach) and were seeded from the level of the hepatic veins (the novel approach).

1.5. Respiration

1.5.1. The findings of previous studies

Previously performed studies showed that the venous blood in the Fontan circulation is influenced by respiration. The venous blood flow in Fontan patients was significantly more influenced by respiration compared to healthy subjects[23,24]. Hsia et al. and Fogel et al. stated that the Fontan tunnel flow was for 30% dependent on inspiration[24,25]. Moreover, Hsia and colleagues revealed that the hepatic blood flow was for 55% dependent on inspiration[24]. Although the cardiac cycle remains the main driving force behind the net mean flow of the Fontan tunnel, it was showed that respiration was primarily responsible for the periodic flow rate changes (i.e., pulsatility) in the Fontan tunnel[24–29]. The Doppler ultrasound measurements of Hsia et al. showed that respiration was not only predominantly in charge of the flow pulsatility in the hepatic veins, but it was also the main driving force behind the hepatic blood flow[24]. Both the Fontan tunnel and the hepatic flow were significantly higher during inspiration than during expiration in Fontan patients[23–27,29–41]. It was revealed that the Fontan tunnel and hepatic flow in Fontan patients are respectively between 1.4 to 1.8 and between 3 to 4 times higher during inspiration than expiration[23,24,27,30–36,38,39,41]. Furthermore, the cardiac cycle barely affected the flow pulsatility in the Fontan tunnel and hepatic veins in Fontan patients[24,27,30,31,42]. The greater influence of respiration was explained by the fact that Fontan patients do not have a sub-pulmonary ventricle that steadily pumps the blood into the lung. Moreover, during the Fontan procedure, the surgeons create a direct connection between the IVC and the lungs by the Fontan tunnel that normal subjects do not have. Therefore, Fontan patients are more subjected to intrathoracic pressure changes related to breathing. Inspiration drops the intrathoracic pressure to negative values[43] and is considered responsible for the increased inspiratory Fontan tunnel and hepatic blood flow in Fontan patients.

1.5.2. Flow acquisitions that take respiratory effects on blood flow into account

Different clinical imaging techniques can measure blood flow while taking the respiratory effects into account. The two clinical imaging methodologies that are most commonly used for visualizing blood flow are free-breathing non-navigated non-ECG gated two-dimensional (2D) through-plane phase-contrast MRI (PC-MRI), better known as real-time PC-MRI, and Doppler Ultrasound. Real-time PC-MRI considered both *the cardiac and respiratory effects* on blood flow, which will be discussed later. PC-MRI uses an MRI scanner and radio waves that are pulsed through a body to analyze blood flow. Doppler ultrasound uses an ultrasound beam and sound waves to visualize blood moving through vessels. PC-MRI has some advantages above Doppler Ultrasound. First, PC-MRI is less dependent on the examiner and has, therefore, a higher inter-observer reproducibility[44,45]. Secondly, when using Doppler Ultrasound, assumptions about basic flow profiles and cross-sectional vessel areas, need to be made to calculate mean velocities and net flow rates. These assumptions may produce imprecise flow calculations in the presence of complicated vessel geometry or flow[46]. Unfortunately, current clinical imaging studies have only investigated the respiratory effects on hepatic blood flow

using (invasive) Doppler ultrasound [24,30,31,34–36,47,48] because hepatic veins are too small to measure these blood flow rates directly with real-time PC-MRI. Despite the fact that the resolution of real-time PC-MRI is not yet good enough for the hepatic flow distribution, in this master thesis, we introduced a new method to indirectly measure the hepatic flow in the hepatic veins during the respiratory cycle using real-time PC-MRI. First, we measured the blood flow in the Fontan tunnel, just proximal to the hepatic veins' entrance. Second, we derived the IVC blood flow caudal from the hepatic veins. By subtracting these flows, we indirectly quantified the hepatic blood flow. With this new method, we were able to investigate the respiratory effects on the blood flow of the SVC, IVC, Fontan tunnel and the hepatic veins while using real-time PC-MRI in this master thesis.

1.5.3. Respiratory effects on hemodynamics in CFD models

Respiration is a physiologic influence on Fontan hemodynamics that has unfortunately not been incorporated in most of the CFD models. The effects of respiration may have important implications for the CFD modeling outcomes, such as the degree of mixing between hepatic and IVC blood flow in the Fontan tunnel and the HFD quantification. Therefore, we developed two types of CFD models: 1. CFD models that only included the cardiac effects on blood flow (part A1) and 2. CFD models that considered both the cardiac and respiratory effects on blood flow waveforms (part B2).

Main objectives

This thesis is subdivided into three main parts: A1, B1 and B2.

Part A1

The objectives of **part A1** of the master thesis project were to 1. investigate the assumption that hepatic blood flow is uniformly distributed in the Fontan tunnel by evaluating the degree of mixing between hepatic and IVC blood flow at two cross-sections within the Fontan tunnel using patient-specific CFD simulations, and 2. quantify HFD using particle tracing directly from the hepatic veins (novel approach) and compare results with the conventional approach, in which particles were uniformly seeded from cross-sections within the Fontan tunnel (conventional approach). In part A1, we used free-breathing, ECG-gated two-dimensional PC-MRI with three-directional velocity encoding (2D-3dir PC-MRI) acquisitions to obtain time-varying flow rate waveforms to reconstruct boundary conditions in the patient-specific CFD models. The free-breathing ECG-gated 2D-3dir PC-MR imaging modality will be discussed in more detail in chapters 2 and 3, however, it is important to know that ECG-gated obtained flow data only consider *cardiac effects* on blood flow. The *hypothesis* of part A1 is that hepatic blood is non-uniformly distributed within the Fontan tunnel, which affects the precision of HFD quantification with the conventional approach.

Part B1

Part B1 involves an in-depth flow analysis without the use of CFD. In this part B1, we introduced a new method to indirectly measure the hepatic flow in the hepatic veins during the respiratory cycle using real-time PC-MRI. With this new method, we were able to investigate

the respiratory effects on the blood flow of the SVC, IVC, Fontan tunnel and the hepatic veins while using real-time PC-MRI. The main hypothesis was that respiration would have a pronounced impact on the flow rates of the hepatic veins in the Fontan patients.

Part B2

Since we only considered the cardiac effects on blood in the CFD models of part A1, it was desirable to reexamine the mixing of hepatic with IVC blood flow in the Fontan tunnel when respiration is taken into account in **part B2**. Furthermore, we will also reassess the HFD quantification and compare the HFD outcomes between the novel and conventional HFD quantification approaches when respiration is incorporated into the CFD models. We used real-time PC-MRI acquired flow data that contain information about the cardiac and respiratory effects on blood flow to reconstruct the boundary conditions in the CFD simulation. We *hypothesized* that incorporating the cardiac and respiratory effects at the boundary conditions have an impact on the mixing properties between hepatic and IVC blood flow within the Fontan tunnel and HFD outcomes.

Thesis outline

The master thesis itself is built up as follows; the current chapter, chapter 1: *General introduction* provides a general introduction about the Fontan procedure, the importance of a balanced HFD towards both lungs and the role of respiration on blood flow in a Fontan circulation. Furthermore, this chapter introduces the application of CFD to evaluate the Fontan performance and questions certain assumptions that have previously been taken in recent CFD studies in order to quantify HFD. Chapter 2: *Theoretical background*, gives a detailed insight into Fontan fluid dynamics, the clinical imaging technique of free-breathing ECG-gated 2D-3dir PC-MRI and real-time PC-MRI, the fundamentals of CFD and the differences between the Lagrangian particle tracking and the Eulerian confection diffusion modeling methods. Chapter 3 presents the *General methods.* This chapter provides a detailed overview of the technical steps that have been taken in this master thesis project. In *part A1* of this master thesis, we performed CFD simulations of 15 Fontan patients. The boundary conditions of the CFD models in part A1 only considered the cardiac effects on blood flow. In part A1, we tested the previously used assumption that hepatic blood flow is uniformly distributed in the Fontan tunnel by evaluating the degree of mixing between hepatic and IVC blood in the Fontan tunnel. Furthermore, we quantified HFD using particle tracing directly from the hepatic veins (novel approach) and compared results with the conventional approach, in which particles were uniformly seeded from cross-sections within the Fontan tunnel (conventional approach). In *part B2* of this master thesis, we carried out CFD simulations of three Fontan cases and used boundary conditions that incorporated both the cardiac and respiratory effects. In part B2, we re-examined the assessment of mixing of hepatic blood with IVC blood in the Fontan tunnel and the HFD outcomes while respiration was taken into account. In *part B1,* we performed an in-depth flow analysis using real-time PC-MRI without the use of CFD. The main goal was to investigate the role of respiration on blood flow in the IVC, SVC, Fontan tunnel and hepatic veins. All three parts (A1, B1 and B2) have their own introduction, methods, results, discussion, limitations and conclusion sections. The *General discussion* is presented in chapter

4. The recommendations for future research are given in chapter 5: *Future research and recommendations*. This master thesis finishes with chapter 6: *General conclusion* with regard to the overall obtained results.

2. Theoretical Background

2.1 Fontan fluid dynamics

A healthy cardiovascular system contains a pulmonary and systemic circulation connected in series and driven by two simultaneously pumping ventricles (i.e., biventricular circulation). A key characteristic of a Fontan circulation (i.e., single ventricle circulation) is the absence of a sub-pulmonary ventricle that steadily pumps the blood into the lungs (figures 6 and 7)[49]. Due to the Fontan circulation, the flow and pressure through circulation differ from a biventricular circulation.

The single ventricle has to provide the power source for the blood flow in both systemic and pulmonary circulations. Therefore, in comparison with a healthy cardiovascular system, the single ventricle has to pump against an enlarged afterload[50]. Afterload is the resistance that the ventricle of the heart has to overcome to eject the blood from the ventricle during contraction of the heart muscle (i.e., systole). Additionally, since the driving force for pulmonary flow is decreased, there is a reduction of ventricle preload compared to biventricular circulation[51]. Preload is the initial stretching of myocardial fibers before the heart contracts (i.e., filling pressure). Lastly, the right ventricle (for patients with hypoplastic left heart syndrome) may not be well appropriate for the elevated afterload, leading the ventricle function to fail over time[52].

As stated before, respiration is primarily responsible for the flow pulsatility in the Fontan tunnel and hepatic veins. The Fontan tunnel and the hepatic blood flow were significantly higher during inspiration than during expiration in Fontan patients[23–27,29–41]. Furthermore, the cardiac cycle barely affected the flow pulsatility in the Fontan tunnel and hepatic veins in Fontan patients[24,27,30,31,42]. Research revealed that this effect of respiration is less pronounced in the IVC in Fontan patients [24,34–36].

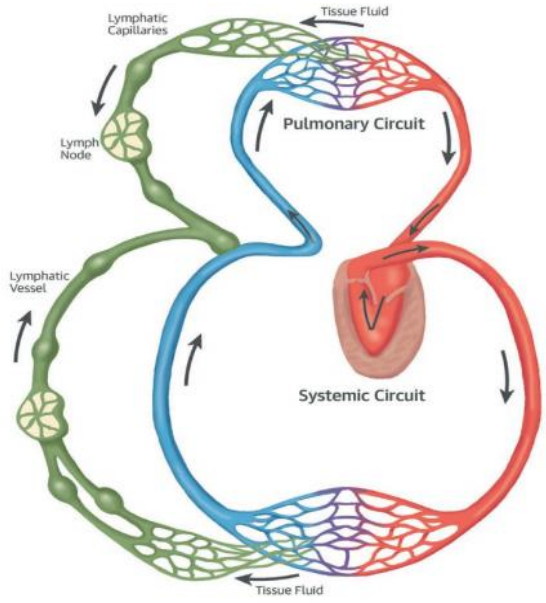

Figure 7: The Fontan circulation (i.e., single-ventricle circulation)
Available via: STS/EACTS Latin America Cardiovascular Surgery Conference

2.1.1 Flow patterns

Generally, it is assumed that blood flow behaves laminar in the human body. In the case of laminar flow, the fluid particles travel in layers, in contrast to turbulent flow, defined by highly disordered velocity fluctuations between the fluid particles (figure 8). To determine whether the fluid is going to be laminar or turbulent, we can use the parameter called Reynolds number (Re). The Reynolds number is a function of the density (ρ) and velocity (v) of the fluid, the diameter (D) of the blood vessel and the dynamic viscosity (μ). If Re is below roughly 2300, we usually say it is a laminar flow. If Re is between 2300 and 4000, the flow is in transition. If Re is greater than 4000, then it is a turbulent flow. The Re equation is the following[53]:

$$Re = \frac{\rho \cdot v \cdot D}{\mu} \tag{2.1}$$

Where:

$Re = Reynold's\ number$ [-]

$\rho = \ fluid\ density\ [kg\ m^{-3}]$

$v = fluid\ velocity\ [\frac{m}{s}]$

$D = diameter\ [m]$

$\mu = dynamic\ visocity\ [Pa \cdot s]$

Although blood flow is generally considered as laminar flow, blood flow is driven by a pulsatile pressure gradient and sometimes reaches high peak velocity magnitudes and flow rates. In this master thesis project, we evaluated the Reynolds numbers for one case using two types of flow acquisitions that either considered only the cardiac effects or both the cardiac and respiratory effects. The Reynolds numbers for this one case usually were between 400 and 600 (i.e., laminar flow) within the Fontan tunnel. Nevertheless, peak Reynolds number could reach values ranging from 1978 and 2748 depending on the considered type of flow since respiratory effects increase the blood velocity. The explanation for these high Reynolds numbers was a combination of a larger diameter, for instance, at the level of the pulmonary artery bifurcation, and higher short-term peak velocities. Since the peak Reynolds numbers were only slightly above the laminar and far below the turbulence threshold, the Fontan blood flow was in transition for a short time during the cardiac or the respiratory cycle.

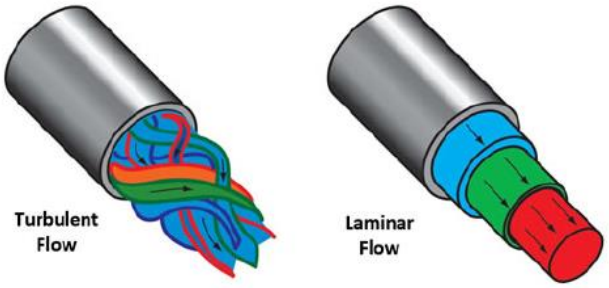

Figure 8: Visualization of turbulent and laminar flow in a pipe. *Available via: Turbulent Flow Rate Calculator. https://www.smartflow-usa.com/turbulent-flow-rate-calculator*

Another important non-dimensional parameter relevant to blood flow is the Womersley number. The Womersley number defines the ratio of the inertial forces and the viscous forces of the blood flow[53]:

$$\alpha = \frac{D}{2} \cdot \sqrt{\frac{(\omega \cdot \rho)}{\mu}} \tag{2.2}$$

Where:

$\alpha = Womersley\ number\ [-]$

$D = diamemeter\ [m]$

$\rho = \ fluid\ density\ [kg\ m^{-3}]$

$\mu = dynamic\ visocity\ [Pa \cdot s]$

$\omega = angular\ frequency = \frac{2*\pi}{T}\ [\frac{rad}{s}]$ with T the cardiac cycle or respiratory cycle time

$T = \ cardiac\ cycle\ or\ respiratory\ cycle\ time\ [s]$

For smaller Womersley numbers, the frequency is slow enough for the flow to develop a parabolic velocity profile in straight cylinder. For higher Womersley numbers, the velocity profiles show a more Womersley profile. Figure 9 demonstrates the velocity profile of flow-dependent on the Womersley number acquired from the N-S equation's solution in a straight cylinder. Of course, in a human body vessels are not perfectly straight cylinders. Besides, blood vessels are connected to other blood vessels by junctions, which cause local velocity profile changes. Therefore, real velocity profiles could differ from the expected velocity profile based on the calculated Womersley number. Nevertheless, it was wise to consider the Womersley numbers because it helped to understand the flow patterns within the Fontan circulation. In this project, the Womersley's numbers one patient varied depending on which cycle time (cardiac or respiratory) and so angular frequency was taken into account. For example, the Womersley number measured in the IVC for one case (D= 19.15e-3 m, μ= 0.0035 Pa·s, ρ = 1060 kg m^{-3}) when considering the cardiac cycle time (T= 0.939s) was 13.63. The Womersley number for that similar case when considering the respiratory cycle time (4.004s) was 6.60. These Womersley numbers increased if it was measured more upstream at pulmonary artery bifurcation since the diameter (D=24.4e-3 m) was larger at this location, respectively 17.40 and 8.41 depending on the chosen cycle time (respectively cardiac or respiratory). Although we have not evaluated the Womersley number for every patient, the outcomes of this single case showed the Womersley number could vary considerably depending on the measurement location, the cardiac or respiratory cycle time, and so the angular frequency.

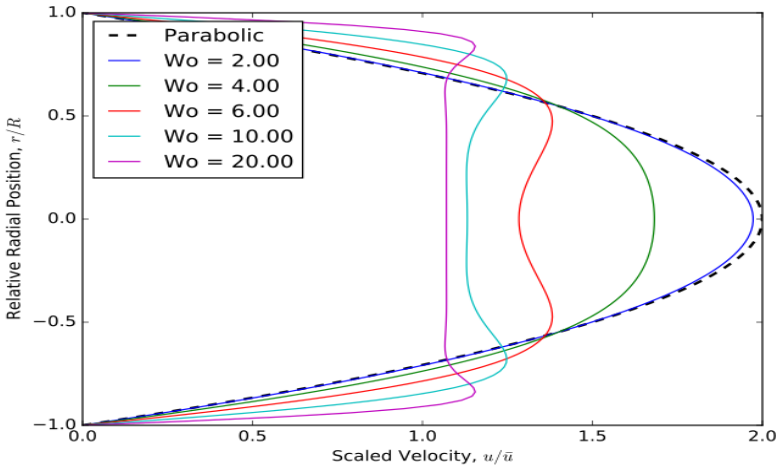

Figure 9: Type of velocity profile related to Womersley number acquired from the N-S equation's solution in a straight cylindric tube. *Available via: tps://commons.wikimedia.org/wiki/File:Comparison_of_velocity_profile_of_Womersley_flow.svg.*

2.1.2 Navier-Stokes equations

The physical characteristics of any fluid flow are determined by three fundamental equations: the continuity equation (the law of the conservation of mass), the momentum equation (which is Newton's second law of motion ($F = m * a$) applied to fluid) and the energy equation (the law of conservation of energy applied to fluid). These mathematical equations are in the most general form partial differential equations. The Navier-Stokes (N-S) equations combine all these three fundamental principles and describe how velocity, pressure, density and temperature of moving fluid are related[53]. In the CFD simulations, blood was considered as an incompressible fluid, whose density does not change with pressure changes (blood density is normally estimated at $\rho = 1060\ kg\ m^{-3}$)[54]. A Newtonian fluid is defined as fluid for which the viscous stress (τ) is linear related to the shear rate (or gradient of the velocity field ∇v) by the equation $\tau = \mu\ (\nabla v)$. Blood has non-Newtonian behavior and is usually defined in a Carreau fluid model, where the viscosity at high shear rate ($\dot{\Upsilon} = \nabla v$) matches the value for a Newtonian fluid[53,55]:

$$\eta_{eff}(\dot{\Upsilon}) = \eta_{\infty} + (\eta_0 - \eta_{\infty})\left(1 + \left(\lambda\dot{\Upsilon}\right)^2\right)^{\frac{n-1}{2}} \qquad (2.3)$$

Where:

$\eta_{eff} = fluid\ viscosity\ depending\ on\ the\ shear\ rate\ by\ Carreau's\ equation\ [Pa \cdot s]$

$\eta_0 = viscosity\ at\ zero\ shear\ rate\ \ [Pa \cdot s]$

$\eta_{\infty} = viscosity\ at\ high\ shear\ rate\ [Pa \cdot s]$

$\lambda = relaxation\ time\ [s]$

$n = \ power\ index$

$\dot{\Upsilon}\ (or\ \nabla v) = shear\ rate\ [s^{-1}]$

For blood of constant density ρ and variable viscosity η_{eff}, the N-S equations coupled with the continuity equation becomes[53,55]:

$$\rho\left[\frac{\partial u}{\partial t} + (u \cdot \nabla)u\right] = \nabla\left[-p\mathbf{I} + \eta_{eff}(\nabla u + (\nabla u)^T)\right] \quad (2.4)$$

$$\nabla \cdot u = 0 \quad (2.5)$$

Where:

$u = velocity\ \left[\frac{m}{s}\right]$

$\rho = fluid\ density\ [kg\,m^{-3}]$

$\eta_{eff} = fluid\ viscosity\ depending\ on\ the\ shear\ rate\ by\ Carreau's\ equation\ [Pa \cdot s]$

$p = fluid\ pressure\ [Pa]$

$t = time\ [s]$

In this master thesis, based on literature, the following values were chosen for the different parameters used in the CFD models: η_0=0.25 [Pa·s], η_∞= 0.0035 [Pa·s], λ=25 [s] and n = 0.25[54]. The blood was supposed to have a constant density ρ = 1060 [kg/m3].[54]

2.2 Computational fluid dynamics

Computational fluid dynamics (CFD) is the technology that applies computers to simulate fluid flow (i.e., fluid modeling) by solving the N-S equations (#2.4-2.5). Because the N-S equations are partial differential equations, nonlinear and highly coupled, solving the N-S equations analytically is extremely difficult and only possible for very simplified fluid cases. Unfortunately, the N-S equations of blood flow in a human body are too difficult to solve analytically. One solution to overcome this problem is using CFD to solve complicated fluid issues. With CFD, the geometry of interests (i.e., the computational fluid domain) is subdivided into a large number of control volumes or elements (or cells). All cells together are called the mesh. For each of these cells we can approximate the continuous N-S partial differential equations with discrete algebraic equations. This method of converting the continuous N-S equations into discrete algebraic equations which can be resolved for a given finite volume, is called the finite volume method. These discrete algebraic equations enable to calculate the pressure and velocity at the center (called a node) of each cell based on the velocity and pressure values of the surrounding nodes. The higher the order of these discreate algebraic approximations, the more neighboring nodes are used. As a consequence, each node of each cell will have a set of algebraic equations. Since the value of one node of each time step is depending on the values of the nearby nodes and vice versa, these discrete algebraic equations are connected. In order to solve these discrete algebraic equations for each cell, all discrete algebraic equations are assembled into one large matrix. Solving this immense matrix of discrete algebraic equations (which is a matrix inversion problem) requires a large number of iterative calculations per time step[53,56]. In this project, we used ANSYS Fluent (v17.1, ANSYS, Inc) as CFD solver.

2.2.1 CFD workflow

There are different software packages available for CFD modeling. All these software packages need a specific pipeline to create CFD models that incorporate patient-specific three-dimensional (3D) geometries and flow data as boundary conditions (figure 10). CFD uses the following workflow: Firstly, the geometry of the anatomy is extracted from static 2D MRI images by drawing contours of the vessel with segmentation tool software packages, which process is called segmentation. All these 2D vessel contours are combined to reconstruct a 3D geometrical model of the blood vessel. Because the 3D geometrical model is created from 2D blood vessel contours, this could cause irregular and rough surfaces and therefore, additional surface smoothing steps are needed to keep the model computationally stable. Secondly, centerlines of the vessel or geometry are applied for clipping and closing the in- and outlet surfaces perpendicular to the centerlines. Hereafter, cylindrical extensions (i.e., flow extensions) are added to each in- and outlet, ensuring that flow incoming and leaving the region of interest is fully developed. Hereafter, a mesh of the 3D geometrical model is created where the fluid domain is discretized into 3D-cells. Patient-specific CFD modeling needs information of patient-specific physiological data such as heart rate, time-varying volumetric flow rates, velocity fields of each vessel, or flow distributions between vessels to reconstruct boundary conditions. Boundary conditions are constraints set to the flow inlets, outlets and wall that need to be applied when solving the fluid problem. An example of a boundary condition is the prescription of time-varying volumetric flow rate waveform at the inlets based on the patient-specific PC-MRI data. Furthermore, material properties for the wall and blood should be determined. After completing the different pre-processing steps, the next step is processing, in which solver settings are defined and the CFD model is simulated. There are two simulation options; steady-state simulation in which the velocity at each location in space is constant with time and unsteady or transient simulation with a changing velocity/flow over time. After the simulation, the obtained results are processed and visualized to draw conclusions. This step is called post-processing. Finally, the CFD simulation outcomes should also be validated with patient-specific data to check if the outcomes agree with physical reality[53,57,58].

Pre-processing					**Processing**	**Post-processing**
Scanning	Segmentation	Smoothing & centerlines	Clipping & meshing	Reconstruction of boundary conditions	Simulation with CFD software	Analyzing results

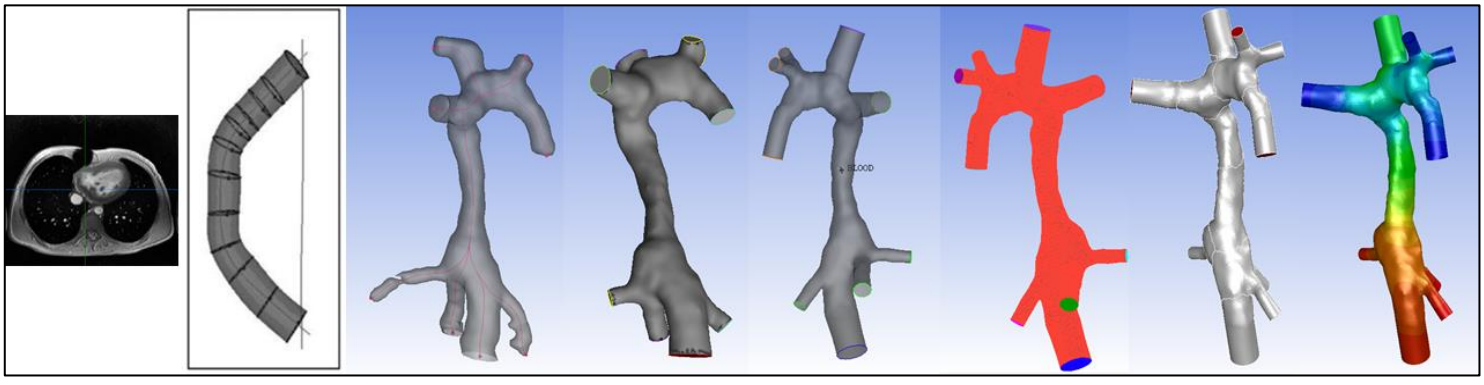

Figure 10: CFD pipeline

2.3 PC-MRI acquisitions

In this master thesis, the CFD models' boundary conditions were reconstructed from PC-MRI extracted flow data. We used two types of PC-MRI: 1. free-breathing ECG-gated PC-MRI with three directional velocity encoding (2D-3dir PC-MRI) and 2. free-breathing non-ECG gated 2D PC-MRI (i.e., real-time PC-MRI) in which velocity is determined in only one direction in the through-plane direction. In part A1, we used the first type of PC-MRI in the CFD models that only considered cardiac effects on blood flow, whereas the second type of PC-MRI was used in parts B1 and B2, which flow analyses and CFD models included both the cardiac and respiratory effects on blood flow. This paragraph provides information about PC-MRI in general and the difference between free-breathing ECG-gated 2D-3dir PC-MRI and real-time PC-MRI. PC-MRI acquisitions details used in this project are given in table 1.

2.3.1 PC-MRI in general

Magnetic resonance imaging (MRI) utilizes a strong magnetic field and radiofrequency energy (i.e., radio waves) to provide detailed images of organs. The principles of MRI are based on the fact that protons within a nucleus of an atom have a magnetic moment (figure 11A). If the atom with protons is placed in a magnetic field, they are forced to align with the magnetic field (Figure 11B). Radio waves are then pulsed through certain areas of the body, thereby forcing the atomic nuclei out of alignment with the magnetic field and inducing a spin of the atoms (figure 11C). Once the applied radio waves are turned off, the atomic nuclei realign (figure 11D). This causes the atomic nuclei to release energy and send radio waves, which are captured by receivers. MRI takes advantage of the nucleus of a hydrogen atom since its abundance in the body. The nucleus of a hydrogen atom has one single proton[59].

The MRI signal is extracted from voxels using a Fourier transform and through an advanced method that measures the true signal (i.e., representing the real anatomy) to noise (signal-to-noise ratio, i.e., SNR). Voxels are volume elements containing millions of protons that create together the MRI signal. Once the MR signal is extracted and converted, it is a vector quantity obtaining a magnitude and a direction (i.e., phase). Normal static MRI reconstruction only uses the magnitude of the MR-signal. However, a special type of MRI is phase-contrast MR imaging (i.e., PC-MRI), using both the magnitude and phase of the MR signal of a voxel. PC-MRI can be used to visualize and quantify moving blood flow. PC-MR imaging takes advantage of the phase to quantify the velocity of the blood within a voxel. Protons of moving blood contain a phase-shift proportional to their velocity when they are placed in a strong magnetic field. These phase shifts proportional to the velocity are extracted from the voxel and transformed into a greyscale image. Because phase-shifts are used to register velocities, it is limited by the periodicity of the sine function. With PC-MRI, we considering both the positive and negative velocities (i.e., the velocities that are going upwards and downwards through the plane). Therefore, we divide the 360 degrees into two 180-degree parts. The peak velocity that matches to 180 degree phase shift is called the velocity encoding (VENC) value and is defined by the examiner. Beyond that value, if phase shifts are larger than 180 degrees, the MRI device cannot distinguish if the blood velocity is positive or negative, which phenomenon is called aliasing. The VENC value needs to be set higher than the blood vessel's maximum velocity to avoid aliasing. However, on the other hand, if the VENC is

determined too high, there is a higher risk of measurement errors. With these PC- velocity images, blood flow rates can be quantified[59].

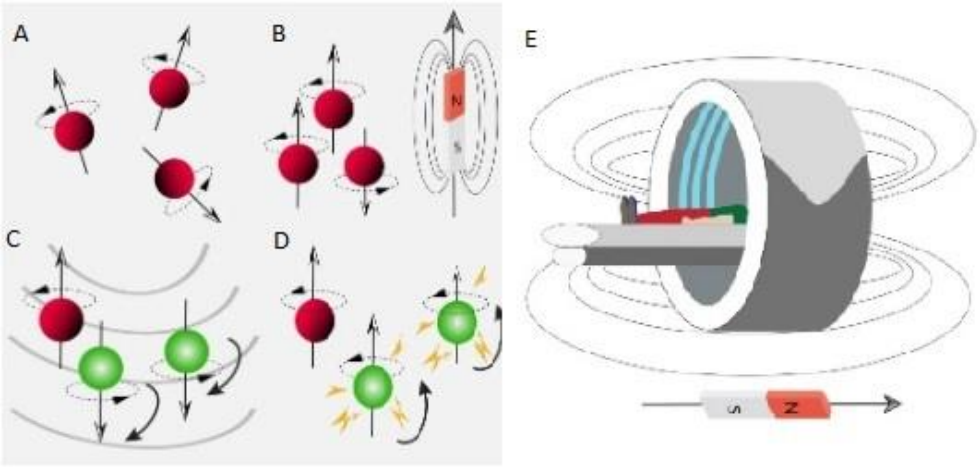

Figure 11: 11A: Protons spin in a random direction, 11B: Protons spin in the direction aligned with an applied magnetic field, 11C: Protons change their spinning direction when the radio frequency pulse is applied, 11D: protons return to their previous directions and release energy once the radio frequency pulse is turned off, 11E: MRI scanner with a strong magnetic field. *Available via: https://knowingneurons.com/2017/09/27/mri-voxels/*

2.3.2 Free-breathing ECG-gated (non-navigator) 2D-3dir PC-MRI

In part A1, we used free-breathing ECG-gated 2D-3dir PC-MRI extracted flow data to create the boundary conditions in the CFD models that ignore respiration. 2D-3dir PC-MRI uses thin slices (1-2 mm thick) containing voxels, in which the velocity is encoded in three principal directions (figure 12A and 12B). The slices are collected consecutively over the domain of the various blood vessels[63]. Therefore, this approach is often called the single-slice three directional acquisition. The plane of the slices is placed perpendicular to the imaged blood vessels. The through-plane velocity-encoding direction is the direction perpendicular to the plane and in the blood flow direction. The in-plane (or in-slice) velocity encoding directions are the directions along the plane. Initially, the hospital's idea was to use the three-directional (3dir) velocity vectors in the CFD models. However, in this master thesis project, we used the volumetric flow rates extracted from one velocity encoding direction, namely the through-plane direction, to reconstruct the CFD models' boundary conditions instead of using all three-directional velocity vectors. Because the through-plane direction is in the blood flow direction, this direction is more relevant than the in-plane direction for flow rate quantification. Velocity encoding in the three principal directions increases the scan time and so it is impossible to acquire the data under breath-holding conditions[62]. Nevertheless, respiration and cardiac contraction can lead to motion artifacts in the PC-MR images of the Fontan circulation. Cardiac contraction can lead to motion artifacts in the PC-MR images of the Fontan circulation. Electrocardiogram (ECG) gating (or synchronization) during PC-MR imaging can be used to avoid cardiac motion artifact. During ECG gating data is acquired continuously over the entire cardiac cycle for several heartbeats. Retrospectively, data of several heartbeats are synchronized and averaged to a velocity data set of one cardiac cycle, providing a higher image quality with fewer artifacts[63]. The drawback of using ECG gating is that any respiratory effect

on blood flow will be averaged too[64]. In other words, ECG-gated acquired flow data only considers the cardiac effects on blood flow, as used in part A1. We did not use respiratory compensation techniques (i.e. navigator-gating, see below) that account for the potential respiratory motion artifacts. However, since an average velocity data set of one cardiac cycle was reconstructed due to the ECG-gating – motion artifacts were averaged out too, and therefore the MR image quality was still high enough.

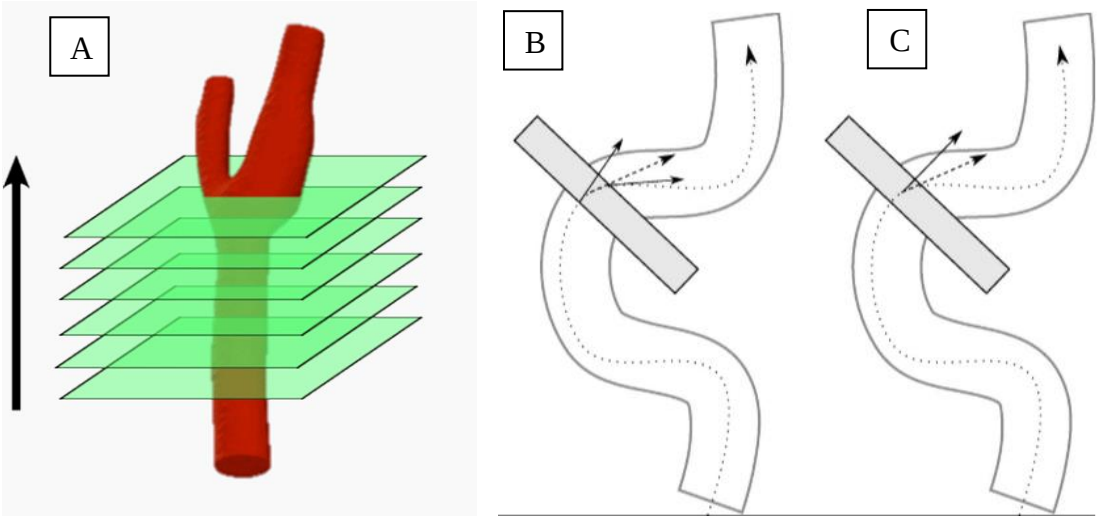

Figure 12: 12a: workflow of 2D PC-MRI by acquiring time-resolved velocity data of sequential slices, 12b: 2D-3dir PC-MRI, 12c: 2D-1dir PC-MRI. *Available via: Schubert et al. Peak velocity measurements in tortuous arteries with phase contrast magnetic resonance imaging: The effect of multidirectional velocity encoding. Invest Radiol. 2014;*

2.3.3 Respiratory compensation techniques during PC-MRI acquisitions (i.e., navigator)

Regarding the respiratory-related motion artifacts, navigator-gating can be used as a compensation technique to improve PC-MRI quality. During navigator gating, a belt is placed around the patient at the diaphragm level and measures the abdomen expansion during free-breathing. This periodic expansion creates a respiratory waveform on which an MRI acquisition window is determined. The pre-determined acquisition window is usually chosen during the end-expiration phase of the respiratory cycle because the diaphragm movement is negligible at that time frame, leading to fewer respiratory motion artifacts. All other data outside the pre-determined acquisition window is rejected[65–67]. The navigator gated MRI acquisition duration depends on the navigator's efficiency and how regularly the patient breathes. The drawback of using navigator-gating is that it does not allow to measure the respiratory effects on the blood flow waveforms. Another disadvantage of navigator gating is that data acquisition occurs during only a small part of the respiratory cycle, namely the end-expiratory phase, which leads to 30-60 % data acquisition efficiency[68].

2.3.4 Free-breathing non-ECG gated non-navigator gated 2D PC-MRI (i.e., real-time PC-MRI)

2D PC-MRI uses thin slices (1-2 mm thick) containing voxels, in which velocity is determined in only one direction through a 2D plane (unidirectional) (figure 12A and 12C). Therefore, this approach is often called the through-plane 2D PC-MRI (2D-1dir) method. If the 2D PC-MRI

acquisitions are acquired under free-breathing conditions without ECG- or navigator gating, it is called real-time PC-MRI. Since there is no ECG-gating nor navigator gating, thereby both the cardiac and respiratory effects on blood flow are present simultaneously, at the expense of a potentially higher risk of motion artifacts. Nevertheless, in this project, acceleration techniques during real-time PC-MRI were applied, which allowed the acquisition of 15 PC-MR images per second and reduced the impact of the respiratory motion (Table 1). Furthermore, we had to set the VENC value of the Fontan tunnel during the real-time acquisitions higher than during 2D-3dir PC-MRI acquisitions since the present respiratory effects increased the Fontan tunnel's velocity. Real-time PC-MRI obtained flow data was used in part B1 and part B2 since we were interested in the respiratory effects on blood flow in these chapters.

Table 1: PC-MRI acquisitions details

MRI details	**2D-3dir PC-MRI**	**Real-time PC-MRI**
Slice thickness (mm)	5	5
Acquired in-plane spatial resolution (mm)	1.5 x 1.5	2.5x2.5
Acquired temporal resolution (ms)	41.0	67.0
Nr of phases per cardiac cycle	25-30	n/a
Nr of phases	n/a	250
ECG-gating	retrospective	-
Respiratory compensation (navigator)	-	-
VENC of IVC (cm/s)	60	100
VENC of Fontan tunnel (cm/s)	50	50
VENC of SVC (cm/s)	40	40
ms; milliseconds, mm; millimeter, VENC; velocity encoding, SENSE; sensitivity encoding		

2.4 Lagrangian and Eulerian method for HFD quantification

After the CFD simulation, we used the simulation results to calculate and visualize the HFD to both lungs as a post-processing step. Two methods could be used for HFD quantification: the Lagrangian and Eulerian methods.

2.4.1 The Lagrangian method for HFD quantification

The Lagrangian method uses separate particles and evaluates the trajectory of every particle individually. We assumed massless particles according to literature[20,60,69–72]. Since the particles do not have mass the local particle velocity U_p is equal to the local fluid velocity magnitude U in the cell of the CFD mesh. So in other words, massless particles follow the streamlines of the blood flow. So if a particle moves from one location in the CFD mesh to another location, the following equation is being solved[53,73,74]:

$$\frac{dx_p}{dt} = U_p = U \tag{2.6}$$

Where:

$\frac{dx_p}{dt} = rate\ of\ change\ of\ particle\ position\ [\frac{m}{s}]$

$U_p = particle\ velocity\ [\frac{m}{s}]$

$U = \ local\ field\ velocity\ \left[\frac{m}{s}\right]$

$$\frac{x_p^{i+1} - x_p^i}{\Delta t} = U_p^i \tag{2.7}$$

$$x_p^{i+1} = x_p^i + U_p^i * \Delta t \tag{2.8}$$

Where:

$x_p^{i+1} = next\ particle\ position\ [m]$

$x_p^i = current\ particle\ position\ [m]$

$U_p^i = current\ particle\ velocity\ [\frac{m}{s}]$

$\Delta t = time\ step\ [s]$

Equation 3.8 means the next particle position is equal to the current particle position plus the current particle velocity times the time step. We know that the current particle velocity is equal to the local fluid velocity since we have massless particles. Therefore equation 2.8 becomes:

$$x_p^{i+1} = x_p^i + U^i * \Delta t \tag{2.9}$$

Therefore, we use the local fluid velocity magnitude of every cell and time step of our CFD solution. The post-processing software ParaView applies equation 2.9 repeatedly and continuously updates the particle position until a complete particle trajectory over the entire fluid domain is provided. Paraview uses the time step size between the different velocity files written by ANSYS Fluent as Δt. In the CFD models of part A1, the time step size used in the simulation was the cardiac cycle time divided by 1000. However, the velocity files were not written for every time step, but for every ten time steps, resulting in a Δt = cardiac cycle time/100 in ParaView. We chose not to write velocity files for every time step since the post-processing would take too long. The same goes for the CFD simulations in part B2, in which the following time step size was used: respiratory cycle time divided by 5000. However, the time step size Δt in ParaView was a factor 10 smaller: respiratory cycle time/500.
In the Lagrangian approach, we seed the particles that represent the hepatic blood flow and evaluate the number of particles leaving through the left and right lung, which represent the HFD to both lungs. Since the Lagrangian method is the most renowned and commonly used method for HFD quantification in Fontan patients[20,60,69–72], we primarily applied the Lagrangian approach for HFD quantifications in this master thesis project.

2.4.2 The Eulerian method (i.e., Convection-Diffusion Model)

For one sub-analysis of one case in part B2, we used the Eulerian method for HFD quantification as well. We were interested in this approach since a pilot study by Prof. dr. S. Kenjereš and Duco Gaillard demonstrated that the Eulerian method might be a more convenient alternative for the Lagrangian method. The Eulerian method uses the concentration of particles and computes the overall confection and diffusion of a number of particles. The convection-diffusion equation for an incompressible fluid, constant diffusion coefficient, and in a situation where there are no sources or sinks, is the following[75]:

$$\frac{\delta}{\delta t}(C) + \nabla * (\vec{v}C) = D_b \nabla^2 * C \qquad (2.10)$$

$$Accumulation + Convection = Diffusion$$

Where:

$C = species\ concentration\ \left[\frac{kg}{m^3}\right]$

$D_b = blood\ diffusion\ coefficient\ \left[\frac{m^2}{s}\right] = 1.54e^{-9}\ \frac{m^2}{s}$ [76]

$\nabla = \left[\frac{\delta x}{\delta t} + \frac{\delta y}{\delta t} + \frac{\delta z}{\delta t}\right]$

In the CFD software package ANSYS Fluent (v17.1, ANSYS, Inc), we used the mass fraction (MF) instead of the concentration. The mass fraction was written to a file for every time step. Equation 3.10 therefore becomes:

$$\frac{\delta}{\delta t}(MF) + \nabla * (\vec{v}MF) = D_b \nabla^2 * MF \qquad (2.11)$$

Where:

$$MF = mass\ fraction = \frac{C}{\rho}$$

$$\rho = blood\ density = 1060\ [\frac{kg}{m^3}]\ ^{54}$$

For HFD quantification, it was necessary to use TECPLOT instead of ParaView. TECPLOT calculated the time-varying hepatic (flow) mass leaving through the left and right pulmonary artery by integrating the mass-weighted flow rate over the time of one respiratory cycle. TECPLOT made use of the same time step size as used in the CFD simulation. By calculating the average of the time-varying hepatic (flow) mass over the respiratory cycle's time steps, the HFD towards the left and right pulmonary artery was quantified.

3. General Methods

This chapter provides an overview (figure 13) of the technical steps that have been taken in this master thesis project. This chapter has the following sections:

1. Patient population
2. Anatomic static MRI acquisition and image processing for the 3D reconstruction of the patient anatomy
3. Clipping and adding flow extensions
4. Mesh generation and mesh-independency study
5. Reconstruction of inlet and outlet boundary conditions using:
    a. Patient-specific free-breathing (non-navigator gated) ECG-gated 2D-3dir PC-MRI measurements
    b. Patient-specific free-breathing (non-navigator gated) non-ECG gated 2D PC-MRI measurements (i.e., real-time PC-MRI)
6. Treatment of vessel wall
7. Material properties
8. Solver settings and discretization schemes
9. Simulation details
10. Post-processing steps
    a. Quantification of mixing between hepatic and IVC flow
    b. HFD quantification
11. Validation of CFD models

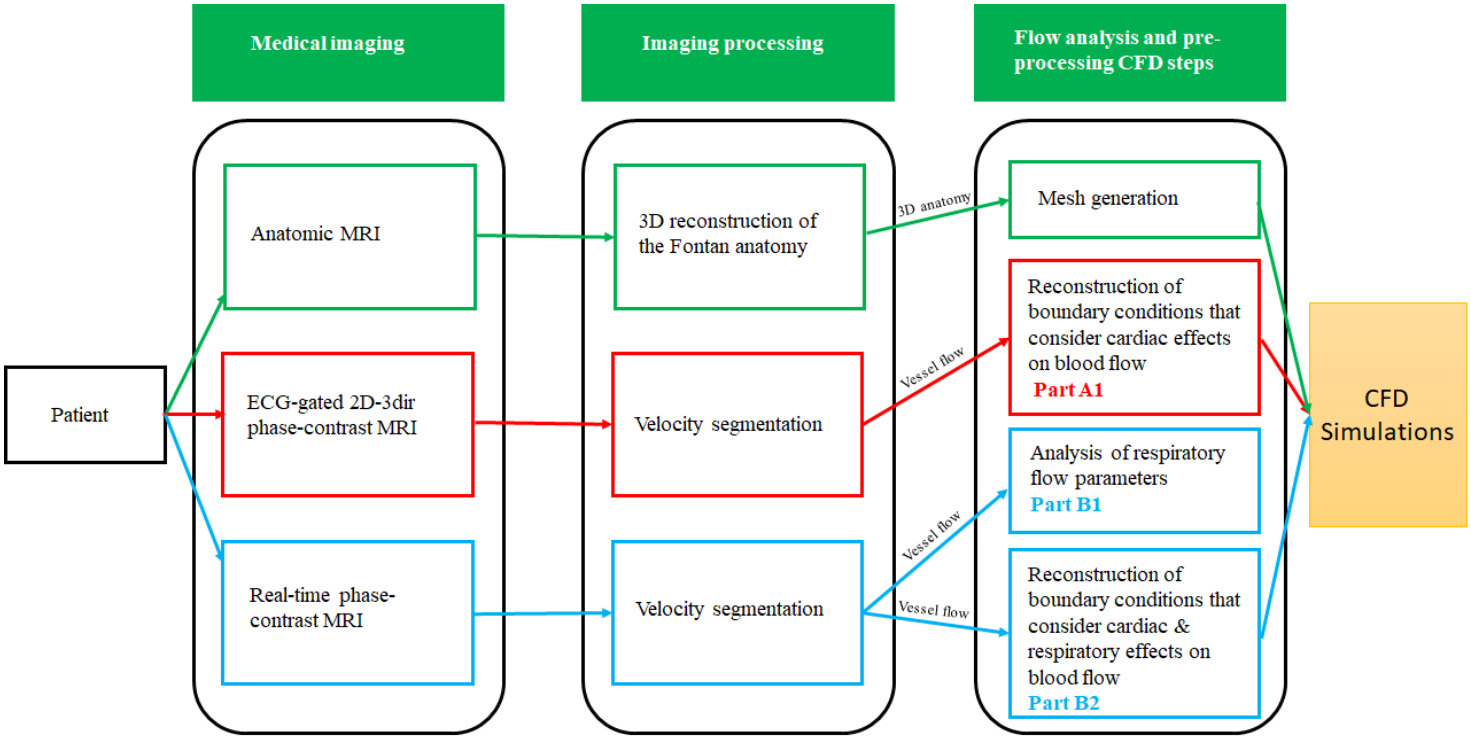

Figure 13: Schematic overview of how patient-specific data is used and analyzed in this master thesis project

The difference between the CFD simulations of part A1 and B2 is the type of PC-MRI acquisitions used to reconstruct the CFD models' boundary conditions. . As stated before in chapters 1 and 3, in part A1 we used boundary conditions that only took the cardiac effects on blood flow into account, whereas in part B2, we used boundary conditions that considered both the cardiac and respiratory effects on blood flow. Therefore, in part A1 we have simulated the blood flow for several cardiac cycles, whereas in part B2 we have modeled the blood flow for a couple of respiratory cycles, as will be discussed later in this chapter. Since all other steps were broadly similar between parts A1 and B2, except for the inlet boundary conditions reconstruction and some simulation details, we created this general method chapter.

3.1 Patient population

This master thesis project used patient data acquired from the Leiden University Medical Center database. All Fontan patients had a TCPC-type Fontan tunnel (ECC or ILT, see chapter A1), were above the age of 8 and participated in an ongoing cross-sectional research project (TOP-FLOW project) between Leiden University Medical Centre, Erasmus Medical Center Rotterdam and the Delft University of Technology. In part A1, we have simulated 15 Fontan patient cases, whereas, in part B2, we modeled three cases. These three cases of part B2 were the first cases that have been modeled when respiration was taken into account. Although more cases will eventually be modeled, only outcomes of these first three CFD cases are included in this master thesis report. The specific patient characteristics of each part of this master thesis project (part A1, B1 and B2) are being described in each individual part.

3.2 Anatomic MR imaging and 3D reconstruction of the Fontan anatomy

To obtain the Fontan anatomy, transversal and sagittal stacks of static (i.e., no phase-contrast) navigator-gated 2D cardiac MR images were used for segmentation. These static MR images only capture the blood vessel anatomy (i.e., anatomic MRI) and do not evaluate the blood velocity encoding as measured during PC-MRI. The MRI scanner was an Ingenia 3.0 Tesla MR system of Philips. These 2D images have an in-plane resolution of 0.9*0.9 mm and a slice thickness of 5 mm with 2.5 mm overlap between slices. The Fontan anatomy is complicated and in particular patient-specific. Therefore, these in vivo Fontan anatomies should be obtained precisely. The reconstruction of a 3D geometrical model of the Fontan anatomy using transverse and sagittal stacks of 2D cardiac MR images involves four crucial steps:

i. *Rigid registration*: since there could be a spatial misalignment between the transverse and sagittal stacks, rigid registration is needed to correct this potential misalignment.
ii. *Interpolation*: the in-plane and out-of-plane resolution of the 2D Cardiac MR images is different. Linear interpolation is needed to obtain isotropic voxels
iii. *Segmentation*: The interpolated images were subsequently segmented on the transversal and sagittal view using the semi-automatic, active contour with manual adjustment tool of open-source software ITK-SNAP[77]. Since we wanted to include the hepatic veins into the geometrical model (and so in the computational fluid domain), the final segmentation included the IVC below the hepatic veins, the hepatic veins, the Fontan tunnel, SVC and the left pulmonary artery, right

pulmonary artery and the upper lobe side-branches of the right pulmonary artery. A general example of the segmentation process is shown in figure 14.

iv. *3D reconstruction of Fontan model*: after segmentation, a 3D geometrical model of the Fontan anatomy was reconstructed. The 3D Fontan model was smoothed using the non-shrinking Taubin filter (500 iterations, Passband 0.05) option of the Vascular Modeling Toolkit (VMTK) open-source software. Centerlines were obtained for every vessel using VMTK[78]. Figure 14 demonstrates a general example of the 3D reconstruction and smoothing steps.

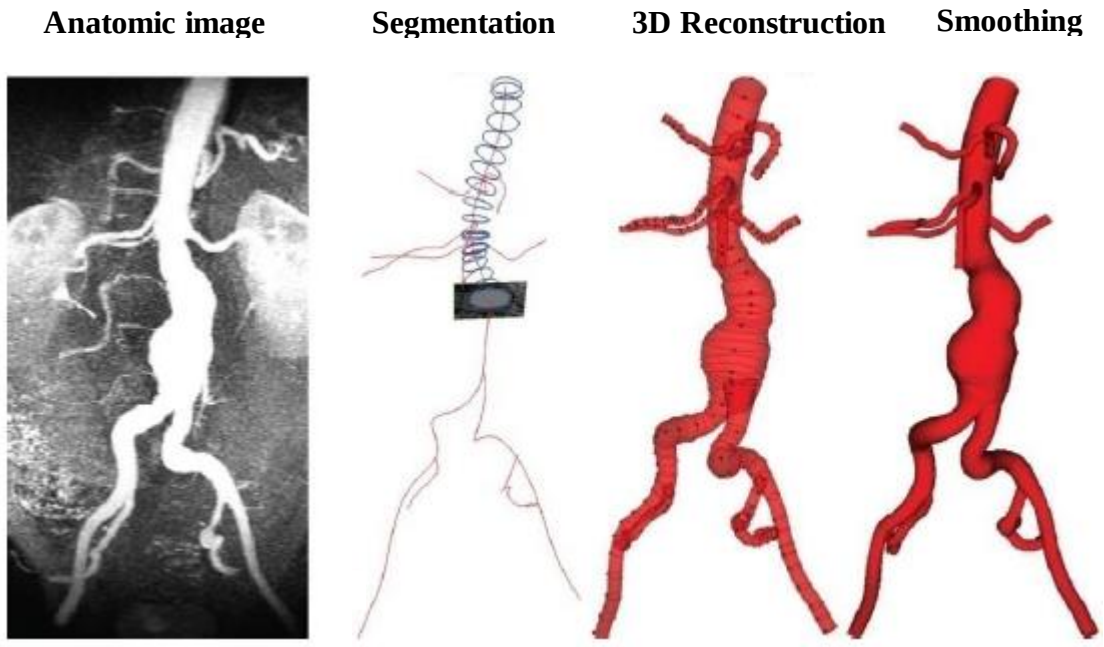

Figure 14: Anatomic imaging, segmentation, 3D reconstruction and smoothing steps of the Aortic blood vessel (this is not a Fontan anatomy). *Available via: http://www.crimson.software/documentation.html*

3.3 Clipping and adding flow extensions to the 3D geometrical model

The 3D geometrical Fontan models needed to be prepared for CFD simulation (figure 15). For CFD simulations, flat inlet and outlet cross-section areas perpendicular to the centerline are required. Therefore, the ANSYS-ICEM software (v 17.1, ANSYS, Inc.) was used to clip the inlet and outlet vessels perpendicular to the centerlines (figure 16). Regarding the hepatic veins, the left-, right- and middle- hepatic veins were clipped near to the IVC. If one of these hepatic veins had sub-branches close to the IVC, these sub-branches were clipped too. Hereafter, we added cylindric flow extensions to each vessel in- and outlet proportional to every vessel's diameter. Adding flow extensions is an important part of CFD modeling because flow extensions guarantee a complete development of the inflow velocities before the flow enters the region of interest. Lastly, we closed the flow extensions of all inlets and outlets, thereby making it possible to prescribe inflow and outflow boundary conditions (figure 17).

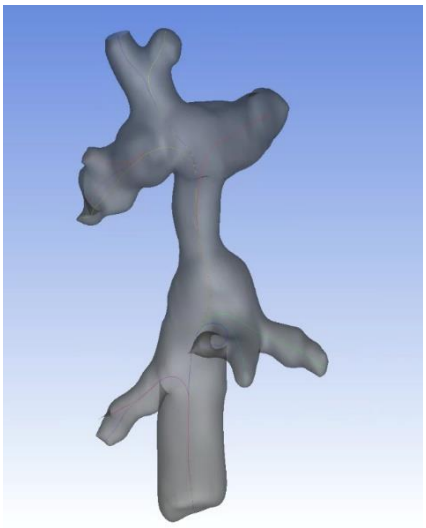

Figure 15: geometrical TCPC model without clipped inlets and outlets and flow extensions (directly after segmentation)

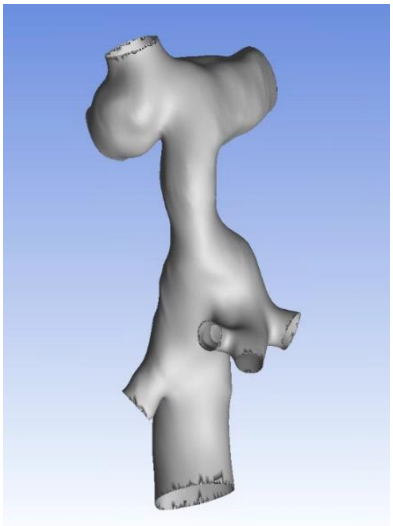

Figure 16: geometrical TCPC model with clipped open inlets and outlets

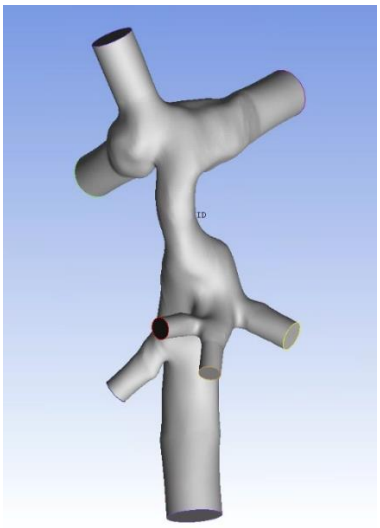

Figure 17: geometrical TCPC model with closed flow extensions at every inlet and outlet

3.4 Mesh generation and mesh independency study

We used an unstructured polyhedral mesh that was built using the meshing tools of ANSYS-ICEM & ANSYS-Fluent (v17.1, ANSYS, Inc). The definition of structured mesh is regular connectivity that provides fast and reliable results. The main drawback of a structured mesh is its severe limitation in the geometric complexity that can be meshed. In complicated geometries like blood vessels, it is challenging to generate a mesh that only consists of structured grids since structures meshes lack the flexibility to appropriately fill up a complicated geometry. An unstructured mesh does not follow a uniform pattern and is therefore often used in complex cardiovascular models. Recent CFD Fontan studies often applied an unstructured polyhedral mesh[72,79,80]. Although the reason of this polyhedral mesh choice is not clarified in the individual papers, polyhedral meshes are probably used because they provide the same level of accuracy but with lower amounts of cells compared to tetrahedral meshes, which speeds up the computation time[81,82]. The great advantage of a polyhedral element is it has more neighbor elements than, for instance, a tetrahedral element. Therefore, a polyhedral element can use more information from its neighbor cells into its calculations, resulting in a better approximation of the velocity and pressure gradients. Peric et al. (2004) showed that using 65513 polyhedral cells gave similar accurate results compared to the outcomes of a tetrahedral mesh with 393273 cells. Interestingly, the computation time for the polyhedral mesh was less than one tenth of the simulation time of the tetrahedral mesh[81].

We chose for an unstructured polyhedral mesh with four layers of boundary mesh (prism layers)[72]. The element (i.e., cell) size of the mesh was based on the average diameter of each geometrical model's inlet, and outlet vessels diameter divided by 30 and ranged between 0.4 and 0.5 mm between cases[72]. Applying a boundary mesh of prism layers is very common in CFD modeling because normal cells (tetrahedral, polyhedral, etc.) can elongate along the geometrical model wall, which could provoke inaccurate results[79,83]. Because prism-layers are less sensitive to elongation and better capture substantial velocity gradients along the wall[84], we added these to the geometrical model. Figure 18 demonstrates the polyhedral mesh with

four prism layers, and figure 19 shows an overview of the mesh used in one of the CFD models in this project.

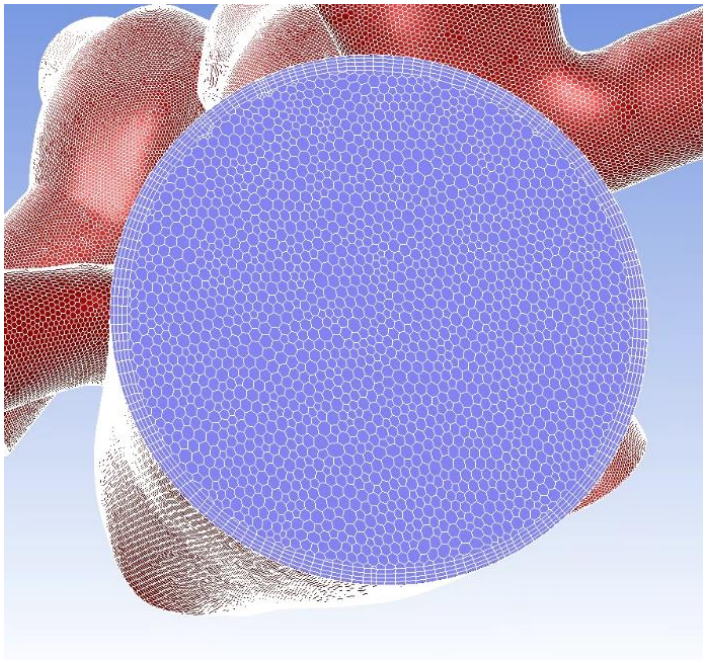

Figure 18: Polyhedral mesh with four prism layers

Figure 19: overview of the mesh used in one of the CFD models in this project

A mesh- and temporal refinement (independence) study evaluates how small the elements and time step size need to be to ensure that the outcomes of the CFD simulations are not affected by the size of the mesh or the time step size. The drawback of having a finer mesh or time step size is an increase in the number of equations that need to be solved and thus the computation time. Furthermore, we also investigated how many cardiac or respiratory cycles we had to simulate to eliminate the CFD simulation's startup effects.

The mesh independence study was performed on one of the Fontan CFD cases with maximum element sizes varying between average diameter vessel divided by 15 (=0.8 mm, mesh type 1), 20 (=0.6 mm, mesh type 2), and 30 (=0.4 mm, mesh type 3). The finest mesh with a maximum element size of 0.4 mm was the smallest mesh that could be created with the computer's computational power. Although the results between the different mesh sizes were almost identical, we noticed very little differences in the cross-sectional velocity profiles between the different mesh sizes for a short time during either the cardiac, especially when the flow reaches its peak velocity (figure 20). Therefore, the choice was made to simulate with the finest mesh type for every planned simulation to guarantee the most accurate solutions.

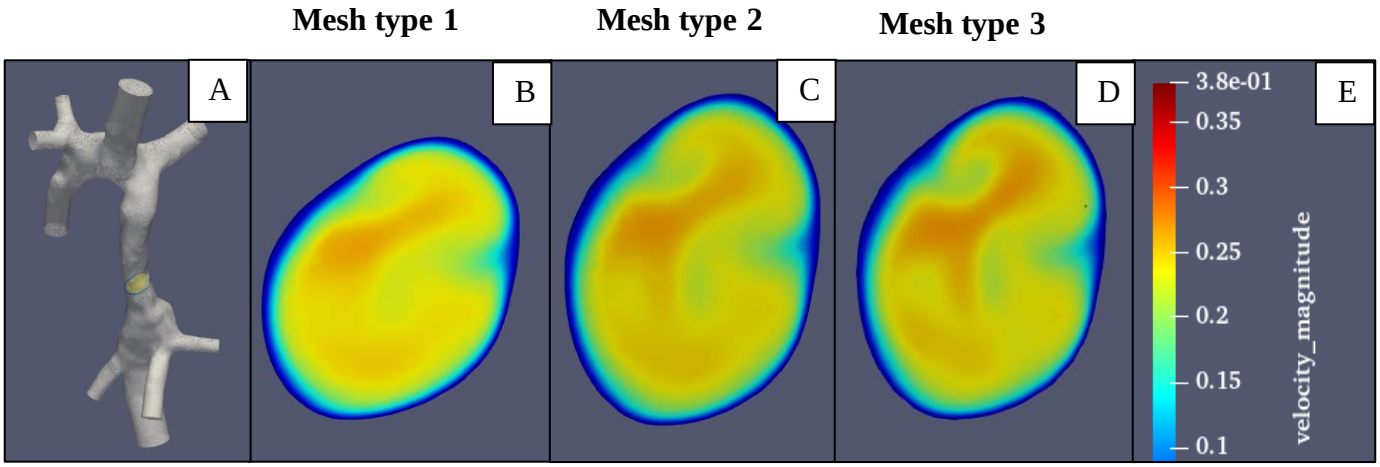

Figure 20: Figure 20 A: overview, cross-sections of velocity profile; 20B: mesh type 1, 20C: mesh type 2, 20D: mesh type 3, 20E: velocity magnitude scale [m/s]

The time step size was based on the Courant–Friedrichs–Lewy (CFL) condition commonly used in CFD simulation[85]. The CFL condition provides a general directive for choosing a correct time step size given the mesh size. The formula of the CFL condition is the following:

$$CLF = \frac{v * \Delta t}{\Delta x} \leq 1 \qquad (3.1)$$

Where:

$v = velocity\ magnitude\ [\frac{m}{s}]$

$\Delta t = time\ step\ size\ [s]$

$\Delta x = element\ size\ [m]$

The velocity magnitude of flow depends on the type of PC-MRI data. Real-time PC-MRI obtained data take respiration into account and usually showed larger velocity values, especially during the inspiratory phase, than ECG-gated 2D-3dir PC-MRI acquired data. In part A1, in which ECG-gated 2D-3dir PC-MRI data was used, the CFL condition was fulfilled when using a time step of $\Delta t = cardiac\ cycle/1000$. In part B2, in which real-time PC-MRI data was used, the CFL condition was satisfied when using a time step of $\Delta t = respiratory\ cycle/5000$. The reason we chose the cardiac cycle and the respiratory cycle as reference period in respectively part A1 and part B2 will be explained in paragraph 3.5.

Additionally, we investigated how many cardiac cycles (part A1) and how many respiratory cycles (part B2) we had to simulate to eliminate startup effects for one CFD case of part A1 and part B2. After several cardiac or respiratory simulation cycles, a stable solution (i.e., periodic behavior) for every time step, which no longer changes when successive simulation cycles are added, is expected. We analyzed the periodic behavior of a few points in the Fontan geometrical model of one case. The velocity magnitudes of these points were written to a file during the consecutive cardiac cycles or respiratory cycles. The next step was to analyze the velocity differences for each time step between the consecutive cardiac and respiratory cycles. An important finding was that at some points in the geometry during some phases of the cardiac or respiratory cycle, no periodic behavior was achieved in both types of CFD models. In the CFD model that only incorporated the cardiac effects on blood flow (part

A1), this non-periodic behavior was only found upstream within the left and right pulmonary arteries' bifurcation. At this locations, as mentioned previously in chapter 2, we have investigated the Reynolds number that could reach: $Re = \frac{\rho \cdot v \cdot D}{\mu} = \frac{1060 * 0.27 * 24.2e-3}{0.0035} = 1978$ during peak velocities. Regarding the CFD model that considered both the cardiac and respiratory effects on blood flow (part B2), this non-periodic behavior was also already found more downstream within the Fontan tunnel: $Re = \frac{\rho \cdot v \cdot D}{\mu} = \frac{1060 * 0.48 * 18.9e-3}{0.0035} = 2748$. These Reynolds numbers showed the blood flow was sometimes in transition for a short time during both the cardiac and respiratory cycle. Fluid flow can demonstrate flow instabilities when it is in transition. Nevertheless, most of the time, periodic behavior was achieved after three cardiac cycles in the CFD models that only consider cardiac effects on blood flow (part A1) and after two respiratory cycles in CFD simulations that consider both the cardiac and respiratory effects on blood flow (part B2). Figure 21 shows the difference of velocity values between consecutive respiratory cycles (RC) of a point in the Fontan tunnel, in which periodic behavior was fully not achieved. As you can see, most of the time-periodic behavior was achieved since the velocity difference between consecutive respiratory cycles was almost always around zero.

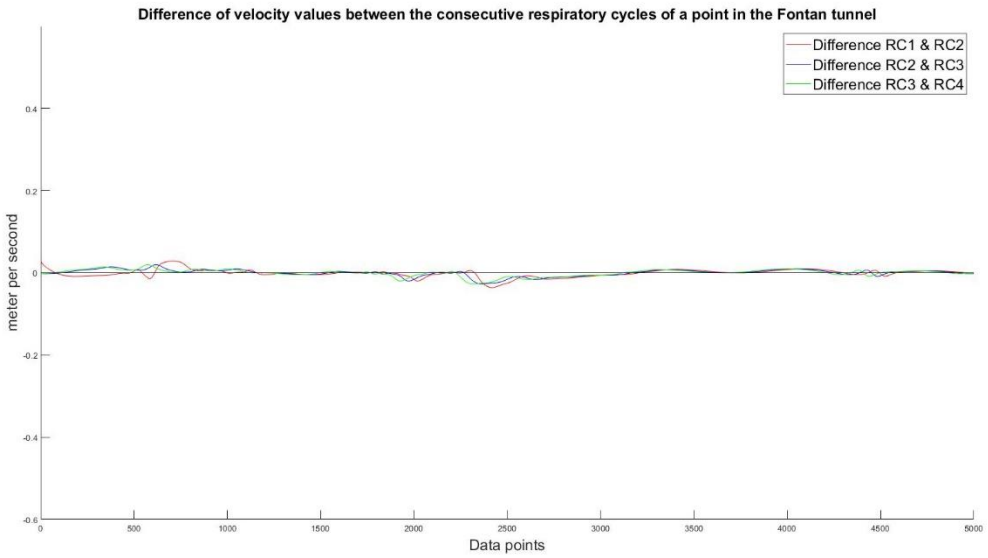

Figure 21: Difference of velocity values between the consecutive respiratory cycles of a point in the Fontan tunnel. RC = respiratory cycle.

3.5 Reconstruction of inlet and outlet boundary conditions

PC-MRI data was used to acquire velocity profiles at the slices perpendicular to IVC, Fontan tunnel, SVC, left pulmonary artery and right pulmonary artery (figure 22). In part A1 we used ECG-gated 2D-3dir PC-MRI data. Real-time PC-MRI data was used in part B2. Hereafter, we used velocity segmentation to convert the PC-MR images with velocity encoding to time-varying volumetric flow rates for each vessel using the Cardiovascular Angiography Analysis System (CAAS) software. During velocity segmentation, the velocity over the vessel's segmented area is integrated over the area to acquire flow rates. In other words, when the cross-sectional areas of the vessels are determined using computer-aided segmentation, time-varying volumetric flow rate data can be acquired from the velocity data by the following formula: $Q = A \cdot v$ with Q= flow rate [m^3/s], A= area [m^2], v= velocity [m/s].

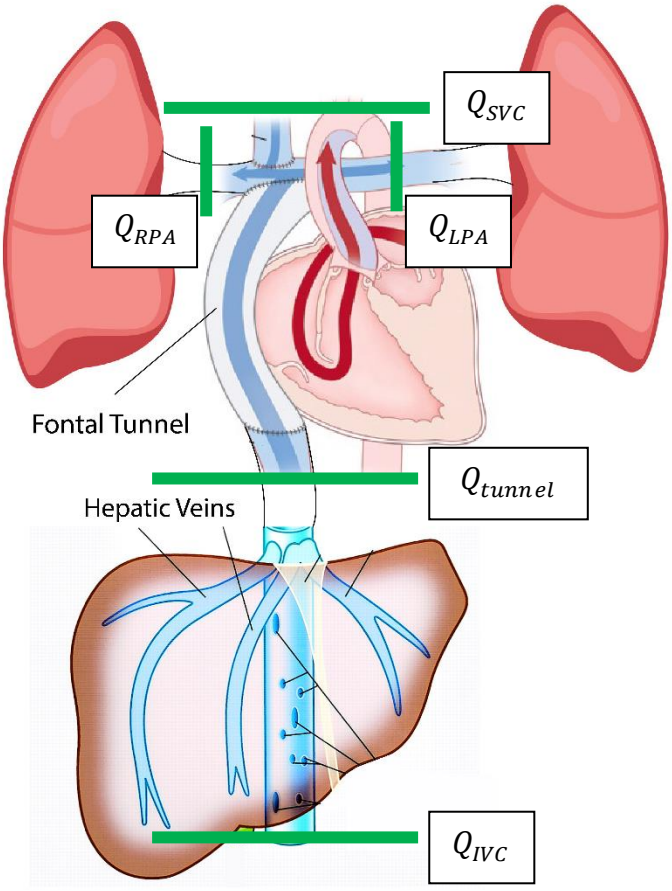

Figure 22: Overview of the 2D-3dir PC-MRI acquisition locations. SVC= superior vena cava, RPA= right pulmonary artery, LPA= left pulmonary artery, tunnel= Fontan tunnel, IVC= inferior vena cava

These time-varying flow rate waveforms were used to reconstruct the inlet and outlet boundary conditions of the different CFD models.

3.5.1 Inlet boundary conditions

The inlets of the CFD model were the IVC, SVC and the hepatic veins. Since the resolution of real-time PC-MRI is not yet good enough for the hepatic flow distribution, we were not able to measure the hepatic flow directly. However, since we aimed at quantifying the HFD while using particle tracing directly from the hepatic veins (novel approach), it was needed to simulate the blood flow from the hepatic veins. Therefore, we are the first that created 3D geometrical Fontan models that include the hepatic veins in the computational fluid domain. However, in order to simulate hepatic blood flow, patient-specific hepatic flow data is necessary. The solution for obtaining patient-specific hepatic flow data was to measure the hepatic blood flow indirectly by subtracting the flow of the IVC (Q_{IVC}) from the flow of the Fontan tunnel (Q_{tunnel}). By doing this, we indirectly knew the contribution of the hepatic blood flow through the hepatic veins (figure 22). This total hepatic blood flow (Q_{total_HV}) was subdivided over the different hepatic veins based on the ratio of their respective cross-sectional areas. The following equation was used:

$$Q_{total\_HV} = Q_{rhv} + Q_{mhv} + Q_{lhv} = Q_{tunnel} - Q_{IVC} \quad (3.2)$$

with Q_{total_HV} , Q_{rhv}, Q_{mhv}, Q_{lhv} , Q_{tunnel} , Q_{IVC} being respectively the total hepatic venous, the right, middle and left hepatic vein, Fontan tunnel and IVC flow.

Another important aspect of CFD modeling is that the flow rate waveforms prescribed at the inlet boundary conditions needed to be in phase and have a similar length of time. The flow rate waveforms extracted from the ECG-gated 2D-3dir PC-MRI data used in part A1 were already in phase. During ECG gating data is acquired continuously over the entire cardiac cycle for several heartbeats. Retrospectively, data of several heartbeats are synchronized and averaged to a velocity data set of one cardiac cycle. Since ECG-gated 2D-3dir PC-MRI provides an 'averaged' time-varying flow rate waveform for every vessel that starts at the same phase in the cardiac cycle, the time-varying flow rate waveforms of the different vessels were basically already in phase. The cardiac cycle was divided in 30 phases. However, the duration of the 30 different phases of the cardiac cycle could sometimes vary a few milliseconds between the different vessels within one patient. For example, the second phase of the cardiac cycle measured in the IVC could endure 28 ms, whereas this phase lasted for 27 ms in the Fontan tunnel. To address for this minimal phase-shift, we first normalized the time vectors of each blood vessel (meaning scale the time-vector values between 0 and 1). Based on these normalized time-vectors, the corresponding flow rate waveforms of the various inlet vessels were interpolated on each other to ensure equal time durations, which is necessary for proper CFD modeling. For interpolation we used the 'Pchip function' of MATLAB (The MathWorks, Inc., Natick, MA) that uses shape-preserving' piecewise cubic Hermite polynomial method to interpolate.

Regarding the real-time PC-MRI data used in part B2, it was a different story. Real-time PC-MRI considers both the respiratory and cardiac effects on blood flow rate waveforms. During real-time PC-MRI data is acquired without ECG gating (and navigator gating) for around 15 seconds. The velocity data is collected without any synchronizing or averaging steps. Therefore, the obtained time-varying flow rate waveforms of each vessel could start at any point in the cardiac cycle or respiratory cycle. For that reason, we had to interpolate the flow rate waveforms and correct the phase-shifts between the flow rate waveforms of the different inlet vessels in part B2. We decided to correct only the phase-shifts of the respiratory cycle between the time-varying flow rate waveforms for every vessel since research revealed, as stated before, that respiration is primarily responsible for the periodic flow rate changes (i.e, flow pulsatility) in Fontan patients. The cardiac contraction barely affects the pulsatility in Fontan patients[24,27,30,31,42]. Therefore the phase-correction of the cardiac cycle was considered less important in part B2. How we precisely correct the respiratory phase-shifts of the flow rate waveforms between different inlet vessels is described in part B2 because the technical aspects are highly detailed.

After phase-shift correction and interpolation, the flow rate waveforms of each inlet were implemented as boundary condition in the CFD models. In order to implement these time-varying flow rate waveforms of all inlets, they needed to be decomposed with MATLAB (The MathWorks, Inc., Natick, MA) into Fourier series:

$$Q(t) = a0 + \sum_{n=1}^{\infty} a_n \cos(\omega t) + \sum_{n=1}^{\infty} b_n \sin(\omega t) \quad (3.3)$$

Where:

$Q(t) = time\ varying\ volumetric\ flow\ rate\ [\frac{m^3}{s}]$

$a_n\ and\ b_n = Fourier\ coefficients$

$t = time\ [s]$

$\omega\ = angular\ frequency = \frac{2\pi}{T}\ [\frac{rad}{s}]$

$T = cardiac\ cycle\ or\ respiratory\ cycle\ period\ [s]$

These Fourier coefficients provided mathematical equations for each inlet vessel's time-varying flow rate waveform and were programmed in a user-defined-function, which could be loaded in the CFD solver ANSYS Fluent (v 17.1, ANSYS, Inc.).

Furthermore, as shown in chapter 2, the Womersley numbers could vary within one patient, ranging from 7.76 and 14.06. These Womersley numbers represent a more Womersley velocity profile. Nevertheless, Wei et al. concluded that no statistical differences were found between HFD, regions of low wall shear stress, power loss, viscous dissipation rate outcomes of Fontan simulations using Womersley, parabolic, or real velocity profiles. Moreover, it was recommended to use parabolic velocity profiles since they are satisfactorily surrogated for real velocity profiles in Fontan simulation, have low computational requirements and general applicability[79]. However, it should be noted that Wei et al. used the Fontan tunnel as the lowest boundary inlet instead of the hepatic veins and the IVC below the hepatic veins as applied in this master thesis project. Furthermore, this article defined HFD as the percentage of Fontan tunnel flow to the LPA (the conventional method). Nevertheless, in reference to this paper, parabolic velocity inlet profiles were implemented for all inlet boundary conditions in this master thesis project using the user-defined-function.

3.5.2 Outlet boundary conditions

The outlet vessels were the right and left pulmonary arteries. The outflow boundary conditions were imposed as a constant outflow ratio based on the average pulmonary flow distribution to the right and left lung measured with ECG-gated 2D-3dir PC-MRI[2]. The first step of calculating the outflow ratios was to ensure that the time and their corresponding flow vectors of the right and left pulmonary arteries were in phase and had the same length (duration) in a similar way as described above. The pulmonary flow distribution (PFD) to the left and right lung was calculated as follows: the measured flow of the left pulmonary artery and right pulmonary artery was divided by the total measured pulmonary artery flow for each of the 30 cardiac phases, using the following equations:

$$PFD\ (LPA) = \frac{Q_{LPA}}{Q_{LPA} + Q_{RPA}}, \qquad PFD\ (RPA) = \frac{Q_{RPA}}{Q_{LPA} + Q_{RPA}} \quad (3.4)$$

Where:

$PFD = measured\ pulmonary\ flow\ distribution$

$Q_{LPA} = measured\ flow\ through\ the\ left\ pulmonary\ artery\ [\frac{ml}{s}]$

$Q_{RPA} = measured\ flow\ through\ the\ right\ pulmonary\ artery\ [\frac{ml}{s}]$

Hereafter, the average PFD to the left and right pulmonary artery over the cardiac was calculated by summing up respectively the PFD(LPA) and PFD(RPA) of the 30 cardiac phases divided by 30. Based on the average PFD, outflow ratios to the right and left lung were prescribed. Since we have mass convergence, the sum of both ratios should, of course, be one. If the right pulmonary artery had side-branches, the right pulmonary artery flow was further subdivided based on their respective cross-sectional areas[16]. Unfortunately, it was impossible to acquire real-time PC-MRI data of high enough quality of the pulmonary arteries since these vessels were too small. Therefore, we have used ECG-gated 2D-3dir PC-MRI data of the pulmonary arteries to prescribe outflow ratios in both types of CFD models that ignore and consider respiratory effects on blood flow (respectively part A1 and part B2).

3.6 Treatment of vessel wall

The CFD simulations were performed using a rigid vessel wall assumption. Furthermore, no-slip conditions were prescribed at the wall. By assuming a rigid wall, the effect of the vessel wall compliance is not taken into account. Since, Long et al.[86] showed that vessel wall compliance barely affects the time-averaged HFD in Fontan simulations, we presume that this assumption would not affect our data However, HFD was mainly influenced by the 3D geometry instead of wall compliance.

3.7 Material properties

Blood is a non-Newtonian fluid and modeled using the Carreau model. The following values were chosen for the different parameters in the model : η_0=0.25 [Pa·s], η_∞= 0.0035 [Pa·s], λ=25 [s] and n = 0.25[54]. The fluid was supposed to have a density ρ = 1060 [kg/m3].[54]

3.8 Solver settings and discretization schemes

We used a pressure-based solver, which is usually used for incompressible flows. There are two types of algorithms among the pressure-based solvers: a segregated and coupled algorithm. The coupled algorithm resolves the pressure-based continuity and the momentum equations in a coupled approach. The advantage of the coupled algorithm is its significantly improved convergence speed compared to the segregated algorithm. However, the coupled algorithm uses more memory than the segregated algorithm. One of the coupled algorithms is the Semi-Implicit Method for Pressure Linked Equations (SIMPLE) algorithm, which has been used in this project. The discretization schemes were Least Square Cell-Based for gradients, a second-order for pressure, second-order upwind for momentum since second-order schemes provide higher-order accuracy. Additionally, a second-order implicit time integration scheme was selected, in which the equations are solved iteratively at each time step before simulating the next time step.

3.9 Simulation details

In part A1, we carried out unsteady CFD simulation for 7 cardiac cycles, simulating 1000 time steps per cardiac cycle. The outcomes of the last 4 cardiac cycles were used for the mixing assessment of hepatic and IVC flow and HFD quantification since it was found that periodic behavior was achieved after three cardiac cycles. In part B2, we also performed unsteady CFD simulation for 3 respiratory cycles, simulating 5000 time steps per respiratory cycle. The outcomes of the third respiratory cycle were used for the mixing assessment of hepatic blood and IVC flow and HFD quantification since it was found that periodic behavior was achieved after 2 respiratory cycles. No turbulence model was used since we assumed the blood flow to be laminar. The convergence criteria for continuity and x-y-,z- velocities were set to 1E-4. CFD solver software ANSYS- Fluent (v17.1, ANSYS, Inc) was used for all CFD simulations.

3.10 Post-processing

For post-processing, the velocity magnitude vectors for every mesh cell were written to an Ensight Gold case file per every 10 time steps as a binary format. Since we used 1000 time steps per cardiac cycle in part A1 and 5000 time steps per respiratory cycle in part B2: 1000/10 = 100 files per cardiac cycle and 5000/10 = 500 files per respiratory cycle were written and used for post-processing in part A1 and B2, respectively. The Ensight Gold case file could be converted to a '.case file' that could be loaded in the post-processing software Paraview (Paraview.org). In both types of CFD models that only considered the cardiac effects on blood flow (part A1) or included both the cardiac and respiratory effects on blood flow (part B2), we have evaluated: 1. Assessment of mixing between IVC and hepatic blood flow, and 2. HFD quantification.

3.10.1 Assessment of mixing between IVC and Hepatic blood flow

Since we were the first that quantified the mixing between hepatic and IVC blood flow within the Fontan tunnel, we have developed a mixing assessment method in collaboration with the TOP-FLOW consortium (*Department of Cardiology, Biomechanics laboratory, at Erasmus MC Rotterdam , the Pediatric Cardiology Department at Leiden University Medical Center and the Department of Chemical Engineering at the faculty of Applied Sciences of Delft University of Technology).* The degree of mixing between IVC and hepatic blood flow was evaluated at two cross-sections in the Fontan tunnel, perpendicular to the centerline. The first cross-section was chosen just above the hepatic veins junction into the IVC (i.e., caudal cross-section), the second cross-section was just below the pulmonary artery bifurcation (i.e., cranial cross-section). The mixing assessment between the IVC and hepatic blood flow relies on the spatial distribution of the hepatic and IVC blood flow in both cross-sections using the Lagrangian particle tracking tool of ParaView. To investigate the spatial distribution of the IVC and hepatic blood flow at both cross-sections, we first had to release particles from the level of the hepatic veins and the IVC that represented the flow of the respective blood vessels. Firstly, we subdivided 7500 massless particles over the hepatic veins proportional to flow of the hepatic veins. As mentioned before, because the total hepatic flow was subdivided over the different hepatic veins based on the ratio of their respective cross-sectional areas, we could also

subdivided the 7500 massless particles according to the respective cross-sectional areas of the hepatic veins. Previously described conventional methods usually used around 10.000 particles uniformly seeded in the Fontan tunnel[18]. To get a similar order of magnitude of particles within the Fontan tunnel, it was chosen to release 7500 particles from the level of hepatic veins, when combined with the particles of the IVC, would approximately provide a comparable range of particles. Secondly, based on the average measured flow ratio between IVC (below hepatic veins) and hepatic flow, the number of particles in the IVC was determined using the following formula:

$$7500 * \frac{Q_{IVC}}{Q_{total_{HV}}} \tag{3.5}$$

The particles that represented the hepatic and IVC flow were released simultaneously from the inlets of the hepatic veins and IVC. In the CFD models that only considered the cardiac effects on blood flow (part A1), particles were seeded continuously from the fourth simulated cardiac cycle. In the CFD models that considered both the cardiac and respiratory effects on blood flow (part B2), the particles were seeded continuously from the third simulated respiratory cycle. Since there was sometimes slow blood flow and because it was necessary that particles were able to reach the caudal and cranial cross-section, the assessment of mixing between hepatic and IVC blood flow was performed on the fifth cardiac cycle and the 'fourth' respiratory cycle. The fourth respiratory cycle is put in quotation marks because we only simulated three respiratory cycles in part B2, as stated in paragraph 3.9. However, we used the third respiratory cycle's velocity magnitude files again to create an additional 'fourth' respiratory cycle. This is a legitimate solution because, after three respiratory cycles, there was almost complete periodic behavior.

Furthermore, In the CFD models of part A1, the time step size used in the simulation was the cardiac cycle time divided by 1000. However, the velocity files were not written for every time step, but for every ten time steps, resulting in a Δt = cardiac cycle time/100 in ParaView. We chose not to write velocity files for every time step since the post-processing would take too long. The same goes for the CFD simulations in part B2, in which the following time step size was used: respiratory cycle time divided by 5000. However, the time step size Δt in ParaView was a factor 10 smaller: respiratory cycle time/500.

Based on these velocity magnitude vector files, ParaView created path lines, which are the trajectories that the individual particles follow over time. We considered caudal and cranial cross-section within the Fontan tunnel for the assessment of mixing between the hepatic and IVC flow. At both cross-sections in the Fontan tunnel, the path line transsections for every time step in the fifth cardiac cycle (in part A1) and in the third respiratory cycle (part B2) were registered and used in the mixing quantification (figure 23). In other words, the path lines in the cross-section for each time step represent the particles within the cross-section at that moment.

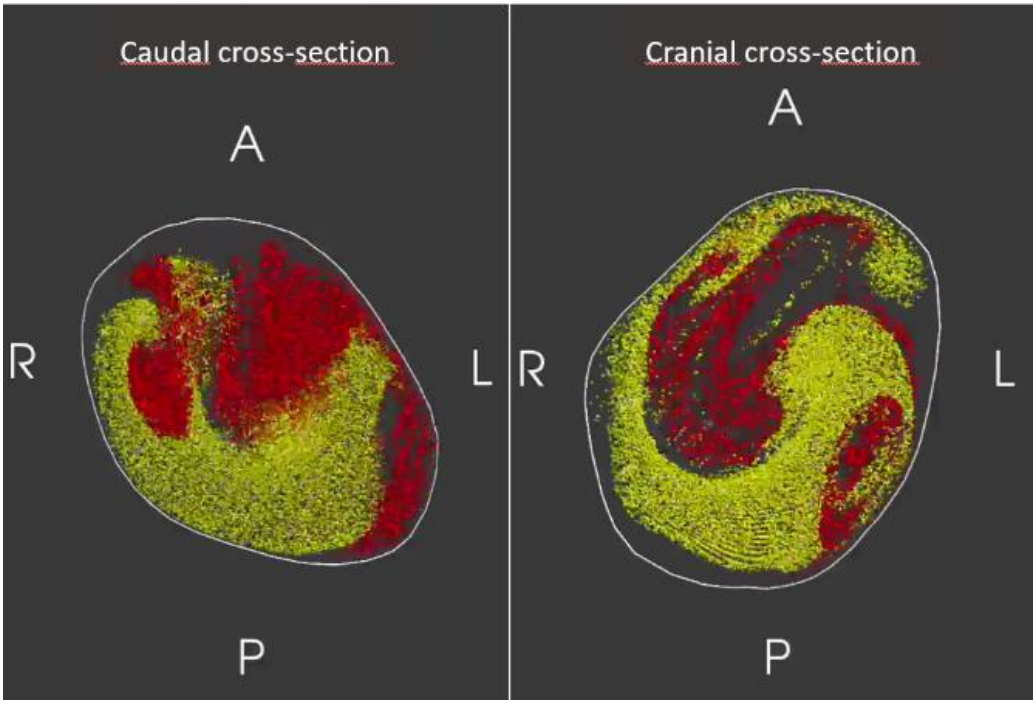

Figure 23:Caudal and cranial cross-section with yellow and red particles representing the IVC flow and hepatic blood flow, respectively

The first step of the mixing quantification was to determine the perfect situation of ideal mixing of hepatic with IVC blood flow in the entire cross-section. The ideal mixing was calculated by evaluating the ratio between the number of IVC and hepatic 'particle' path lines (i.e, the number of hepatic flow particles) and total number of path lines (i.e., total number of particles) in the entire cross-section for every time step in the cardiac or respiratory cycle. The ideal mixing ratio of flow in the hepatic veins ($P_{ideal\_mixing\_HV}$) and the ideal mixing ratio of IVC blood flow ($P_{ideal\_mixing\_IVC}$) are calculated as follows:

$$P_{ideal_{mixing_{HV}}} = \frac{P_{HV}}{P_{total}}, \in [0,1] \tag{3.6}$$

$$P_{ideal_{mixing_{IVC}}} = \frac{P_{IVC}}{P_{total}}, \in [0,1] \tag{3.7}$$

Where:

$P_{ideal\_mixing\_HV} = ideal\ mixing\ ratio\ of\ hepatic\ blood\ flow$

$P_{ideal\_mixing\_IVC} = ideal\ mixing\ ratio\ of\ IVC\ blood\ flow$

$P_{HV} = number\ of\ hepatic\ blood\ flow\ pathlines\ in\ entire\ crosssection$

$P_{IVC} = number\ of\ IVC\ flow\ pathlines\ in\ entire\ crosssection$

$P_{total} = P_{HV} + P_{IVC}$

The second step was to subdivide the caudal and cranial cross-sections in the Fontan tunnel in an anterior-posterior and right-left direction, leading to four sections in each cross-section: left-anterior, left-posterior, right-anterior and right-posterior. Hereafter, we quantified the

measured mixing ratio of each of these four sections per time step for both cross-sections in the Fontan tunnel as follows:

$$P_{measured_{mixing_{HV}}} = \frac{P^*_{HV}}{P^*_{total}} \ , \in [0,1] \tag{3.8}$$

$$P_{measured_{mixing_{IVC}}} = \frac{P^*_{IVC}}{P^*_{total}} \ , \in [0,1] \tag{3.9}$$

Where:

$P_{measured\_mixing\_HV} =$
$measured\ mixing\ ratio\ hepatic\ blood\ flow\ \ in\ each\ of\ the\ four\ sections$
$P_{measured\_mixing\_IVC} = measured\ mixing\ ratio\ IVC\ in\ each\ of\ the\ four\ sections$
$P^*_{HV} = number\ of\ hepatic\ blood\ flow\ pathlines\ in\ the\ section$
$P^*_{IVC} = number\ of\ IVC\ flow\ pathlines\ in\ the\ section$
$P^*_{total} = P^*_{IVC} + P^*_{HV}$ per section

Subsequently, the relative mixing ratio in every section for every time step was established. The definition of the relative mixing ratio is the ratio between the measured mixing ratio (within every section) and the ideal mixing (based on the entire cross-section). The following equations were used:

$$P_{relative_{mixing_{HV}}} = \frac{P_{measured_{mixing_{HV}}}}{P_{ideal_{mixing_{HV}}}} \tag{3.10}$$

$$P_{relative_{mixing_{IVC}}} = \frac{P_{measured_{mixing_{IVC}}}}{P_{ideal_{mixing_{IVC}}}} \tag{3.11}$$

Where:

$P_{relative\_mixing\_HV} = relative\ mixing\ ratio\ hepatic\ blood\ flow\ in\ the\ section$
$P_{relative\_mixing\_IVC} = relative\ mixing\ ratio\ IVC\ flow\ in\ the\ section$

Lastly, the degree of mixing between the hepatic and IVC blood in every section per time step was determined as the minimal value of the relative mixing ratios:

$$D_{mixing} = \min\left(P_{relative_{mixing_{HV}}}, P_{relative_{mixing_{IVC}}}\right), \in [0,1] \tag{3.12}$$

Where:

$D_{mixing} = Degree\ of\ mixing\ in\ each\ section$

Degree of mixing (D_{mixing}) of 0 means no mixing (the section contains only hepatic or IVC blood flow path lines) and 1 represents perfect mixing (the relative mixing ratio of hepatic with IVC blood flow path lines in the section is similar to the ideal mixing ratios). A degree of

mixing of 0.3, for instance, can be explained as 70% less path lines, either IVC or hepatic blood flow, are found in the section at that time step as expected according to the ideal mixing ratio. Consequently, we could use this parameter for the mixing quantification within each of the four sections at the caudal and cranial cross-section within the Fontan tunnel for every time step in the cardiac cycle (part A1) and the respiratory cycle (part B2).

However, during one cardiac or respiratory cycle, the amount of hepatic and IVC flow and so the degree of mixing in one section could vary substantially. Therefore, it was desirable to evaluate a time-averaged degree of mixing of every section. The time-averaged degree of mixing $D_{mixing\_average}$ was calculated for each of the four sections by using the average number of hepatic and IVC flow path lines present during the cardiac or respiratory cycle (i.e. taking the sum of hepatic and IVC flow path lines in each section for every time step in the cardiac or respiratory cycle divided by the total number of time steps in the cardiac or respiratory cycle). Finally, we also investigated the time-averaged degree of mixing of the entire cross-section ($D_{mixing\_average\_CS}$). Since each of the four sections was not exactly a quarter of the cross-section, we had to normalize the time-averaged degree of mixing of the section ($D_{mixing\_average}$) for every section's respective area. The $D_{mixing\_average\_CS}$ for the complete cross-section was calculated by taking the sum of the normalized $D_{mixing\_average}$ of every section divided by four. We have used the time-averaged degree of mixing of the entire cross-section ($D_{mixing\_average\_CS}$) for the final mixing quantification and statistical analyses. More details about the statistical analyses are found in part A1; however an example of one of the statistical analyses is that we statistically tested whether the degree of mixing of both cross-sections differed from perfect mixing.

3.10.2 Hepatic flow distribution (HFD) quantification

For HFD quantification, we did another separate post-processing step apart from the assessment of mixing between hepatic and IVC blood flow, as described above. For the HFD quantification, we used a well-established approach based on Lagrangian particle tracking, which has been reported in previous studies[19,87]. This Lagrangian particle tracking method used in the previous articles relies on analyzing individual massless particles and their trajectories described by the equations in chapter 2. We used three different HFD quantification methods; two conventional and one novel HFD quantification methods. In the two conventional methods ($HFD_{caudal\ tunnel}$ and $HFD_{cranial\ tunnel}$), 'hepatic blood flow particles' are uniformly seeded from two locations, either from a caudal or cranial cross-section within the Fontan tunnel. These two conventional methods represented, as stated before, the HFD quantification approaches that have been used in former studies. In contrast to the conventional HFD quantification method, particles are directly seeded from the level of the hepatic veins (HFD_{HV}) in the novel method.

To analyze the effect of the different HFD quantification methods (conventional versus novel), we released another 7500 massless particles, representing the hepatic blood flow, either from the level of one of both cross-sections ($HFD_{caudal\ tunnel}$ and $HFD_{cranial}$) or directly from the inlets of the hepatic veins (HFD_{HV}). In the conventional methods, these 7500 particles were evenly seeded from the cross-sections. In the novel method, the 7500 particles were divided over the hepatic veins based on the ratio of their respective cross-sectional areas. Figure 24 shows the different HFD quantification methods. Subsequently, the HFD ($HFD_{caudal\ tunnel}$,

$HFD_{cranial\ tunnel}$ and HFD_{HV}) towards the left and right lung was computed by counting the number of particles leaving the left pulmonary artery and right pulmonary artery and expressed as a percentage of the total particles that were seeded [19]:

$$HFD\ (LPA) = \frac{P_{LPA}}{P_{RPA} + P_{LPA}} * 100\%\ , \qquad HFD\ (RPA) = \frac{P_{RPA}}{P_{RPA} + P_{LPA}} * 100\% \quad (3.13)$$

Where:

$HFD = hepatic\ flow\ distribution$

$P_{LPA} = amount\ of\ particles\ leaving\ through\ left\ pulmonary\ artery$

$P_{RPA} = amount\ of\ particles\ leaving\ through\ right\ pulmonary\ artery$

$Total\ amount\ of\ particles = P_{LPA} + P_{RPA}$

In the CFD models that only consider the cardiac effects on blood flow (part A1), the particles were seeded during the fourth simulated cardiac cycle. In the CFD simulations that took both the cardiac and respiratory effects on blood flow into account (part B2), the particles were seeded during the third simulated respiratory cycle. The particles were released for 100 time steps and 500 time steps in part A1 and part B2, respectively, representing one cardiac cycle and respiratory cycle. Since there could be slow blood flow in part A1, we needed the simulation files of cardiac cycles 5, 6 and 7 to ensure the particles had enough time to reach all the way op to the left and right pulmonary arteries. The hepatic blood flow in part B2 was faster than in part A1 due to the respiratory component. In part B2, a fourth respiratory cycle was required for letting the particles arrive at the left and right pulmonary arteries. Since, in part B2, we had only the velocity magnitude files of three respiratory cycles, we used the velocity magnitude files of the third respiratory cycle again and added these as an extra 'fourth' respiratory cycle.

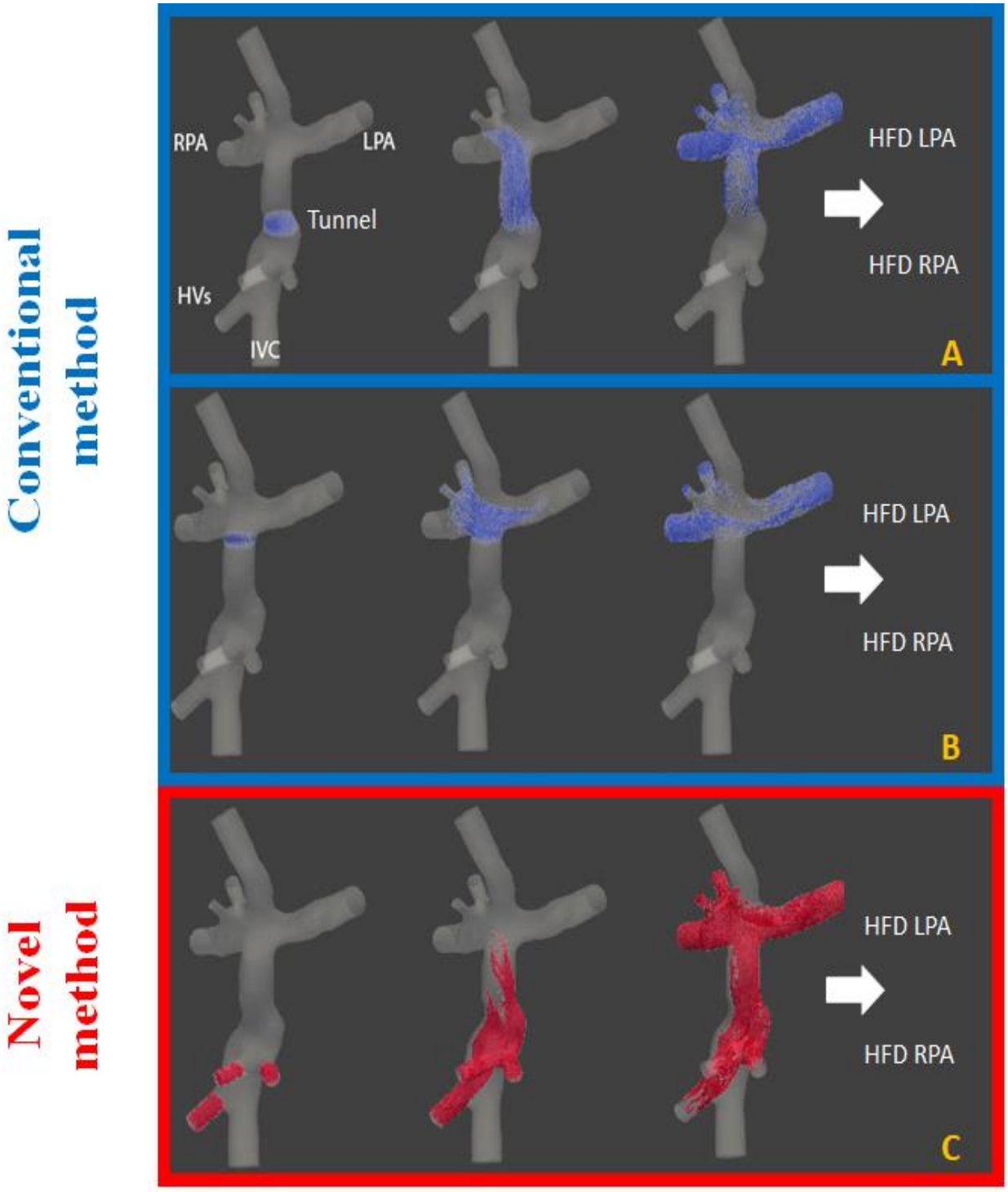

Figure 24: The three seeding locations for HFD quantification. 24A: uniformly particle seeding over the caudal cross-section (conventional method), 24B: uniformly particle seeding over the cranial cross-section (conventional method), 24C: direct particle seeding from the level of the hepatic veins (novel method). HFD was measured by counting the number of particles leaving the left pulmonary artery (HFD LPA) or right pulmonary artery (HFD RPA). IVC; inferior vena cava, HVs; hepatic veins, LPA: left pulmonary artery, RPA: right pulmonary artery, Tunnel: Fontan tunnel, HFD: hepatic flow distribution

3.11 Verification and validation of CFD models

Verification includes evaluating if the programming code and the implementation of the CFD model are correct. Validation means checking if there is a good agreement between the CFD simulation outcomes and real patient data to ensure that the CFD models accurately represent the Fontan circulation.

One important verification step was to inspect if the user-defined-function was programmed correctly. As stated before, based on an article of Wei et al, parabolic velocity inlet profiles were implemented for all inlet boundary conditions. After simulation of one CFD case, we loaded the velocity files in ParaView and analyzed the inlet velocity profile of each inlet. As can be seen from figure 25 , the inlet showed a perfect parabolic inlet profile (red = high velocity, blue = low velocity), just as was imposed in the user-defined-function file. Another verification step was that we continuously verified the MATLAB code if the MATLAB code extracted, interpolated and phase-shift corrected the time-varying flow rate waveforms correctly the way we expected.

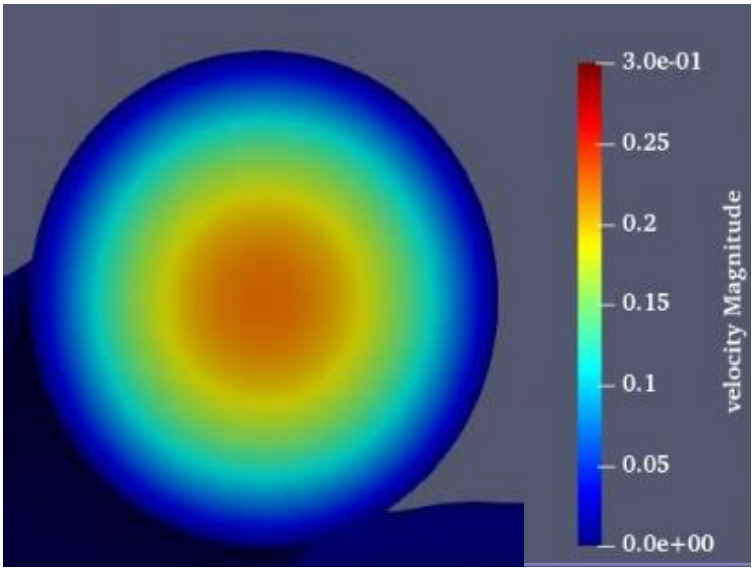

Figure 25: Simulated velocity profile of the IVC of one Fontan case. The velocity profile is parabolic, just as was imposed.

Additionally, we have applied a validation step on all CFD models used in part A1 and part B2. The validation step was to check if the averaged volumetric flow rate of the IVC computed with CFD agreed with the measured averaged volumetric flow rate obtained from the ECG-gated 2D-3dir PC-MRI and real-time PC-MRI acquisitions. Furthermore, we compared the averaged flow through LPA calculated with CFD to the averaged measured LPA flow extracted from PC-MRI. Because we needed to have mass convergence in the CFD system, we defined the measured LPA flow as the sum of the measured Fontan tunnel and SVC flow (which is total flow in the Fontan circulation) extracted from 2D-3dir ECG-gated PC-MRI (part A1) or real-time PC-MRI (part B2) times the outflow ratio prescribed for the LPA. The 'real' LPA flow measured with 2D-3dir PC-MRI was only used for calculating the outflow ratio.

3.11.1 Validation CFD models of part A1 (only cardiac dependent flow)

Table 2 shows the validation of the LPA flow of part A1, which CFD models only encountered cardiac effects on blood flow. The difference between the computed and measured average LPA flow were a maximum 2 percent.

Table 2: Validation CFD models of part A1 (only cardiac dependent flow)

Patient	Average LPA flow measured with PC-MRI (m3/2)	LPA computed with CFD (m3/s)	Difference
1*	2.10e-5	2.09e-5	0.6%
2	3.22e-5	3.19e-5	0.9%
3	8.42e-6	8.41e-6	0.1%
4	2.65e-5	2.66e-5	0.4%
5	2.76e-5	2.74e-5	0.7%
6	1.52e-5	1.50e-5	1.3%
7	2.32e-5	2.32e-5	0.0%
8	3.64e-5	3.63e-6	0.3%
9	3.21e-5	3.24e-5	0.9%
10	1.58e-5	1.59e-5	0.6%
11	2.02e-5	2.02e-5	0.0%
12	2.86e-5	2.87e-5	0.3%
13	2.09e-5	2.09e-5	0.0%
14	1.39e-5	1.39e-6	0.0%
15	5.28e-5	5.27e-5	0.2%

*patient 1 had a situs inversus (in which the tip of the heart (apex) is on the right side of the thorax), so we used the RPA flow instead of the LPA flow.

3.11.2 Validation CFD models of part B2 (cardiac and respiratory dependent flow)

Table 3 demonstrates the validation of the LPA flow of part B2, which CFD models considered both the cardiac and respiratory effects on blood flow. Initially, in the first three cases, which are included in this master thesis report, we compared the measured LPA flow after phase-shift correction and interpolation with the computed LPA flow with CFD (B versus C), which needed to be below 2 percent. Because of the interpolation and phase-shift correction, the final end time of inspiration can sometimes a bit longer than measured in the individual blood vessel. For instance, if the SVC and IVC both have a longer inspiratory phase than the Fontan tunnel flow, the inspiratory phase of the Fontan tunnel flow after phase-shift correction and interpolation, which was needed for CFD implementation, will increase a little bit as well. Consequently, since inspiration increases the Fontan tunnel flow, the average 'measured' Fontan tunnel flow enlarges after phase-shift correction and interpolation. This increase of Fontan tunnel flow will eventually enlarge the LPA flow – as shown in the table 3– and the RPA flow. However, although the absolute flow magnitude might increase due phase-shift correction and interpolation, the pulmonary flow distribution to left and right lung as measured with real-time PC-MRI were validated to be still correct. Therefore, it is not entirely fair to compare the real average LPA flow magnitude measured with PC-MRI to the average computed LPA flow magnitude with CFD (A versus C). However, although not included in this master thesis, from cases 4 onward, we also tried to consider the differences between A and C by applying an extra programming step, as described in the recommendation of part B2. As you can see from table 3, this additional programming step reduced the difference between the average LPA flow measured with PC-MRI and the average computed LPA flow with CFD for all following cases to below 2 percent.

Table 3: Validation CFD models of part B2 (cardiac and respiratory dependent flow)

Patient	A= average LPA flow measured with PC-MRI (m3/s)	B= average 'measured' LPA flow after phase-shift correction and interpolation of the flow with the other blood vessels (m3/s)	C= average computed LPA flow with CFD (m3/s)	Differences between A&B and B&C.
1*	2.47e-5	2.59e-5	2.59e-5	4.8%, 0.0%
2	8.96e-6	9.35e-6	9.34e-6	4.2%, 0.1%
3	3.41e-5	3.49e-5	3.49e-5	2.3%, 0.0%
4	3.83e-5	3.76e-5	3.76e-5	1.8%, 0.0%
5	3.37e-5	3.37e-5	3.37e-5	0.0%, 0.0%
6	2.06e-5	2.02e-5	2.02e-5	1.9%, 0.0%
7	2.23e-5	2.26e-5	2.26e-5	1.3%, 0.0%
8	4.44e-5	4.48e-5	4.48e-5	0.9%, 0.0%

*patient 1 had a situs inversus (which means the tip of the heart (apex) is on the right side of the thorax), so we used the RPA flow instead of the LPA flow.

Grey color : the outcomes of case 4 to 8 are not included in this master thesis.

Part A1.

The assessment of mixing between hepatic and inferior vena cava blood flow & hepatic flow distribution quantification

The outcomes of part A1 are used in a scientific article written by F.M. Rijnberg, medical PhD of Leiden University Medical Center. We provided the technical part for this article, and this has led to a second co-authorship for me on this paper, which makes me very proud.

Introduction

Recent CFD studies indirectly quantify HFD to the left pulmonary artery and right pulmonary artery by tracking 'hepatic flow' particles that are uniformly seeded in the Fontan tunnel and analyzing the distribution of these particles towards both lungs (the *conventional approach*) [18–22]. However, this conventional approach is based on an unvalidated assumption that there is a uniform distribution of hepatic blood in the Fontan tunnel. Because Reynolds numbers in the Fontan tunnel are low, the blood flow in the Fontan tunnel behaves laminar. Due to this laminar flow behavior, the mixing of blood from the hepatic veins and the IVC might be far from optimal contrary to what is generally assumed and so the question rises whether this assumption of uniform hepatic flow distribution within the Fontan tunnel is correct. Moreover, using this assumption of even distribution of hepatic flow in the Fontan tunnel could potentially cause inaccuracies in HFD quantification. Therefore, this study aimed to test this assumption of uniform distribution of hepatic blood flow within the Fontan tunnel. To achieve this, we created patient-specific CFD models that included the geometry of the hepatic veins into the computational fluid domain. These CFD models that incorporated the hepatic veins made it possible to seed 'hepatic flow' particles directly from the level of the hepatic veins (*the novel approach*). We supposed that seeding 'hepatic flow 'particles directly from the level of the hepatic veins would provide physiologically more realistic hepatic blood flow patterns. Another objective was to quantify and compare the HFD outcomes when particles were uniformly seeded from a cross-section within the Fontan tunnel (the conventional approach) and were seeded from the level of the hepatic veins (the novel approach). In part A1 we used free-breathing ECG-gated 2D-3dir PC-MRI acquisitions to reconstruct the boundary conditions in the CFD models. Due to ECG-gating, the respiratory effects on blood flow are ignored. Consequently, part A1 only considered the cardiac impact on blood flow in the CFD simulations. Part A1 hypothesized that hepatic blood is non-uniformly distributed within the Fontan tunnel, which affects the precision of HFD quantification with the conventional approach.

Methods

Study group

A comprehensive description of the method is found in chapter 3. Here is a brief outline of the method of part A1. The Fontan patients involved in part A1 of the master thesis were identified from the Leiden University Medical Center database. Fifteen single ventricle patients with a TCPC-type (Fontan) tunnel and age above eight were included. The patient characteristics are found in table 4. Informed consent was obtained from all patients, and Leiden University Medical Center approved the protocol.

Table 4: Patients characteristics of the entire cohort

Characteristics of patient cohort (n=15)	
Male/Female	9/6
Age (years)	18.2 (5.6)
Fontan type (ECC/LT)	14/1

CFD simulations

We created 3D reconstructions of patient-derived Fontan anatomy that included the geometry of the hepatic veins in the computational fluid domain (see chapter 3). ECG-gated 2D-3dir PC-MR images were acquired under free-breathing conditions to assess time-varying volumetric flow rates of the IVC, SVC, Fontan Tunnel, right pulmonary artery and left pulmonary artery and were used to reconstruct the inlet and outlet boundary conditions. A detailed prescription of how we reconstructed the boundary conditions are described in chapter 3. Time-varying flow rates were imposed with a parabolic velocity profile at all inlet vessels (IVC, SVC and hepatic veins)[79]. The outflow boundary conditions (left pulmonary artery and right pulmonary artery) were imposed as an outflow ratio based on the average measured pulmonary flow distribution extracted from ECG-gated 2D-3dir PC-MRI data. A polyhedral mesh with a four boundary prism layer at the vessel wall was used[72]. The mesh element size was based on the average diameter of all inlet and outlet vessel diameters divided by 30 (range 0.4-0.5mm elements)[72]. The density of the blood was set to 1060 [kg/m3]. Blood was modeled as a non-Newtonian fluid using a Carreau model[54] (chapter 3). No turbulence model was used since we assumed the blood flow to be laminar. The convergence criteria for continuity and x-y-,z-velocities were set to 1E-4. CFD solver software ANSYS- Fluent was used for all CFD simulations. In part A1, we carried out unsteady CFD simulation for seven cardiac cycles, simulating 1000 time steps per cardiac cycle. The outcomes of the last four cardiac cycles were used for the assessment of mixing between hepatic and IVC blood flow and HFD quantification since it was found that periodic behavior was achieved after simulation of three cardiac cycles.

Post-processing

For post-processing, the velocity magnitude vectors for every mesh cell were written to an Ensight Gold case file per every ten time steps as a binary format. Since we used 1000 time steps per cardiac cycle, 1000/10 = 100 files per cardiac cycle were written and used for post-processing.

The assessment of mixing between hepatic and IVC blood flow

We released particles from the hepatic veins and IVC level for the assessment of mixing between the hepatic and IVC blood flow and investigated the degree of mixing at two cross-sections within the Fontan tunnel. The first cross-section was chosen just above the hepatic veins junction (i.e., caudal cross-section), the second cross-section was just below the pulmonary artery bifurcation (i.e., cranial cross-section). The quantification of mixing between the IVC and hepatic blood flow relies on the spatial distribution of both flows at both cross-sections using the Lagrangian particle tracking tool of Paraview. Based on these velocity magnitude vector files, Paraview created path lines, which are the trajectories that the individual particles follow over time. At both cross-sections, the path line transsections for every time step were registered and used in the mixing analysis. Furthermore, we divided each cross-section in four sections: left-anterior, right-anterior, left-posterior and right-posterior. For the assessment of mixing between hepatic and IVC blood flow, we used the time-averaged degree of mixing per each of the four sections over one respiratory cycle ($D_{mixing\_average}$)

and the time-averaged degree of mixing of both entire caudal and cranial cross-sections over one respiratory cycle ($D_{mixing\_average\_CS}$), as explained in detail in chapter 3.

HFD quantification

The second post-processing step was to analyze and compare the HFD towards the lungs between the novel and conventional HFD quantification methods using the Lagrangian particle tracking tool of Paraview. In the two *conventional methods* ($HFD_{caudal\ tunnel}$ & $HFD_{cranial\ tunnel}$), hepatic blood flow particles were uniformly seeded from either a caudal or cranial cross-section, whereas in the *novel method*, particles were directly seeded from the level of the hepatic veins (HFD_{HV}). Chapter 3 explains both the conventional and novel HFD quantification approaches in detail. The HFD ($HFD_{caudal\ tunnel}$, $HFD_{cranial\ tunnel}$ and HFD_{HV}) towards the left and right lung was computed by counting the number of particles leaving the left pulmonary artery and right pulmonary artery and expressed as a percentage of the total particles that were seeded.

Statistics

As part of the TOP-FLOW consortium, we provided most of the engineering side within this project. Leiden University Medical Center performed statistical analyses on the outcomes of the 15 simulated cases. Since the statistical findings were interesting, a few outcomes are highlighted below. SPSS 25.0 (IBM-SPSS, Chicago, IL) and Prism 8.0 (Graphpad Software, La Jolla, CA) were used for data analysis. Continuous data were reported as mean ± standard deviation.

The assessment of mixing between hepatic and IVC blood flow

For statistical analyses, the degree of mixing ($D_{mixing\_average}$, $D_{mixing\_average\_CS}$) was subdivided into six categories: no mixing <0.1, poor mixing 0.1-0.3, mild mixing 0.3-0.5, moderate mixing 0.5-0.7, good mixing 0.7-0.9, uniform mixing >0.9. A paired t-test was used to compare measurements.

HFD comparison between conventional and novel method

Furthermore, Bland-Altman plots (or difference plots) and intraclass correlation (ICC) analysis were applied to evaluate the agreement between the different HFD quantification methods (moderate <0.7, good ≥0.7-0.9 and excellent >0.9). The Bland-Altman plot is commonly used for investigating the agreement of two methods with quantitative outcomes. The horizontal lines drawn in the Bland-Altman plot are at the mean difference and at the limits of agreement. The limits of agreement are defined as the mean difference ± 1.96 times the standard deviation (SD) of the differences. However, the mean difference is the average difference between all values (negative and positive) on the Bland-Altman plot, meaning the negative and positive values could average out that mean difference on the plot. For example, if there exists one value of +10 and another value of -10, the mean difference is zero. Therefore, we also considered the mean *absolute* difference. We used the mean absolute difference (± 1.96 standard error of the mean) between methods to evaluate the absolute amount of which one HFD quantification approach over or underestimates the other HFD quantification approach. Percentage points

were used to describe the differences. A paired t-test was used to compare the measurements of the different HFD quantifications methods. P values <0.05 were considered statistically significant.

Results

First, the outcomes of the entire group of 15 Fontan patients are presented. Secondly, the results of three subjects of the cohort are pointed out separately since these patients were also investigated during the studies described in chapter part B2, which made it easier to compare the CFD results between part A1 and B2. In part A1, we only took the cardiac effects on blood into account, whereas the CFD models in part B2 considered both the cardiac and respiratory effects on blood flow.

Results of the entire group

The assessment of mixing between hepatic and IVC blood flow

As illustrated in figures 26,27,28, and 29, there was an obvious hepatic bloodstream pattem within both cross-sections during the entire cardiac cycle, leading to an uneven distribution of hepatic blood flow in the Fontan tunnel. This hepatic bloodstream pattern was most noticeable in the caudal cross-section. This observation was supported by the time-averaged degree of mixing of the entire cross-section ($D_{mixing\_average\_CS}$), as presented in table 5. The time-averaged degree of mixing of the entire caudal and cranial cross-section were moderate mixing (mean 0.66 ±0.13) and good mixing (mean 0.79 ±0.11), respectively. This difference in degree of mixing between the caudal and cranial cross-section was significant, demonstrating a better mixing of hepatic and IVC blood flow more downstream in the Fontan tunnel. Moreover, the degree of mixing at the caudal and cranial level of the Fontan tunnel were statistically different from 0.9 (i.e., uniform mixing) with p-values of < 0.001 and 0.012, respectively. These findings demonstrate that the hepatic flow is non-uniformly distributed within the Fontan tunnel.

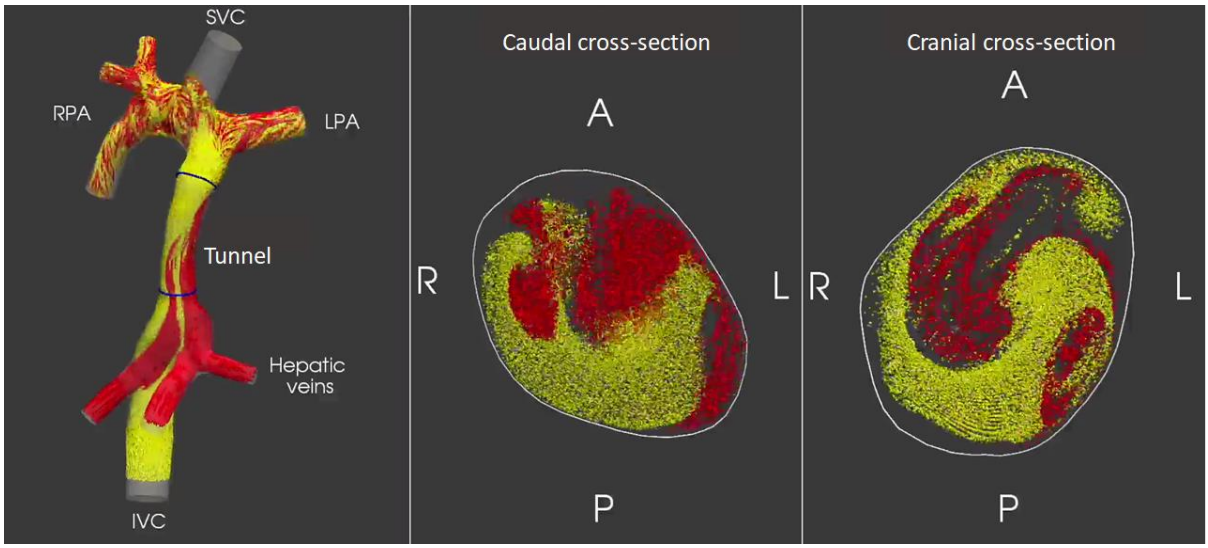

Figure 26: Hepatic (red) and IVC (yellow) bloodstreams at caudal and cranial level at the beginning of the cardiac cycle

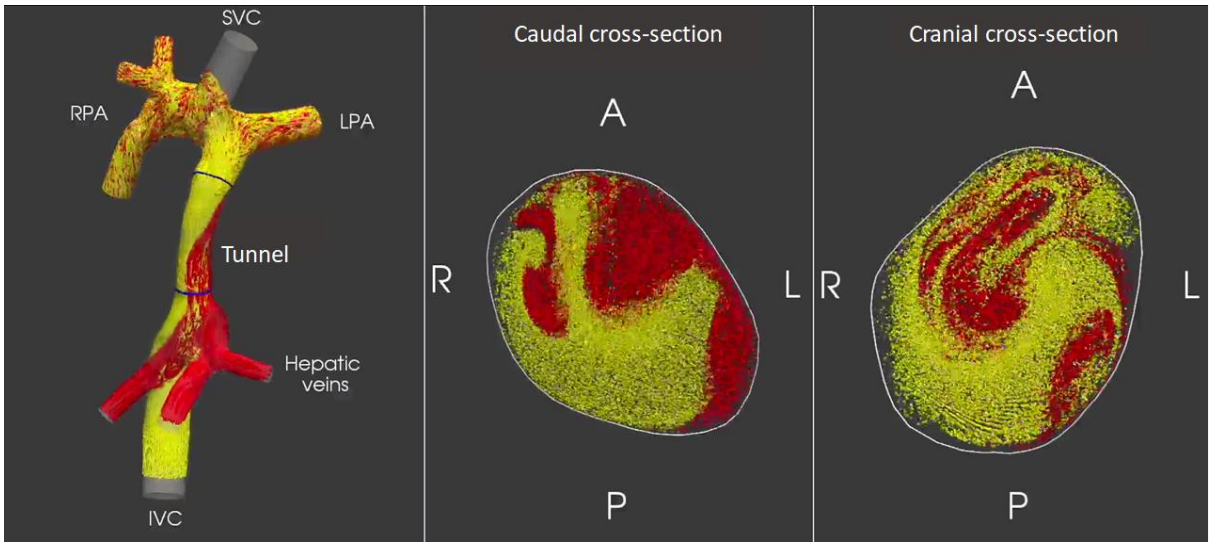

Figure 27: Hepatic (red) and IVC (yellow) bloodstreams at caudal and cranial level around the midpoint of the cardiac cycle

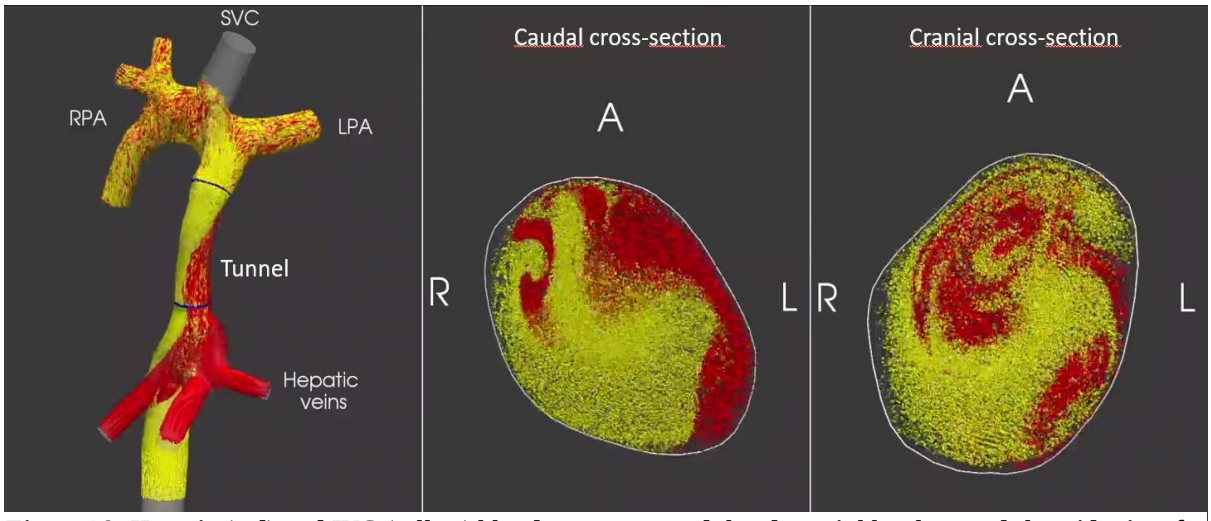

Figure 28: Hepatic (red) and IVC (yellow) bloodstreams at caudal and cranial level around the midpoint of the cardiac cycle

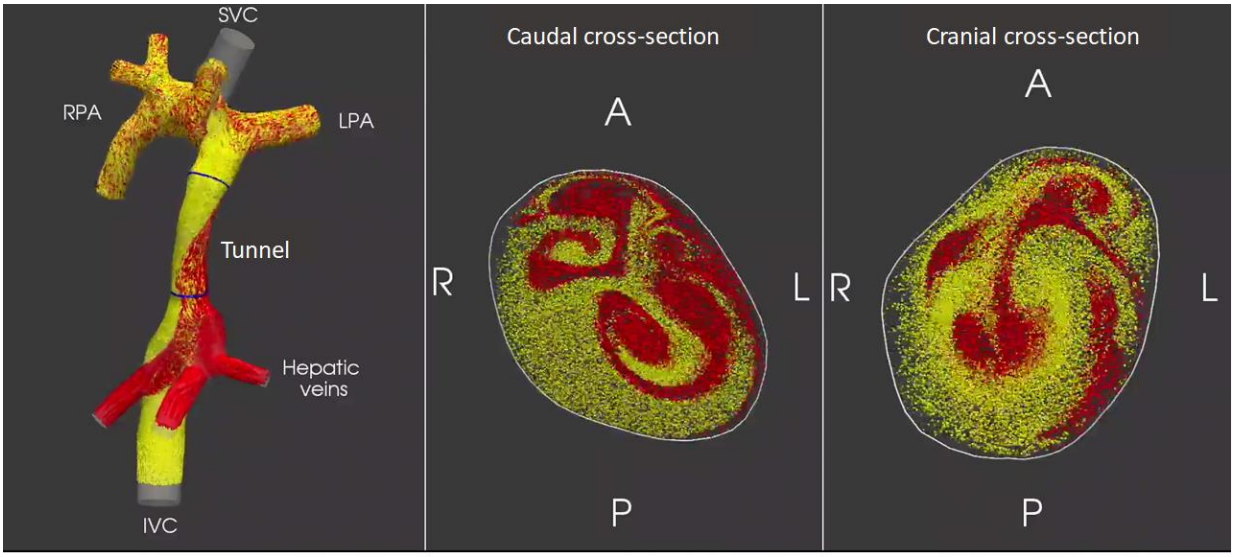

Figure 29: Hepatic (red) and IVC (yellow) bloodstreams at caudal and cranial level at the end of the cardiac cycle

Table 5: Time-averaged degree of mixing of the entire cross-section on cohort-level

Cross-section	**Time-averaged degree of mixing of the entire cross-section** ($D_{mixing\_average\_CS}$)
Caudal	mean 0.66 ± 0.13 = moderate
Cranial	mean 0.79 ± 0.11 = good mixing

HFD quantification

Table 6 demonstrates the outcomes of the HFD quantification and comparison between the three methods. There was no significant difference between the HFD quantification of both conventional approaches: $HFD_{caudal\ tunnel}$ (48.2±21.9%) and $HFD_{cranial\ tunnel}$ (48.0±21.9%), mean difference 0.2% (95%CI -6.0 – 6.4), p=0.80. However, a significant difference was found when comparing both conventional methods with the novel method. The HFD_{HV} was 51.0±20.6%. The mean difference between HFD_{HV} and $HFD_{caudal\ tunnel}$ was 2.9% (95%CI -6.3 – 12.0), p=0.033. The mean difference between HFD_{HV} and $HFD_{cranial\ tunnel}$ was 3.1% (95%CI -7.4 – 13.6), p=0.044. Furthermore, we evaluated the mean absolute difference between the different HFD quantification methods, describing the absolute amount of which one HFD approach over- or underestimates the other HFD approach. When comparing both conventional methods, we found a mean absolute difference of 2.4% (95%CI 1.3-3.4). However, a higher mean absolute difference was discovered between the HFD quantification of the novel and conventional methods: HFD_{HV} versus $HFD_{caudal\ tunnel}$ 4.6% (95%CI 3.1-6.0), HFD_{HV} versus $HFD_{cranial\ tunnel}$ 4.4 % (95%CI 2.2-6.5). These findings confirmed the hypothesis that, when particles are seeded directly from the hepatic veins, it significantly affects the HFD quantification compared to the conventional HFD quantification approaches. On the other hand, the mean absolute differences between the novel and the conventional HFD quantification methods were relatively small; in most cases, less than 5% for 8 out of 15 and 11 out of 15 when comparing HFD_{HV} with respectively $HFD_{caudal\ tunnel}$ and $HFD_{cranial\ tunnel}$. Interestingly, when considering individual patients, differences between the novel and

conventional HFD quantification as high as 14.9% were noticed. In that specific case, the HFD towards the left lung was 20.7% and 35.6% using the respective HFD quantification methods $HFD_{cranial\ tunnel}$ and HFD_{HV}.

Furthermore, using the sub-analysis, we concluded that there was no significant relationship between the mean absolute difference in HFD between the novel and conventional approaches and the $D_{mixing\_average\_CS}$ at the caudal and cranial level: r = 0.32, p = 0.27 and r = -0.06, p = 0.82, respectively. Additionally, we discovered no correlation between the percentage of hepatic to total Fontan tunnel flow contribution and the mean absolute difference in HFD value between the three HFD quantification methods.

Table 6: Outcomes of comparison between HFD quantification methods

	Paired t-test	**Bland-Altman**		**Intraclass Correlation**	**Mean absolute difference**
Comparisons		Mean difference	LoA	ICC	(± 1.96 SEM)
HFD_{HV} vs $HFD_{caudal\ tunnel}$	p=0.033	2.9	-6.3 – 12.0	0.97	4.6 (3.1-6.0)
HFD_{HV} vs $HFD_{cranial\ tunnel}$	p=0.044	3.1	-7.4 – 13.6	0.96	4.4 (2.2-6.5)
$HFD_{caudal\ tunnel}$ vs $HFD_{cranial\ tunnel}$	p=0.80	0.2	-6.0 – 6.4	0.99	2.4 (1.3-3.4)

HFD; hepatic flow distribution towards the left pulmonary artery.
SEM; standard error of the mean, LoA; limits of agreement, defined as the mean difference ± 1.96 standard deviations. ICC: intraclass correlation.

Results of three pointed out cases

Table 7 shows the patient characteristics of the three-pointed out cases.

Table 7: Patient characteristics of three cases

Patient characteristics of 3 cases	**CASE 1**	**CASE 2**	**CASE 3**
Gender	Male	Male	Male
Age (years)	17.5	18.1	18.2
Type TCPC tunnel	ECC	ECC	ECC
Diameter size of tunnel (mm)	16	18	16

The assessment of mixing between hepatic and IVC blood flow

Table 8 demonstrates the outcomes of the time-averaged degree of mixing of the entire cross-section for cases 1, 2 and 3 over the cardiac cycle. Figure 30 and 31 demonstrates the time-varying degree of mixing per each of the four sections of the caudal and cranial cross-section over the cardiac cycle. As shown from table 8 and figures 30 and 31, all cases had a higher degree of mixing between the hepatic and IVC blood flow in the cranial cross-section than in the caudal cross-section. The caudal degree of mixing ranged from 0.49 to 0.70, whereas the cranial degree of mixing varied between 0.58 and 0.86.

Table 8: Time-averaged degree of mixing of the entire cross-section for three cases over one cardiac cycle for CFD models that only consider cardiac effects on blood flow

CASE	Cross-section	Degree of mixing of entire cross-section
Case 1	Caudal	0.49
	Cranial	0.58
Case 2	Caudal	0.70
	Cranial	0.86
Case 3	Caudal	0.70
	Cranial	0.86

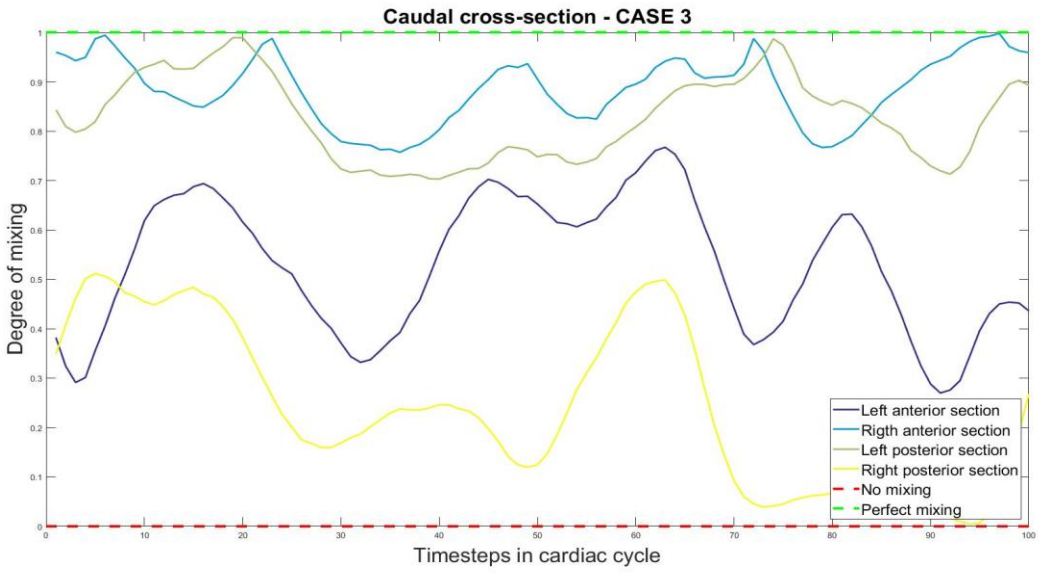

Figure 30: Time-varying degree of mixing for each of the four section of the caudal cross-section of Case 3 over the cardiac cycle

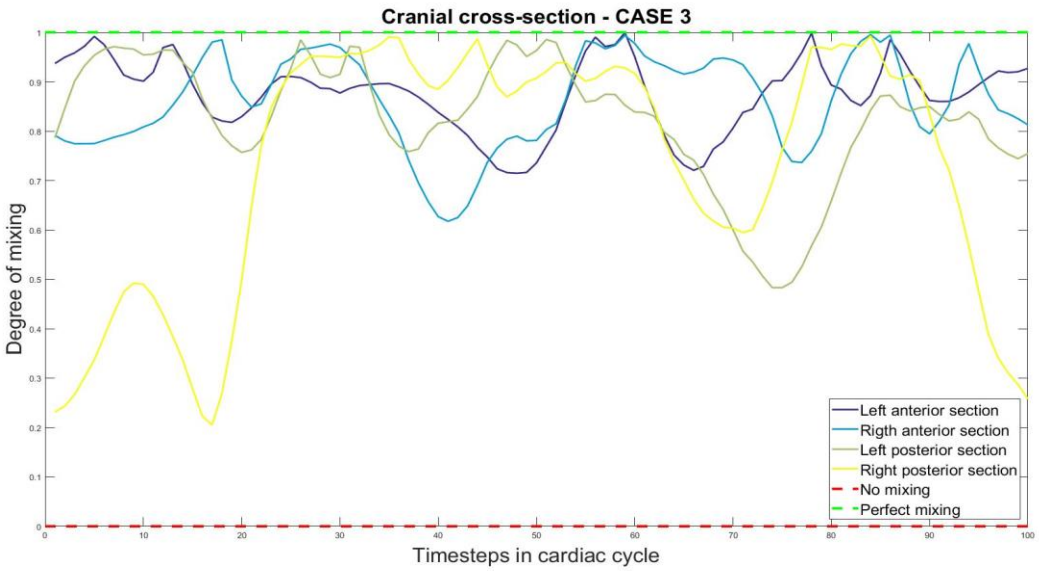

Figure 31: Time-varying degree of mixing for each of the four section of the cranial cross-section of Case 3 over the cardiac cycle

HFD quantification

The results of HFD quantification of the different methods for 3 cases are presented in table 9. It can be clearly seen that there were different HFD outcomes between the conventional and novel HFD quantification methods. For instance, concerning case 1, a 9.05% difference between the $HFD_{caudal\ tunnel}$ and HFD_{HV} was found.

Table 9: Outcomes of HFD quantification of the different methods for three cases over one cardiac cycle

	$HFD_{caudal\ tunnel}$ (LPA)	$HFD_{caudal\ tunnel}$ (RPA)	$HFD_{cranial\ tunnel}$ (LPA)	$HFD_{cranial\ tunnel}$ (RPA)	HFD_{HV} (LPA)	HFD_{HV} (RPA)
Case 1	61.57%	38.43%	63.75%	36.25%	66.62%	33.38%
Case 2	17.35%	82.65%	17.69%	82.31%	26.40%	73.60%
Case 3	54.65%	45.35%	61.11%	38.89%	57.81%	42.19%

Discussion

We were the first that included the hepatic veins into the computational fluid domain of patient-specific CFD models of (TCPC-type) Fontan patients. The main objectives were 1. evaluate the degree of mixing between the hepatic and the IVC blood flow in the Fontan tunnel and 2.quantify HFD using particle tracing directly from the hepatic veins (the novel approach), and compare results with the conventional approach. The key results were: we have shown that there is a non-uniform distribution of hepatic blood flow in the Fontan tunnel. This non-uniform distribution was most noticeable in the caudal cross-section (just above the junction of hepatic veins with the IVC). There was a significantly higher degree mixing of hepatic with IVC blood flow at the cranial level than at the caudal level in the Fontan tunnel. Although it was a relatively small difference, the HFD was significantly different between the novel and conventional HFD quantification approaches. Interestingly, when considering individual patients, differences between the novel and conventional HFD quantification as high as 14.9% were found.

HFD is a crucial hemodynamic parameter that is used by clinicians in their evaluation of Fontan performance. Hepatic blood flow contains hepatic factors, which are very important for a well-development of the lungs. A lack of hepatic factors in one of the lungs is associated with PAVMs formation[14,15]. Therefore, a balanced HFD towards both lungs is crucial. Moreover, an unbalanced HFD may suggest the need for intervention in an effort to restore a more balanced HFD, resulting in a reduced risk for PAVMs formation[88]. Consequently, an accurate HFD quantification is essential since it could have a clinical impact on Fontan patients. Current CFD studies used the conventional HFD quantification approach in which 'hepatic blood flow' particles are uniformly seeded from either a caudal or cranial cross-section in the Fontan tunnel[18–21]. Thereafter, the HFD is computed by counting the particles that leave the right pulmonary artery and left pulmonary artery. This conventional method relies on the assumption that hepatic blood flow is uniformly distributed over the Fontan tunnel blood flow. However, the correctness of this conventional HFD quantification method has never been investigated. In part A1 of this graduation project, we investigated the assumption of uniform distribution of hepatic blood flow in the Fontan tunnel and concluded that this assumption is not valid[18–21], at least in CFD models with only cardiac-dependent boundary conditions. There was a significantly better mixing of hepatic blood and IVC blood flow at the cranial level than at caudal level, but the hepatic blood flow was still not uniformly mixed over the Fontan tunnel. This non-uniform mixing of hepatic blood flow is explained by the bloodstream's laminar behavior with only minimal periodic flow amplitude changes along the cardiac cycle, leading to less optimal mixing.

Because of the uneven distribution of hepatic blood flow in the Fontan tunnel, the conventional HFD quantification approach could potentially provide inaccurate results. This project revealed that the novel approach had statistically different HFD outcomes than the conventional approach when using CFD models that only considered cardiac effects on blood flow; however, these differences were relatively small and on a cohort level of minimal clinical relevance. For this reason, the fact that there is a non-uniform distribution of hepatic blood flow in the Fontan tunnel does, in general terms, not affect the HFD quantification with clinical significance. Therefore, the findings of previously performed studies on group-level are still valid[18–21].

Even though the conventional HFD quantification method on group-level is accurate enough, it should be emphasized that on individual basis differences as high as 14.9% were found in patients. In that specific case, the HFD towards the left lung was 20.7% and 35.6% with the respective HFD quantification methods: $HFD_{cranial\ tunnel}$ and HFD_{HV}. Nowadays, clinicians accept an HFD of 70/30% between both lungs before they consider to intervene[19,89,90]. As one can see, the conventional HFD quantification method would indicate inadequate HFD, whereas the novel method reveals sufficient HFD for this specific case. These HFD differences may have implications for the patient-specific decision making about the need for intervention and therefore, could have a meaningful clinical impact on individual patients.

We believe that the novel HFD quantification better represents the physiology of hepatic blood flow in Fontan patients because 'hepatic' particles are actually seeded from the inlets of the hepatic veins instead of from a cross-section within the Fontan tunnel. However, more research with a larger cohort group is needed to investigate which Fontan patients profit the most from the novel HFD quantification method.

Limitations

Because hepatic veins are too small for (free-breathing ECG-gated 2D-3dir) PC-MRI acquisitions, we indirectly measured the total hepatic blood flow by subtracting the IVC flow (below the entrance of the hepatic veins) from the Fontan tunnel flow. Additionally, we assumed that the total hepatic blood flow was distributed over the different hepatic veins based on the ratio of their respective cross-sectional areas. Furthermore, we used free-breathing ECG-gated 2D-3dir PC-MRI data to reconstruct the boundary conditions; however, it ignores the respiratory effects on the blood flow waveforms. In my literature study, it was shown that the hepatic blood flow is 3 to 4 times higher during inspiration than expiration[24] while this effect was less pronounced in the IVC flow. Therefore, breathing could affect the pattern of the hepatic blood flow streams and hence the HFD quantification. Fortunately, we will reexamine the assessment of mixing between hepatic and IVC blood flow in the Fontan tunnel and the HFD quantification while incorporating the respiratory effects in part B2. Furthermore, we assumed a rigid vessel wall in the CFD models. Nevertheless, a previously performed study showed that wall compliance barely affects the time-averaged HFD[86]. Besides, a relatively coarse mixing evaluation was conducted by subdividing the entire cross-sections at the cranial and caudal levels into only four sections. Unfortunately, we did not consider the degree of mixing on smaller scales. Additionally, most Fontan patients included in this study had an ECC-type Fontan tunnel. Although the ECC and ILT-type Fontan tunnel are both TCPC connections, little different flow patterns may exist within the ITL-type tunnel compared to the ECC-type tunnel. Nevertheless, all these limitations should not affect our novel insights into the fluid dynamics of hepatic and IVC flow in a Fontan circulation and its impact on HFD quantification.

Conclusion

In brief, the hepatic blood flow is non-uniformly distributed within the Fontan tunnel, which was most noticeable in the caudal cross-section (just above the junction of the hepatic veins with the IVC). A significant difference was found in HFD between the conventional method, in which hepatic blood flow particles are uniformly seeded from either a caudal or cranial cross-section, and the novel method, in which particles are directly seeded from the level of the hepatic veins. However, although significant, these differences were relatively small and had no clinical relevance on-group level. Nevertheless, it should be emphasized that on individual basis differences as high as 14.9% were found in patients, which could influence the patient-specific decision making about the need for intervention.

Part B1.

The effects of respiration on the blood flow in the inferior vena cava, the Fontan tunnel, hepatic veins and superior vena cava using real-time PC-MRI

Introduction

Previously performed studies showed that the respiration influences the venous blood in the Fontan circulation. The venous blood flow in the IVC above the level of the hepatic veins in Fontan patients were more influenced by respiration compared to healthy subjects[23,24]. Hsia et al. and Fogel et al. stated that the Fontan tunnel flow was for 30% dependent on inspiration[24,25]. Also, the hepatic blood flow have been shown to be dependent on the respiration. Hsia and colleagues revealed that the hepatic blood flow was for 55% dependent on inspiration[24]. These percentages represent the blood flow that was solely derived from inspiration. Furthermore, the (invasive) Doppler Ultrasound studies showed that the hepatic blood flow in Fontan patients was between 3 to 4 times higher during inspiration than expiration[23–27,29–41].

Unfortunately, current clinical imaging studies have only investigated the respiratory effects on hepatic blood flow using (invasive) Doppler ultrasound[24,30,31,34–36,47,48] because the the resolution of real-time PC-MRI is not yet good enough for hepatic flow quantification. Real-time PC-MRI acquisitions take both cardiac and respiratory effects on blood flow waveforms into account, as described in chapter 2. Although Doppler Ultrasound has an excellent spatial resolution of 0.15-0.6 mm, which is higher than real-time PC-MRI[91], Doppler Ultrasound has also some disadvantages. First of all, the blood flow velocity measurement by Doppler ultrasound is affected by the beam angle and a small acoustic window. Therefore, the quality of the Doppler ultrasound examinations is highly dependent on the expertise of the operator[44,45]. Consequently, there is an observer dependency and low inter-observer reproducibility when using Doppler ultrasound. Furthermore, Doppler ultrasound is not always applicable in every region throughout the human body[60]. Moreover, assumptions about basic flow profiles and cross-sectional vessel areas need to be made to calculate mean velocities and net flow rates. These assumptions may produce imprecise flow measurements in the presence of complicated vessel geometry or flow[46]. Therefore, real-time PC-MRI measurements of the hepatic blood flow would be very desirable, also because real-time PC-MRI allows to investigate the respiratory effects on blood flow. In order to meet this desire, in this master thesis, we introduced a novel approach to indirectly measure the hepatic flow in the hepatic veins during the respiratory cycle using real-time PC-MRI. First, we measured the blood flow in the Fontan tunnel, just above the entrance of the hepatic veins. Second, we derived the IVC blood flow caudal from the hepatic veins. By subtracting these mean flows, we indirectly quantified the mean hepatic blood flow. This is the first work that used real-time PC-MRI for indirect quantification of hepatic flow to the best of our knowledge. With this new method, we were able to investigate the respiratory effects on the blood flow of the SVC, IVC, Fontan tunnel and the hepatic veins while using real-time PC-MRI. For the sake of clarity, in part B1 we only conducted an in-depth flow analysis without the use of CFD. We hypothesized that it was feasible to indirectly quantify hepatic blood flow in Fontan patients while using real-time PC-MRI. Furthermore, it was assumed that respiration has a pronounced impact on the hepatic veins and Fontan tunnel's flow rates while having mild effects on IVC and SVC flow in the Fontan patients at rest

In addition to the effects of respiration on blood flow rate, we were also interested in the impact of respiration on the blood flow velocity in the IVC and Fontan tunnel. Moreover, the velocity values were used to calculate the IVC-Tunnel mismatch parameter. The IVC-tunnel mismatch parameter was introduced by Rijnberg et al. and defined as an increase of

mean velocity from the IVC towards the Fontan tunnel[92]. The relative difference between the mean velocity in the IVC and Fontan tunnel characterizes the difference in size of these two geometries. Although the IVC-tunnel mismatch was highly correlated with energy loss known to be associated with exercise intolerance and related more inferior clinical outcomes[93], not much research has been dedicated to study the IVC-tunnel mismatch. Unfortunately, Rijnberg et al. did not make the distinction between inspiratory and expiratory flow data, and therefore they could not investigate the impact of respiration on the IVC-tunnel mismatch parameter. To bridge this knowledge gap, in this current chapter of my master thesis the research is described that was conducted to investigate the influence of respiration on the IVC-tunnel mismatch.
It was hypothesized that the IVC-mismatch value is influenced by respiration.

Methods

Study group

Three patients were studied with a TCPC (Fontan) tunnel. These three patients were the same subjects whose CFD simulation outcomes were pointed out in part A1. Patient characteristics are demonstrated in table 7 in part A1 (page 64).

Real-time PC-MR imaging and respiratory monitoring

Patients were investigated during rest and were placed in a supine position in the MRI scanner. Free-breathing non-ECG gated, non- navigator gated 2D PC-MRI (i.e., real-time PC-MRI) slices perpendicular to IVC, Fontan tunnel and SVC were used to acquire through-plane velocity profiles. During velocity segmentation, the velocities over the vessel's segmented area were integrated over the area to compute time-varying blood vessel flow rates (figure 32A).
In other words, when the cross-sectional areas of the vessels are determined using computer aided segmentation, time-varying volumetric flow rate data can be acquired from the velocity data by the following formula $Q = A \cdot v$ with Q= flow rate [m^3/s], A= area [m^2], v= velocity [m/s]. As stated before, the resolution of real-time PC-MRI is not yet good enough for hepatic flow quantification. Therefore, we introduced a novel approach to indirectly measure the hepatic flow in the hepatic veins during the respiratory cycle using real-time PC-MRI. First, we measured the blood flow in the Fontan tunnel, just above the entrance of the hepatic veins. Second, we derived the IVC blood flow caudal from the hepatic veins. By subtracting these mean flows, we indirectly quantified the mean hepatic blood flow. Every quantification consisted of 250 consecutive, real-time PC-MRI flow acquisitions over a 16.7 seconds time period. The real-time PC-MRI acquisitions details are shown in table 1 (page 32). Real-time PC-MRI are real-time flow measurements in which no gating is applied for respiration or cardiac contraction. Therefore, the obtained time-varying flow rate waveform of each vessel could start at any point in the cardiac cycle or respiratory cycle. Since we know from the literature that the respiration is primarily responsible for periodic changes in the flow amplitude in Fontan patients, we decided to monitor the respiratory cycle simultaneously with the real-time PC-MRI acquisitions (figure 32B). We used an abdominal placed respiratory belt to monitor the respiratory waveform that measured the expansion of the abdomen related to respiration. In the next paragraph we explain how the patient's respiratory curve is linked to the simultaneously acquired blood flow measurements. This coupling step was important since we

aimed at evaluating the flow during inspiration, expiration, and throughout the entire respiratory cycle.

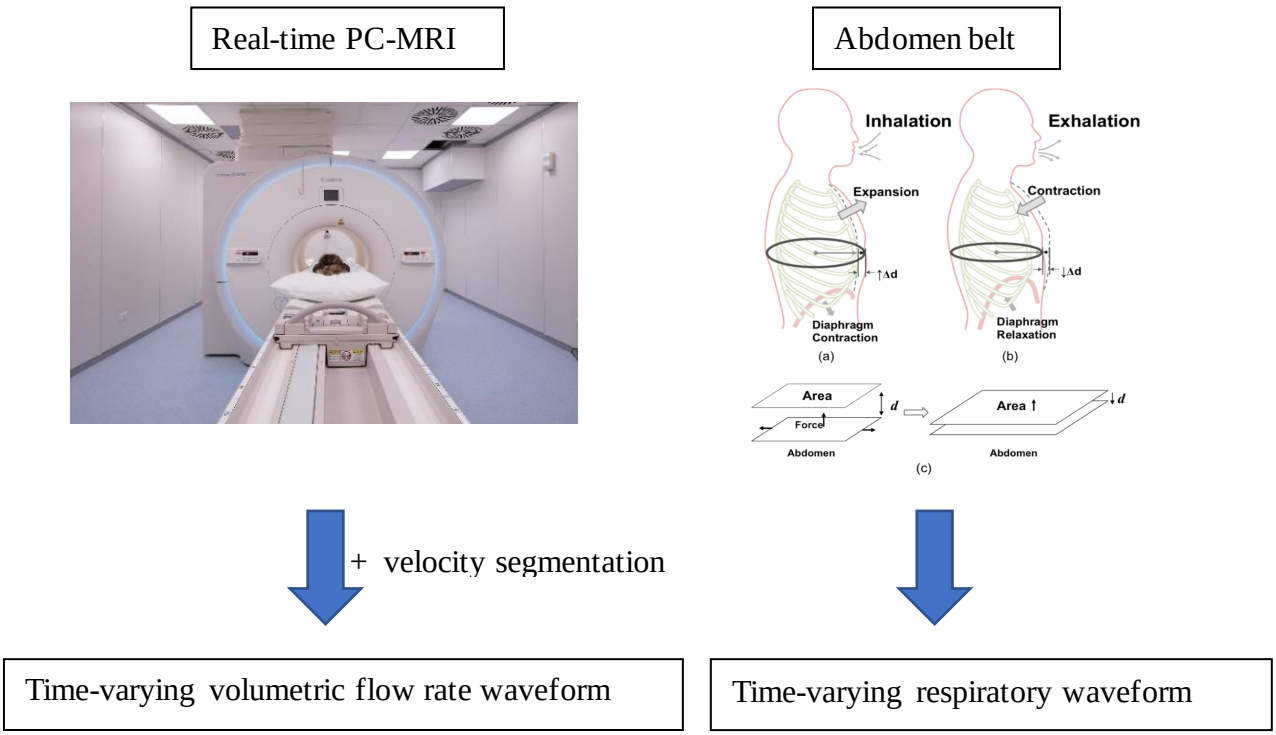

Figure 32: A. Real-time PC-MRI acquisitions that generate time-varying flow rate waveforms of each vessel after velocity segmentation, B: Abdomen belt that monitor the patient's respiratory waveform

Extracting the monitored respiratory waveform

Information about the respiratory cycle obtained from the abdominal placed respiratory belt was stored in so-called Philips Physlog files. The Physlog file also contains other information for instance from the MRI scanner showing markers that identify the different moments when the MRI scanner starts certain measurements. The first step was to extract the respiratory waveform that was synchronous with the real-time PC-MRI blood flow acquisitions. The beginning and end of the real-time PC-MRI acquisitions were marked by a signal of 100 and 20 units, respectively (Supplemental B, figure 53). Unfortunately, these start and stop markers were not accurate enough to extract the patient's respiratory waveform, since the time period between these markers did not completely match the time of the PC-MRI flow acquisition, which time is equal to the MRI gradient signal (Supplemental B, figures 54, 55, 56). Luckily, the MRI gradient signal that is used for the PC-MRI measurement was also stored as a signal in the Physlog file during that measurement . Therefore, we created a MATLAB code that first identified the start marker (equal to 100) and the stop marker (equal to 20). Hereafter, the code searched for the beginning and ending of the MRI gradient within the index range of the start and stop marker. The final step was to use the indices of the beginning and end of the MRI gradient signal to extract the patient's respiratory waveform (figure 33). In this way, we obtained the patient's respiratory waveforms of each vessel (IVC, SVC, Fontan tunnel) during their corresponding real-time PC-MRI acquisitions (figure 34).

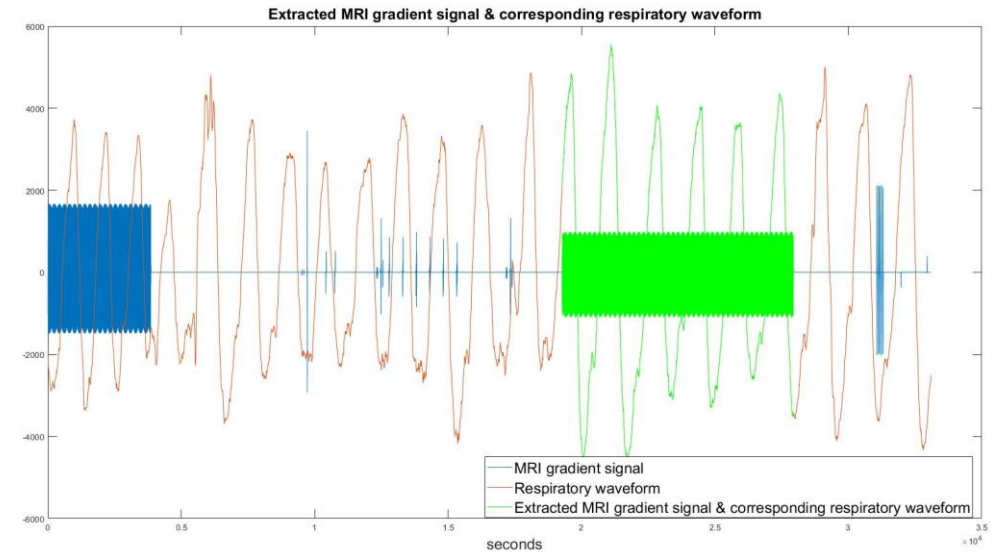

Figure 33: Extracted MRI gradient signal and corresponding respiratory waveform

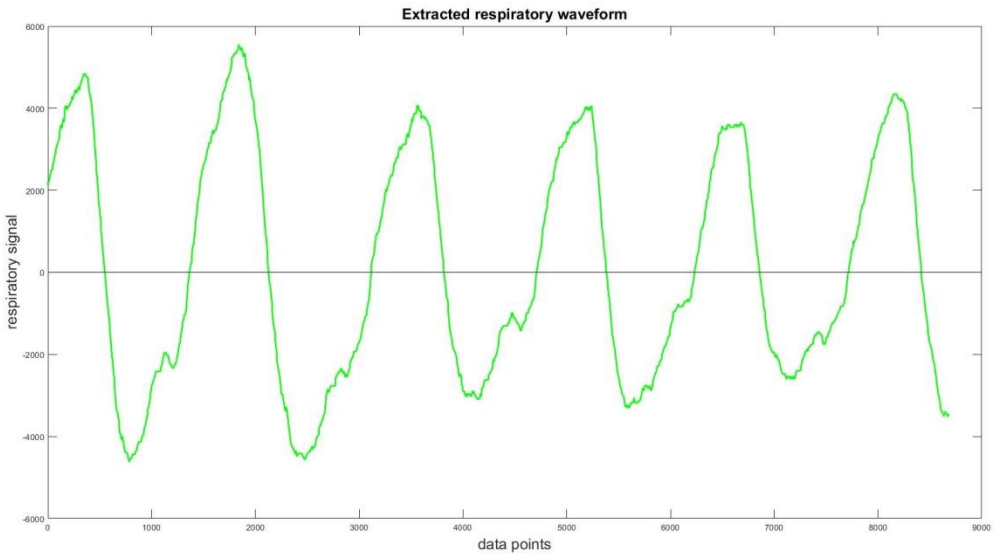

Figure 34: Extracted respiratory waveform

Defining the inspiratory and expiratory phases on the extracted respiratory waveform

The PHILIPS Physlog files manual describes the start of the upward deflection of the respiratory waveform is the starting point of the inspiratory phase and the beginning of the downward deflection is the starting point of the expiratory phase of the respiratory cycle. According to the Philips manual, the light blue line that shows the upward deflection represents the inspiratory phase, while the green line illustrates the expiratory phase (figure 35). Using this definition, the time ratio of the inspiratory to expiratory phase was 2.255 in this case, meaning that the inspiration is more than twice as long as the expiration. In normal breathing, the expiration time is around twice as long as the inspiration time, so the inspiratory-to-expiratory time ratio is usually around 0.5. Therefore, we checked the definitions of inspiration and expiration based on the belt in much more detail.

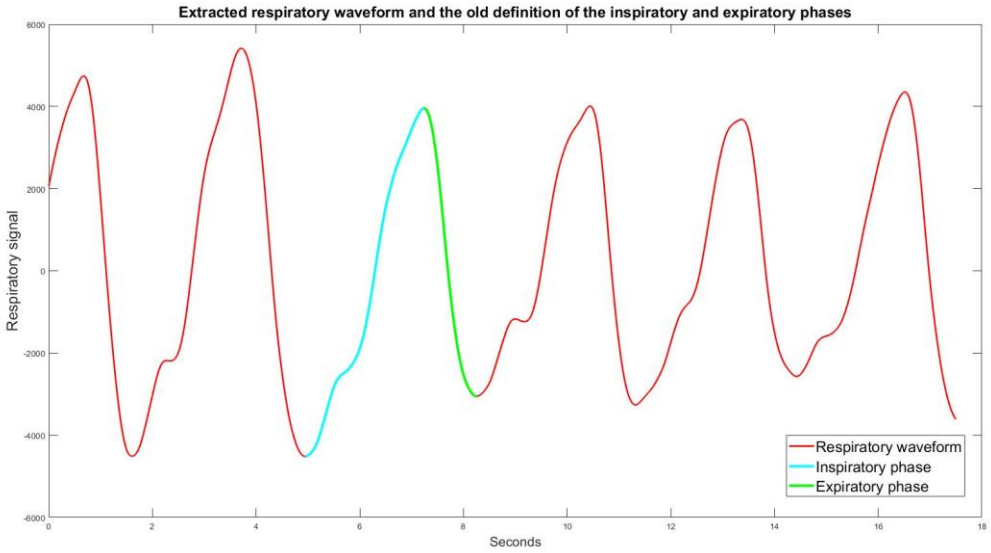

Figure 35: Extracted respiratory waveform and <u>the old definition</u> of the inspiratory and expiratory phases according to the Philips manual

In close collaboration with Utrecht UMC, we found out that some MRI scanners demonstrate a slowly increasing drift during the expiratory phase. Taking this information into consideration, the expiration is now defined as the range between the start of the downward deflection (i.e., curve's maximum) until the end of the drift (figure 36). The corrected definition provided normal inspiration to expiration time ratios. Moreover, additionally we checked this definition by scanning one person of our research team and monitored his respiratory waveform during normal breathing and breath-holding after expiration and concluded that expiration indeed cause a drift period in the respiratory signal (Supplimental B, figures 57 and 58).

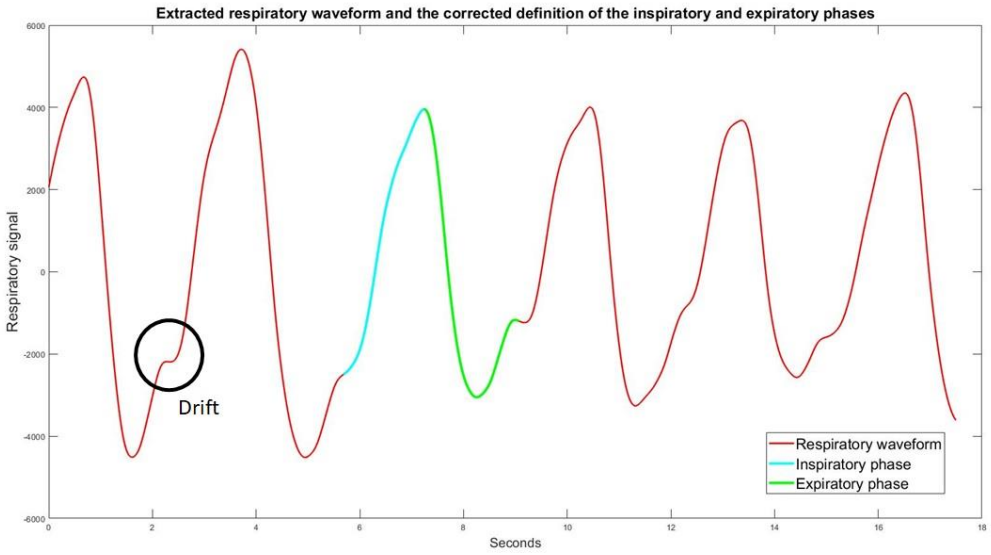

Figure 36: Extracted respiratory waveform and the corrected definition of the inspiratory and expiratory phases

We created a MATLAB code that automatically identified the start and end points of the inspiratory and expiratory phases of the various respiratory cycles on the respiratory waveform (see supplement C). Moreover this script can also be used to differentiate the multiple respiratory cycles from each other. Below you can see an example of respiratory waveform and its differentiation of four respiratory cycles (figure 37).

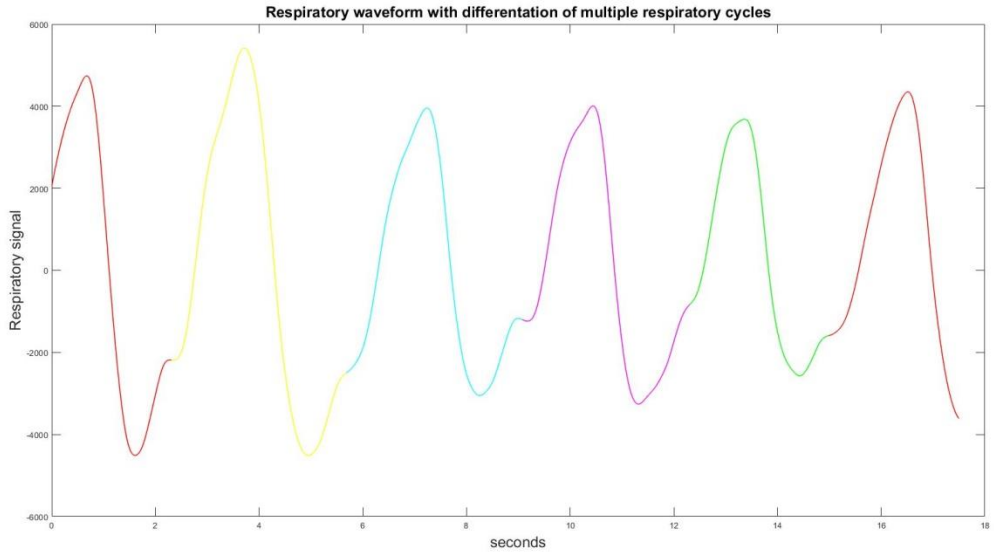

Figure 37: Respiratory waveform with differentiation of four respiratory cycles

Coupling of the respiratory waveform to the simultaneously obtained volumetric flow rate waveform

The next step was to couple the respiratory waveform to the simultaneously obtained volumetric flow rate waveform using MATLAB. Since the respiratory waveform (n=8000) was generated with a much higher temporal resolution than the volumetric flow rate waveform (n=250), the volumetric flow rate waveform was interpolate, such to obtain flow information at each moment of the respiratory waveform. We knew that the respiratory and volumetric flow rate waveforms had the same length of time and therefore we could interpolate the volumetric flow rate curve based on the number of measure points (i.e., indices) of the respiratory waveform using the Pchip function of MATLAB (The MathWorks, Inc., Natick, MA). The Pchip function is a shape-preserving' piecewise cubic Hermite polynomial method. Interpolation was an essential step for determining the inspiratory and expiratory flow since the indices of the respiratory waveform that marked the inspiratory and expiratory phases were translated to the volumetric flow rate waveform. Figure 38 demonstrates the interpolated volumetric flow rate and the corresponding respiratory waveform. The flow during inspiration is blue, whereas the flow during expiration is green. We have generated these interpolated volumetric flow rate waveforms for the IVC, SVC, and Fontan tunnel for all three Fontan cases. The inspiratory and expiratory flow values were used to analyze the effects of respiration on blood flow, as described in the next paragraph 'Flow calculations'.

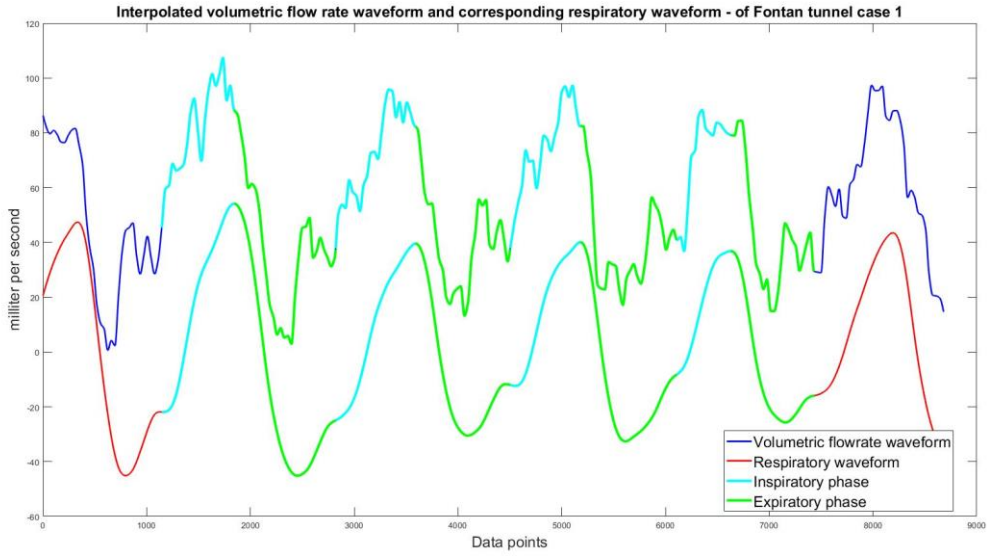

Figure 38: Interpolated volumetric flow rate waveform and corresponding respiratory waveform. The light blue colors marks the inspiratory phase and the inspiratory flow. The green color represents the expiratory phase and the expiratory flow

Flow calculations

The following flow parameters were calculated in each individual: We evaluated the flow during inspiration, expiration, and throughout the entire respiratory cycle for the IVC, SVC, and Fontan tunnel. The time-averaged flow rate from 2 to 4 inspiratory and from 2 to 4 expiratory phases, respectively, was calculated, as well as the overall average flow for each vessel. The number of inspiratory and expiratory phases relied on the maximum number of respiratory cycles available on the extracted respiratory waveform, which could vary between patients. The mean inspiratory, expiratory flow and mean flow throughout the entire respiratory cycle in the hepatic veins was indirectly quantified by subtracting the mean flow rates of the IVC (below the hepatic veins junction) from the mean flow rates of the Fontan tunnel (above the entrance of the hepatic veins). Furthermore, we analyzed a few specific respiratory-related flow parameters used in literature to reflect respiration effects. We decided to quantify all these different respiratory-related flow parameters so that these could be compared with literature. Hjortdal et al.[39,94] calculated the inspiratory flow fraction, which is the mean inspiratory flow in relation to mean flow rate during a complete respiratory cycle as follows[39,94]:

$$Inspiratory\ flow\ fraction = \frac{Q_{inspiration}}{Q_{full}} \quad (B1.1)$$

Where $Q_{inspiration}$ is the mean inspiratory flow rate [ml/s], Q_{full} is the mean flow rate during the entire respiratory cycle [ml/s].

We also evaluated the inspiratory-to-expiratory flow ratio, which was the mean inspiratory flow divided by the mean expiratory flow [24,27,34,36]:

$$Inspiratory\ to\ expiratory\ flow\ ratio = \frac{Q_{inspiration}}{Q_{expiration}} \quad (B1.2)$$

Where $Q_{expiration}$ is the mean expiratory flow rate [ml/s].

Besides, in reference to Hsia et al. we evaluated the flow that was solely dependent on inspiration[24]:

$$Percentage\ of\ inspiratory\ dependent\ flow = \frac{Q_{inspiration} - Q_{expiration}}{Q_{inspiration} + Q_{expiration}} * 100\% \ (B1.3)$$

Additionally, we performed an extra sub-analysis on the hepatic blood flow. We analyzed the mean inspiratory hepatic flow relative to the mean inspiratory Fontan tunnel flow, the mean expiratory hepatic flow relative to the mean inspiratory Fontan tunnel flow and the mean hepatic flow to the mean Fontan tunnel flow during the entire respiratory cycle:

$$mean\ inspiratory\ hepatic\ to\ tunnel\ flow = \frac{Q_{inspiration_{hepatic}}}{Q_{inspiration_{tunnel}}} \quad (B1.4)$$

$$mean\ expiratory\ hepatic\ to\ tunnel\ flow = \frac{Q_{expiration_{hepatic}}}{Q_{expiration_{tunnel}}} \quad (B1.5)$$

$$mean\ hepatic\ to\ tunnel\ flow\ full\ respiratory\ cycle = \frac{Q_{full_{hepatic}}}{Q_{full_{tunnel}}} \qquad (B1.6)$$

These specific hepatic relative to Fontan tunnel flow parameters gave insight into the hepatic blood flow's contribution to the tunnel flow during each respiratory phase. Finally, we also validated the inspiration time relative to the time of the entire respiratory cycle, which was called the inspiratory time fraction. The mean inspiratory time fraction was only achieved for the IVC, SVC and Fontan Tunnel since these vessels had a coupled respiratory waveform and hence a time vector:

$$Inspiratory\ time\ fraction = \frac{Mean\ time\ inspiration}{Mean\ time\ full\ respiratory\ cycle} \qquad (B1.7)$$

Coupling of the respiratory waveform to the simultaneously obtained velocity waveform and the IVC-Tunnel mismatch calculation

For quantifying the IVC-tunnel mismatch parameter, we had to perform all previously described steps, except that we had to interpolate the velocity waveform instead of the volumetric flow rate waveform (figure 39). Since the velocity waveform had the same temporal resolution as the volumetric flow rate waveform and therefore also contained 250 measure points over the same time period, we could use similar interpolations steps to couple the respiratory waveform to the velocity waveform, as described above. We evaluated the velocity during inspiration, expiration, and the entire respiratory cycle for the IVC (below the hepatic veins' entrance) and Fontan tunnel (above the junction of the hepatic veins). The mean velocity from 2 to 4 inspiratory and from 2 to 4 expiratory phases, respectively, was calculated, as well as overall mean velocity. The IVC-tunnel mismatch parameters as defined by Rijnberg et al during the inspiratory and expiratory phase and the complete respiratory cycle were calculated as follows[92]:

$$Mismatch_{IVC-tunnel} = \frac{V_{tunnel} - V_{IVC}}{V_{IVC}} * 100\% \qquad (B1.8)$$

Where:

$V_{tunnel} = mean\ velocity\ in\ a\ cross\ section\ in\ the\ Fontan\ tunnel\ \left[\frac{cm}{s}\right]$

$V_{IVC} = mean\ velocity\ in\ the\ IVC\ \left[\frac{cm}{s}\right]$

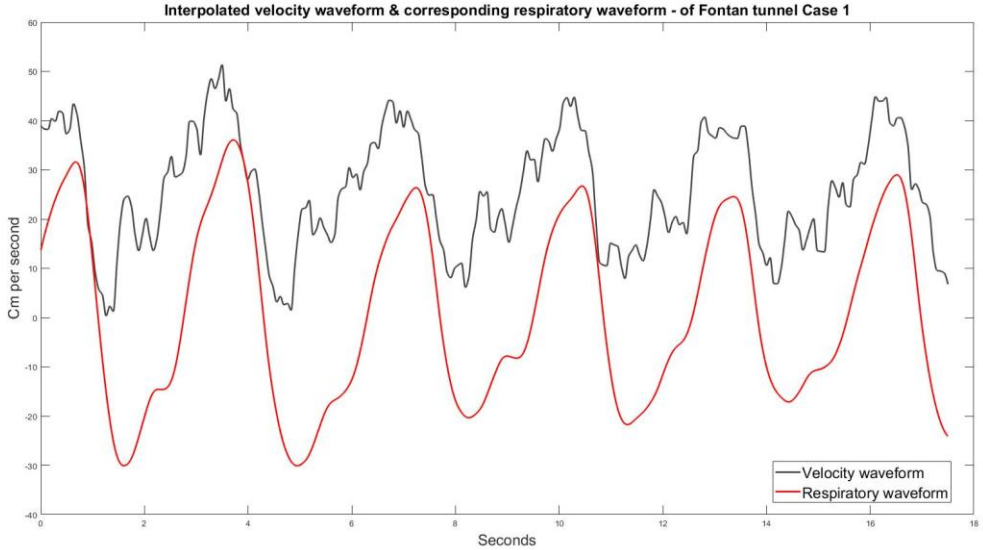

Figure 39: Interpolated velocity waveform and corresponding respiratory waveform

Results

Flow calculations

Tables 10,11 and 12 demonstrate the mean flow rates during inspiration, expiration and throughout the entire respiratory cycle, the inspiratory flow fraction, the inspiratory-to-expiratory flow ratio, percentage of inspiratory dependent flow and the inspiratory time fraction for the three studied cases. The flow was consistently higher during the inspiratory phase than during the expiratory phase for all blood vessels in each of the three cases. However, the most substantial inspiratory augmentation of flow was found in the Fontan tunnel and hepatic veins. The inspiratory-to-expiratory flow ratios showed that the Fontan tunnel flow was between 1.82 and 1.97 times higher during inspiration than during expiration. Furthermore, the Fontan tunnel flow was for 29.2% up to 32.7% dependent on inspiration. Regarding the hepatic flow, we observed that the hepatic flow in Fontan patients was dominated by inspiration. The inspiratory-to-expiratory flow ratios revealed that the hepatic flow increased 3.53 to 4.88 times during the inspiratory phase. Moreover, between 56.0% and 66.0% of the hepatic blood flow was dependent on inspiration. Besides the hepatic flow provides a dramatic contribution, varying between 46.0 and 63.0 percent, to the Fontan tunnel flow during inspiration (table 13). Contrary, the hepatic blood flow contribution to tunnel flow was between 19 and 32 % during expiration.

The IVC flow was minimally affected by inspiration with percentages of inspiratory dependent flow varying between 0.1% and 13.1%. However, the percentages of the SVC's inspiratory dependent flow differed a little bit more, namely between 5.8% and 27.0%, as well as the inspiratory-to-expiratory flow ratios, ranging from 1.12 and 1.74.

Table 10: Mean Blood Flow Rates (milliliter per second) in two to four respiratory cycles and corresponding mean flow rates in the inspiratory and expiratory phases in the IVC, Fontan tunnel, Hepatic veins and SVC for case 1. Besides, the inspiratory flow fraction [-], Inspiratory-to-expiratory flow ratio [-], percentage of inspiratory dependent flow [%] and inspiratory time fraction [-] are presented.

CASE 1	**IVC**	**Fontan tunnel**	**Hepatic veins**	**SVC**
Mean flow in respiratory cycle [ml/s]	30.28	55.10	24.82	28.45
Mean flow in inspiration [ml/s]	32.53	75.35	42.82	33.25
Mean flow in expiration [m/s]	28.22	40.34	12.12	24.49
Inspiratory flow fraction [-]	1.07	1.37	1.73	1.17
Inspiratory-to-expiratory flow ratio [-]	1.15	1.87	3.53	1.36
Percentage of inspiratory dependent flow [%]	7.1%	30.3 %	56.0%	15.2%
Inspiratory time fraction[-]	0.48	0.42	Not applicable	0.45

Table 11: Mean Blood Flow Rates (milliliter per second) in two to four respiratory cycles and corresponding mean flow rates in the inspiratory and expiratory phases in the IVC, Fontan tunnel, Hepatic veins and SVC for case 2. Besides, the inspiratory flow fraction [-], Inspiratory-to-expiratory flow ratio [-], percentage of inspiratory dependent flow [%] and inspiratory time fraction [-] are presented

CASE 2	IVC	Fontan tunnel	Hepatic veins	SVC
Mean flow in respiratory cycle [ml/s]	26.65	40.70	14.06	22.02
Mean flow in inspiration [ml/s]	32.04	59.83	27.79	36.34
Mean flow in expiration [ml/s]	24.62	30.32	5.70	20.88
Inspiratory flow fraction [-]	1.20	1.47	1.98	1.65
Inspiratory-to-expiratory flow ratio[-]	1.30	1.97	4.88	1.74
Percentage of inspiratory dependent flow [%]	13.1%	32.7%	66.0%	27.0%
Inspiratory time fraction [-]	0.28	0.36	Not applicable	Not reliable

Tabel 12: Mean Blood Flow Rates (milliliter per second) in two to four respiratory cycles and corresponding mean flow rates in the inspiratory and expiratory phases in the IVC, Fontan tunnel, Hepatic veins and SVC for case 3. Besides, the inspiratory flow fraction [-], Inspiratory-to-expiratory flow ratio [-], percentage of inspiratory dependent flow [%] and inspiratory time fraction [-] are presented

CASE 3	IVC	Fontan tunnel	Hepatic veins	SVC
Mean flow in respiratory cycle [ml/s]	32.40	62.90	30.50	13.41
Mean flow in inspiration [ml/s]	32.33	87.03	54.70	14.27
Mean flow in expiration [ml/s]	32.40	47.72	15.32	12.71
Inspiratory flow fraction [-]	1.0	1.38	1.79	1.06
Inspiratory-to-expiratory flow ratio [-]	1.0	1.82	3.57	1.12
Percentage of inspiratory dependent flow [%]	0.1%	29.2%	56.2%	5.8%
Inspiratory time fraction [-]	0.39	0.38	Not applicable	0.45

Table 13: Mean inspiratory hepatic to tunnel flow ratio [-], mean expiratory hepatic to tunnel flow ratio [-], mean hepatic to tunnel flow ratio during the entire respiratory cycle [-]

	Mean inspiratory hepatic to tunnel flow ratio [-]	**Mean expiratory hepatic to tunnel flow ratio [-]**	**Mean hepatic to tunnel flow ratio during entire the respiratory cycle [-]**
CASE 1	0.57	0.30	0.45
CASE 2	0.46	0.19	0.35
CASE 3	0.63	0.32	0.49

Additionally, the inspiratory time fractions remained within normal ranges. The inspiratory time fraction of the SVC of case 2 was not reliable since the respiratory signal was not well obtained and there existed an extremely long period of drifting (figure 40). However, since we were primarily interested in the mean inspiratory and expiratory flow and not in time, we could still use our developed approach to obtain the mean flow values (figure 40) in consultation with the researcher of LUMC.

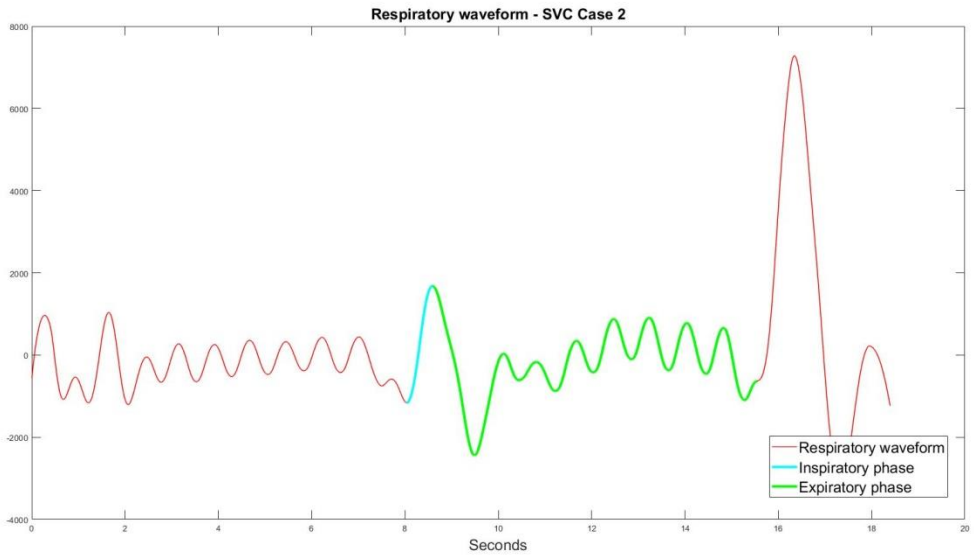

Figure 40: Respiratory waveform during SVC PC-MRI acquisitions of Case 2. In this respiratory signal, there was an extremely long period of drifting

IVC-tunnel mismatch calculations

The mean velocity of the IVC and Fontan tunnel for all three studied cases are presented in tables 14, 15, and 16. These tables also reveal the IVC- tunnel mismatch parameters during inspiration, expiration, and throughout the complete respiratory cycle. As can be seen, there was a huge IVC-tunnel mismatch during inspiration, varying between 80.5% and 291.0%. These mismatch values signify an increase of velocity between 80.5 and 291.0 percent from the IVC towards the Fontan tunnel during the inspiratory phase. During expiration, the IVC-tunnel mismatch parameters reduced extensively. Nevertheless, when considering the average IVC-tunnel mismatch parameters over the entire respiratory cycle, there still existed a serious IVC-tunnel mismatch for all three subjects, ranging from 55.1% to 188.2%. Furthermore, these observations confirmed the previous findings of a substantial inspiratory augmentation of flow within the Fontan tunnel, leading to a larger IVC-tunnel mismatch during inspiration than during expiration.

Table 14: Mean velocities [cm/s] in two to four respiratory cycles and corresponding mean velocities in the inspiratory and expiratory phases in the IVC and Fontan tunnel for case 1. Besides, the IVC-tunnel mismatch during inspiration, expiration and throughout the full respiratory cycle are presented.

CASE 1	**Fontan Tunnel**	**IVC**		**IVC- tunnel Mismatch**	
Mean velocity inspiration [cm/s]	35.14	14.81		**Inspiration [%]**	137.3%
Mean velocity expiration [cm/s]	18.78	13.21		**Expiration [%]**	42.2%
Mean velocity full respiratory cycle [cm/s]	25.69	14.00		**Full respiratory cycle [%]**	83.9%

Table 15: Mean velocities [cm/s] in two to four respiratory cycles and corresponding mean velocities in the inspiratory and expiratory phases in the IVC and Fontan tunnel for case 2. Besides, the IVC-tunnel mismatch during inspiration, expiration and throughout the full respiratory cycle are presented.

CASE 2	**Fontan Tunnel**	**IVC**		**IVC- tunnel Mismatch**	
Mean velocity inspiration [cm/s]	22.68	12.56		**Inspiration [%]**	80.5%
Mean velocity expiration [cm/s]	11.99	9.25		**Expiration [%]**	29.7%
Mean velocity full respiratory cycle [cm/s]	15.74	10.15		**Full respiratory cycle [%]**	55.1%

Table 16: Mean velocities [cm/s] in two to four respiratory cycles and corresponding mean velocities in the inspiratory and expiratory phases in the IVC and Fontan tunnel for case 3. Besides, the IVC-tunnel mismatch during inspiration, expiration and throughout the full respiratory cycle are presented.

CASE 3	Fontan Tunnel	IVC		IVC- tunnel Mismatch	
Mean velocity inspiration [cm/s]	41.81	10.69		**Inspiration [%]**	291.0%
Mean velocity expiration [cm/s]	24.13	10.76		**Expiration [%]**	124.3%
Mean velocity full respiratory cycle [cm/s]	30.96	10.74		**Full respiratory cycle [%]**	188.2%

Discussion

First of all, it is good to know that the term 'IVC flow' in literature can signify Fontan tunnel flow above the entrance of hepatic veins (because some researchers see the Fontan tunnel as an extension of the IVC) or IVC flow below the entrance of the hepatic veins. It is, therefore, necessary to relate the outcomes of this study with literature carefully.

Part B1 showed the flow was consistently higher during the inspiratory phase than during the expiratory period for all studied blood vessels for all three cases. These findings also confirmed that the flow in the hepatic veins and Fontan tunnel are heavily influenced by inspiration. The flow rates in the Fontan tunnel and hepatic increased dramatically during inspiration, and decreased during expiration. Moreover, inspiration seemed to be the main driving force behind hepatic blood flow in patients with a Fontan circulation. We found that hepatic blood flow was for 56.0 and 66.0 percent dependent on inspiration, which was in line with the Doppler Ultrasound measurements of Hsia et al., who found that 55% of the hepatic blood was dependent on inspiration[24]. Moreover, the percentages of inspiratory dependency of Fontan tunnel flow ranging from 29.2% to 32.7% were in close agreement with Fogel et al. and Hsia et al. that both found a 30% inspiratory dependency[24,25]. The obtained inspiratory-to-expiratory flow ratios of the Fontan tunnel and hepatic veins in our study were also consistent with the outcomes of previously performed clinical studies and fell within the standard deviation[24,27,32,34,36,41,95]. Although less pronounced, respiration also had a considerable effect on the SVC blood flow. The results of the SVC showed a more variable range than those of the IVC. The outcomes partially contradict Hjortdal's statement that SVC blood flow is not affected by respiration[23]. However, when you think about it, theoretically, the SVC is - just like the Fontan tunnel – directly connected to the pulmonary arteries of the lungs during the Glenn procedure. Therefore, we believe that the SVC's blood flow is also subjected to the intrathoracic pressure changes related to respiration, which explains why we did not found inspiratory flow fractions equal to 1. Wei et al. also concluded that respiratory effects impact the SVC flow and found an inspiratory-to-expiratory flow ratio of 1.9 ± 0.6[27]. In this current study, the SVC's inspiratory-to-expiratory flow ratios fell with the standard deviations described by Wei and colleagues. Regarding the IVC flow (measured below the entrance of the hepatic veins), we discovered that it was the least affected by respiration compared to the other studied blood

vessel, which phenomenon has previously been described by other researchers as well. The IVC's inspiratory flow fractions and inspiratory-to-expiratory ratios for all three cases were in line with the literature.

It is known from the literature that Fontan patients are more affected by respiration than healthy subjects[23,24]. The explanation is that Fontan patients do not have a sub-pulmonary ventricle that steadily pumps the blood into the lung. Moreover, during the Fontan procedure, the surgeons create a direct connection between the IVC and the lungs by the Fontan tunnel, which healthy subjects do not have. Therefore, Fontan patients are more affected by intrathoracic pressure changes related to respiration. Inspiration drops the intrathoracic pressure to negative values and is considered to be responsible for the increased inspiratory Fontan tunnel and hepatic blood flow. Conversely, the blood flow in the hepatic veins and Fontan tunnel are substantially decreased during expiration. Our findings are entirely in line with this theory; however, it does not clarify why Fontan tunnel flow and hepatic blood flow are more affected by respiration than the blood flow in the SVC and IVC. We try to provide an answer to this question below.

Firstly, the blood flow in the hepatic veins in healthy subjects is dependent on the compliance of the liver parenchyma, the cardiac cycle, right heart hemodynamics and the respiratory cycle[96]. It is hypothetically speaking, but due to the Fontan anatomy, it seems logical that the cardiac cycle and right heart hemodynamic factors become less pronounced, whereas the respiratory cycle impact on the hepatic blood flow increases. The findings of Hsia et al., who discovered that 55% of the hepatic blood flow in Fontan patients was dependent on inspiration and only 25% of the hepatic blood in healthy subjects was dependent on inspiration, support this idea[24]. Regarding the Fontan tunnel flow, it was quite interesting that we found that the contribution of the hepatic blood flow to the tunnel flow was tremendous, especially during inspiration. Because most of the hepatic flow occurs during inspiration, a large proportion of the Fontan tunnel flow is hepatic flow, and the fact that the Fontan tunnel is directly attached to the lungs, we believe this explains why the Fontan tunnel flow was highly influenced by respiration as well. Furthermore, the IVC below the entrance of the hepatic veins is not exposed to this significant contribution of respiratory-derived hepatic blood flow. Besides, the IVC is farther located from the lungs. Additionally, the IVC is a kind of collecting barrel, in which many veins from the lower part of the body drain their venous blood. Therefore, we believe the respiratory effects on the IVC blood flow are more averaged out. On the other hand, the SVC is nearby located and directly connected to the lungs. Nevertheless, the respiratory effects on the SVC blood flow were less noticeable than in the Fontan tunnel. Our outcomes showed that the flow split (SVC flow: Fontan tunnel flow) was between 17.5%-35.0%: 82.5%-65.0% among the three cases. So, the total amount of venous blood flow that reached the lungs contained mainly blood flow from the Fontan tunnel. Hjortdal et al. supported this finding[23]. The difference in respiratory flow variation between the SVC and Fontan tunnel is possibly related to a larger venous capacitance in the inferior part of the body that allows an accumulation of blood in the veins, especially the hepatic veins, of the lower part of the body, during expiratory phase and mobilization of this reservoir during inspiratory phase.

Besides, we have demonstrated that it is possible to use real-time PC-MRI for indirect hepatic flow examination in Fontan patients (by subtracting mean flow rates of the IVC from the mean flow rates of Fontan tunnel flow). The hepatic flow parameters of this approach were

consistent with other clinical studies that used Doppler ultrasound to evaluate the hepatic blood flow[24,34–36,41]. Therefore, we showed the feasibility of deriving hepatic flow from clinical routinely real-time PC-MRI acquisitions, which could be a new opportunity for evaluating the hepatic blood flow in Fontan patients. However, a drawback of using real-time PC-MRI to quantify hepatic blood flow is that a MATLAB programming code is needed to extract and analyze the respiratory waveform and its corresponding flow rate waveform for each vessel. The current MATLAB code that we generated is semi-automatic and still consists of a few manual checks. However, it is possible to professionally optimize the code to a software program that fully automatically evaluates the real-time PC-MRI data and its corresponding respiratory signal. Nevertheless, future research is needed to elucidate the potential of deriving hepatic blood flow from real-time PC-MRI on a clinically routine basis.

Additionally, regarding our third objective, the results confirmed our hypothesis that the IVC-tunnel mismatch increases during inspiration. This increased IVC-tunnel mismatch indicated a tremendous rise in velocity from the IVC towards the Fontan tunnel during the inspiratory phase. Although far less prominent, also during expiration, there still existed an IVC-tunnel mismatch in all three cases. These differences in velocity values within the transition zone from IVC to Fontan tunnel cannot be healthy from a fluid dynamic perspective since an IVC-tunnel mismatch is highly correlated with energy losses in the Fontan circulation and reduced exercise tolerance[92]. Unfortunately, previous studies did not distinguish between inspiratory and expiratory flow data, and therefore they could not investigate the impact of respiration on the IVC-tunnel mismatch parameter[92]. This study's strength is that we evaluated the IVC-tunnel mismatch parameter for three Fontan cases during inspiration, during expiration, and throughout the entire respiratory cycle. Although we did not investigate the energy loss due to the IVC-tunnel mismatch, we strongly believe, based on our findings, that respiratory effects should play an essential role in future IVC-tunnel mismatch and energy loss calculations.

Limitations

It is worth mentioning that the findings of part B1 are based on three Fontan patients. A larger group of Fontan patients is needed for being able to translate results into generalizable insights.

Furthermore, the troubles that we experienced with defining the inspiratory and expiratory phases on the respiratory waveform were not described in the PHILIPS Physlog manual. The definition of inspiration and expiration, according to this manual, was not correct. Although another research group discovered similar problems, the respiratory signal issues have not been thoroughly investigated before. We created a solution to extract the respiratory signal with a corrected definition of the inspiratory and expiratory phases. This corrected definition provided us physiologically plausible flow values and normal inspiration to expiration time ratios. Moreover, we validated our theory by monitoring the respiratory waveform of one of our researchers. However, we have not fully examined what triggers the drifts in the expiratory phase and if these troubles with the respiratory signal could be solved.

Additionally, all Fontan patients included in part B1 had an ECC-type Fontan tunnel. Although the ECC and ILT-type Fontan tunnel are both TCPC connections, little different flow patterns may exist within the ITL-type tunnel compared to the ECC-type tunnel.

Besides, it is known that the heart rate could vary with breathing, which is called respiratory sinus arrhythmia (RSA). Due to RSA, the heart rate increases during inspiration and reduces during expiration. RSA is a physiological phenomenon; however, RSA occurs mostly in young and healthy subjects[97]. Fontan patients are not categorized as healthy subjects, but it is theoretically possible that the inspiratory augmentation of flow was due to cardiorespiratory response instead of inspiration alone. Nevertheless, a few articles that studied the cardiac and respiratory effects on blood flow separately using real-time PC-MRI (sometimes in combination with CFD) has already demonstrated that respiration is primarily responsible for the flow pulsatility in the Fontan tunnel and hepatic veins in Fontan patients[24,26,27,29–31,34–37]. Furthermore, these studies also showed that the cardiac cycle barely affects the flow rate changes in Fontan circulations, which is quite logical since the Fontan tunnel bypasses the heart and is directly connected to the lungs.

Furthermore, Hsia et al. demonstrated that the venous blood flow in Fontan patients is significantly influenced by gravity, which is not considered in this study. We measured the flow rates of patients that were in supine positions during their PC-MRI acquisitions. However, Hsia et al. used Doppler Ultrasound to evaluate blood flow, whereas we used an MRI scanner. Therefore, it was not possible to obtain the flow acquisitions in an upright position.

Conclusion

Respiration tremendously affects the hepatic blood flow and the Fontan tunnel flow. The flow rates in the Fontan tunnel and hepatic increased dramatically during inspiration, then decreased during expiration. For instance, the hepatic blood was 3.53 to 4.88 times higher during inspiration than during expiration. Also, the blood flow in the SVC was considerably influenced by breathing. However, respiration had a minimal effect on the blood flow in the IVC. These findings were in close agreement with what has previously been described. Therefore we showed it was feasible to quantify hepatic blood flow and analyze the respiratory effects while using real-time PC-MRI. Although more research is needed, real-time PC-MRI could be a new opportunity for evaluating the hepatic blood flow in Fontan patients instead of using Doppler Ultrasound in the future. Besides, we showed that there was an increase in the IVC-tunnel mismatch during inspiration compared to expiration. This IVC-tunnel mismatch indicated a tremendous increase in velocity from the IVC towards the Fontan tunnel during the inspiratory phase. Although we did not investigate the energy loss due to the IVC-tunnel mismatch, we strongly believe, based on our findings, that respiratory effects should play an essential role in future IVC-tunnel mismatch and energy loss calculations.

Part B2.

The Influence of respiration on the assessment of mixing between hepatic and inferior vena cava blood flow & hepatic flow distribution quantification

Introduction

Respiration is a physiologic influence on Fontan hemodynamics that has unfortunately not been incorporated in most of the CFD models. However, previous clinical imaging studies and the outcomes of part B1 of this master thesis showed that respiration has a tremendous impact on the blood flow in the hepatic veins and Fontan tunnel in Fontan patients. The flow rates in the Fontan tunnel and hepatic increased dramatically during inspiration. Then the flow rates decreased during expiration[23–27,29–41]

The effects of respiration may have important implications for the CFD modeling outcomes, such as hepatic flow distribution (HFD). Tang and colleagues are one of the few who did investigate HFD using CFD models with boundary conditions that took both cardiac and respiratory effects on blood flow into account[22]. Tang et al. compared the HFD between CFD models with and without respiration and found no significant difference in HFD values between both models. They concluded that respiration did not significantly impact the HFD parameter[22]. However, also this study used the conventional HFD quantification method by tracking particles that were uniformly seeded from a cross-section within the Fontan tunnel and analyzing the distribution of these particles towards both lungs. As mentioned earlier, this approach assumed that hepatic blood flow is uniformly distributed in the Fontan tunnel. In part A1, we introduced a *novel HFD quantification method, in which 'hepatic' particles are directly seeded from the level of the inlets of the hepatic veins. Based on the outcomes of 15 CFD simulations that only considered the cardiac effects on blood flow,* we concluded in part A1 that hepatic blood flow was non-uniformly distributed within the Fontan tunnel. Furthermore, a significant difference was found between the novel and conventional HFD quantification methods. Despite the fact that part A1 already showed that there was a non-uniformly mixing between hepatic and IVC blood flow within the Fontan tunnel and a significant difference in HFD values between the novel and conventional HFD quantification methods, the respiratory effects on the blood flow were ignored in the CFD models of part A1. Therefore, in part B2, we wanted to re-examine the mixing assessment of hepatic with IVC blood flow within the Fontan tunnel and HFD values of part A1 using patient-specific CFD models that did consider the cardiac and the respiratory effects on blood flow. So, in part B2, we aimed to test the assessment of mixing between hepatic and IVC blood flow in the Fontan tunnel and the differences between the novel and conventional HFD quantification method again while taking respiration into account. Therefore, we used the same 3D geometrical Fontan models and meshes of three cases as used in part A1, except that part B2 used boundary conditions used that included both the cardiac and respiratory effects on blood flow. The first objectives of part B2 of the master thesis project were to 1. evaluate the degree of mixing of the hepatic blood with the IVC blood in the Fontan tunnel and 2.quantify HFD using particle tracing directly from the hepatic veins (the novel approach), and compare results with the conventional approach while using CFD models that consider both the cardiac and respiratory effects on blood flow. We hypothesized that there is also a non-uniformly distribution of hepatic blood in the Fontan tunnel when respiratory effects on blood flow are considered. Furthermore, we believed that the HFD values between the conventional and novel methods still vary a lot, similar to the CFD models that only considered cardiac effects (part A1).

In addition to separate analysis of the outcomes of the CFD simulations that consider both the cardiac and respiratory effects on blood flow, we also wanted to compare the degree

mixing between IVC and hepatic blood flow in the Fontan tunnel and HFD values between the CFD models with (part B2) and without respiration (part A1). This comparison made it possible to test the statement of Tang et al. that respiration not (significantly) affects the HFD. We hypothesized that including respiratory effects in the CFD simulations would provide a different degree of mixing between hepatic and IVC blood flow and different HFD values compared to the CFD models that ignore respiration, which would disapprove Tang et al.'s statement.

Aside from the different seeding locations (the novel versus conventional HFD quantification method), HFD can also be quantified with convection diffusion modeling (The Eulerian method), as stated before in chapter 2. The difference between the Lagrangian particle tracking and the Eulerian convection diffusion modeling method is more a technical issue from a computational efficiency perspective. The Lagrangian particle tracking method is the golden standard for HFD quantification in Fontan patients and widely used by other research groups. However, a pilot study by Prof. Dr. S. Kenjereš and his student D. Gaillard of the TU Delft, who are also members of the TOP-FLOW consortium, demonstrated that the Eulerian method might be an elegant alternative for HFD quantification instead of the Lagrangian method. The Eulerian method uses the concentration of particles and computes the overall convection and diffusion of a number of particles. Since we wanted to explore the efficiency of the Eulerian method, we compared the HFD values obtained from the Lagrangian and Eulerian method for one similar case in part B2. For both the Lagrangian and the Eulerian method, we used the inlet of the hepatic veins as the starting point for HFD quantification. So in the Lagrangian method, we used the novel HFD quantification method, in which particles were seeded directly from the level of the hepatic veins. For the Eulerian method, we needed to model the hepatic blood flow and the remaining blood flows as two separate mass flow rates. The hepatic blood mass flow rate was prescribed as boundary condition at the inlets of the hepatic veins. We hypothesized that the Lagrangian and Eulerian methods would give similar HFD results.

Besides, an additional analysis of part B2 was to investigate the amount of hepatic backflow during one respiratory cycle. Hsia et al. studied the hepatic backflow in healthy and Fontan subjects. The researchers explained that since the Fontan tunnel bypasses the heart, Fontan patients are excluded from the atrial systolic flow that provides physiological retrograde hepatic flow pattern[24]. They concluded that hepatic backflow in Fontan patients was mainly driven by respiration that occurred mainly during expiration[42]. To investigate respiration's role on the hepatic backflow in Fontan patients, part B2 analyzed the hepatic backflow during one respiratory cycle. Although this sub-analysis is purely a flow analysis without the use of CFD and therefore seems to fit better in part B1, we performed our hepatic backflow analysis on the average total hepatic volumetric flow rate waveform that was used as a boundary condition in the CFD models of part B2. Therefore, all the steps below also had to be undertaken until the CFD implementation to make it possible to study the amount of hepatic backflow throughout the respiratory cycle. For that reason, the sub-analysis of hepatic backflow is included in part B2. We hypothesized that hepatic backflow mainly occurs during expiration.

Methods

Study group

Three Fontan patients were studied with a TCPC (ECC-type) Fontan tunnel. These three patients were the same subjects whose CFD simulation outcomes were pointed out in part A1. Patient characteristics are demonstrated in table 7, page 64 in part A1.

CFD simulations

In part B2, we conducted unsteady CFD simulations with boundary conditions that consider both the respiratory and cardiac effects on blood flow in contrast to part A1, which CFD models only considered the cardiac effects on blood flow. Since we wanted to make a proper comparison between CFD models with and without respiration, we used the same 3D geometrical Fontan models that incorporated the hepatic veins in the computational fluid domain, meshes, material properties, convergence criteria and discretization schemes as used in the CFD models that only considered the cardiac effects on blood flow in part A1. More information on meshes, material properties and discretization schemes can be found in chapter 3. We only changed the boundary conditions and some simulation details in the CFD models of part B2 compared to the CFD models of part A1. Furthermore, we had to run an extra CFD simulation to implement the convection diffusion model (the Eulerian method).

Inlet boundary conditions

For the reconstruction of the inlet boundary conditions, we used free-breathing non-ECG gated non-navigator gated 2D PC-MRI, or real-time PC-MRI, slices perpendicular to IVC, Fontan tunnel, and SVC to acquire through-plane velocity profiles. During velocity segmentation, the velocity over the vessel's segmented area is integrated over the area to acquire volumetric flow rate waveforms. Real-time PC-MRI acquisitions take both cardiac and respiratory effects on blood flow waveforms into account. Since research revealed that respiration is primarily responsible for the flow pulsatility in the Fontan tunnel and hepatic veins, whereas the cardiac cycle barely influences the flow pulsatility in Fontan patients, we only corrected the phase-shifts of the respiratory cycle between the time-varying flow rate waveforms for every inlet vessel. As performed in part B1, the initial processing steps were also needed in part B2 for the reconstruction of the inlet boundary conditions. We took the extracted respiratory waveforms and their corresponding interpolated volumetric flow rate waveforms for every vessel from part B1, which served as the first step in creating the inlet boundary conditions in the CFD models of part B2. Figure 41 demonstrates an example of an interpolated volumetric flow rate wave and its corresponding respiratory waveform of the Fontan tunnel of case 1, as we obtained in part B1. As illustrated in figure 41, the extracted interpolated volumetric flow rate and respiratory waveform contain data of four respiratory cycles.

However, we only needed one average volumetric flow rate waveform of one average respiratory cycle of each vessel for the CFD simulations instead of four respiratory cycles' flow data. To obtain one average volumetric flow rate waveform of one average respiratory cycle for each vessel, we had to perform a second interpolation (apart from the interpolation between the volumetric flow rate and respiratory waveform as outlined in part B1). In the second interpolation, we interpolated the different respiratory cycles and its corresponding volumetric

flow rate waveforms on each other per vessel. To do this, we had to split the respiratory waveform and its corresponding volumetric flow rate curve into separate vectors related to one respiratory cycle and interpolate the different respiratory and corresponding flow rate waveforms on each other. Besides, we used the end-inspiration index for each respiratory cycle vector to correct for the phase-shifts between the individual vectors. The phase-shift correction between the different respiratory cycle vectors was necessary to ensure the inspiratory and expiratory phases of each of the different respiratory cycles had the same length of time. Interpolation was performed using the Pchip function of MATLAB. After the second interpolation and phase-shift correction step, we computed an average volumetric flow rate waveform of one average respiratory cycle for each vessel (figure 42). The red dashed line and the dark blue dashed line represent the average respiratory cycle and the average volumetric flow rate waveform, in this particular figure, for the Fontan tunnel of case 1. The arrows in figure 42 indicate the end of inspiration (and hence the start of expiration) of every respiratory cycle. As you can see, the duration of inspiration and expiration are made equal between the different respiratory curves and their corresponding volumetric flow rate waveforms due to the second interpolation and phase-shift correction step. Although the volumetric flow rate waveforms extracted from real-time PC-MRI also contain information about cardiac effects on flow rates, we decided not to correct for the phases of the cardiac cycle, as explained above.

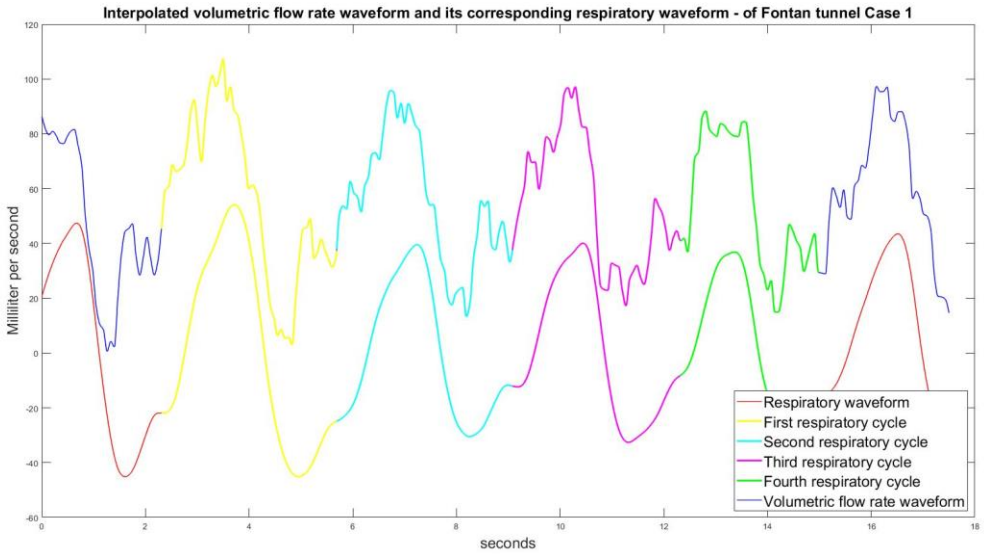

Figure 41: Interpolated volumetric flow rate waveform and its corresponding respiratory waveform (of the Fontan tunnel flow of case 1)

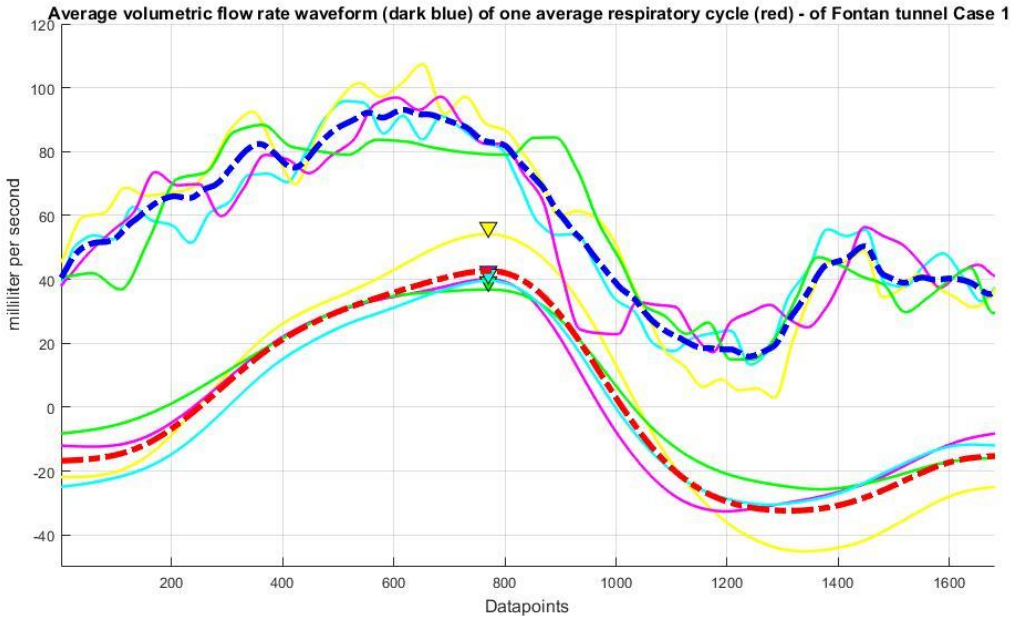

Figure 42: Average volumetric flow rate waveform (dark blue) of one average respiratory cycle (red) (of the Fontan tunnel flow of case 1). Note that the volumetric flow rate and respiratory curves in yellow, magenta, green and light blue are the same as in figure 41 above

We created such an average volumetric flow rate waveform of one average respiratory cycle for the following blood vessels: the IVC, SVC, and Fontan tunnel.

Hereafter, we needed a third interpolation and phase-shift step because the volumetric flow rate waveforms of the IVC, SVC and Fontan tunnel also needed to be interpolated and phase-shift corrected on each other. The reason for the third interpolation and phase-shift correction step is that it was necessary to implement inlet boundary conditions that were in phase to ensure the blood flow of every inlet boundary condition of the CFD model is either in the inspiratory or expiratory phase at the same time. For this third interpolation, we used the IVC respiratory waveform as reference an interpolated the respiratory and volumetric flow rate waveforms of the Fontan tunnel and SVC on the IVC using the Pchip function of MATLAB. Figure 43 shows the volumetric flow rate waveforms of each vessel after the third interpolation and phase-shift correction. The unit of the y-axis is now converted to m3/s because that is the unit used in CFD solver software.

The inlets of the CFD model were the IVC, SVC, and hepatic veins (not the Fontan tunnel). Since the hepatic veins were too small for real-time PC-MRI acquisitions, we indirectly quantified the total hepatic venous blood by subtracting the average volumetric flow rate waveform of the IVC from average volumetric flow rate waveform of the Fontan tunnel, leading to a volumetric flow rate waveform of the total hepatic blood flow (figure 44). In other words, we only used the average volumetric flow rate waveform of the Fontan tunnel to quantify the average volumetric flow rate waveform of the hepatic veins. We did not use the average volumetric flow rate waveform of the Fontan tunnel as an inlet boundary condition. Hereafter, the total hepatic venous blood flow was subdivided over the various hepatic veins based on the ratio of their respective cross-sectional areas. The time-varying volumetric flow rate waveforms needed to be decomposed with MATLAB into the Fourier series to make it possible to prescribe the time-varying flow rate waveforms at all inlets. Time-varying flow rates were imposed with a parabolic velocity profile at all inlet vessels[79].

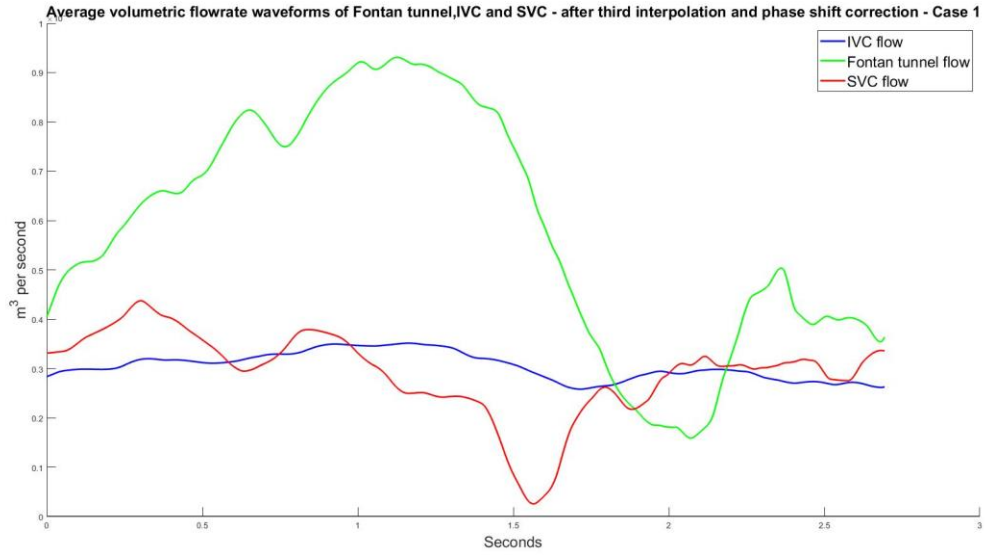

Figure 43: Average volumetric flow rate waveforms of Fontan tunnel, IVC and SVC of Case 1 over the respiratory cycle after third interpolation and phase shift correction

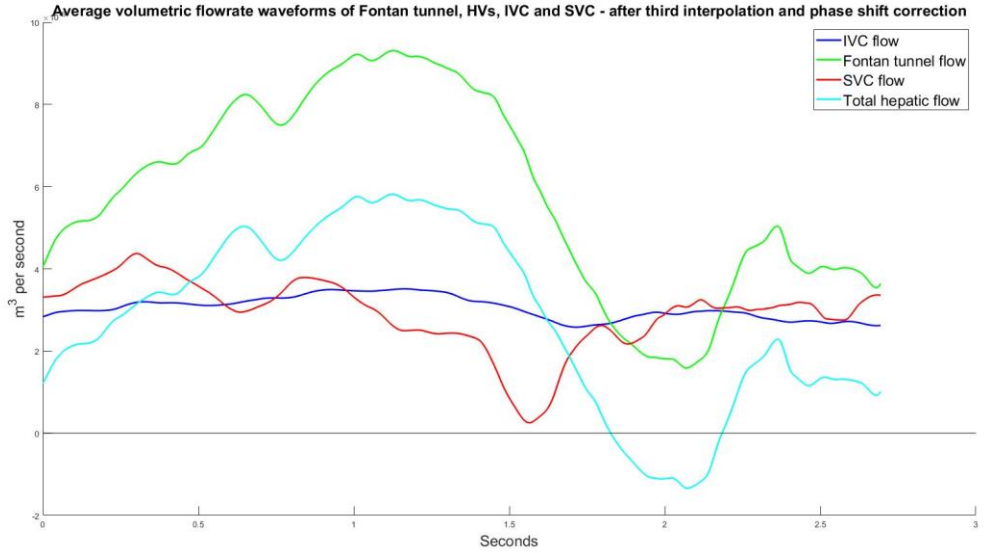

Figure 44: Average volumetric flow rate waveforms of Fontan tunnel, IVC and SVC of Case 1 over the respiratory cycle after third interpolation and phase shift correction

Outlet boundary conditions

At the outlet vessels (the right and left pulmonary arteries), outflow boundary conditions were enforced to guarantee mass convergence. The outflow boundary conditions were imposed as an outflow ratio based on the average pulmonary flow distribution to the right and left lung measured with ECG-gated 2D-3dir PC-MRI. Unfortunately, it was impossible to acquire real-time PC-MRI data of high enough quality of the pulmonary arteries since these vessels were too small. Therefore, we have used ECG-gated 2D-3dir PC-MRI data of the pulmonary arteries to prescribe outflow ratios

Simulation details

Since we decided to only perform a phase-shift correction of the respiratory cycle, we used the respiratory cycle as a reference period in the CFD simulations of part B2. In part B2, we carried out unsteady CFD simulation for three respiratory cycles, simulating 5000 time steps per respiratory cycle. The outcomes of the third respiratory cycle were used for the mixing assessment between hepatic blood with IVC flow within the Fontan tunnel and HFD quantification since it was found that periodic behavior was achieved after simulation of two respiratory cycles. CFD solver software ANSYS-Fluent (v17.1, ANSYS, Inc) was used for all CFD simulations.

Hepatic backflow analysis

The hepatic backflow analysis was performed on the average total hepatic volumetric flow rate waveform shown in figure 44 (without the use of CFD). The percentage of the absolute sum of backward flow (i.e., the flow that is moving away from the heart towards the liver = negative flow) relative to the sum of forward flow (positive flow) was calculated throughout the entire respiratory cycle and during the expiratory and inspiratory phases to explore the percentage of hepatic backflow in Fontan patients.

Post-processing of CFD outcomes

For post-processing, the velocity magnitude vectors for every mesh cell were written to an Ensight Gold case file per every ten time steps as a binary format. Since we used 5000 time steps per respiratory cycle, 5000/10 = 500 files per respiratory cycle were written and used for post-processing.

The assessment of mixing between hepatic and IVC blood flow

We released particles from the hepatic veins and IVC level for the assessment of mixing between the hepatic and IVC blood flow and investigated the degree of mixing at two cross-sections within the Fontan tunnel. The first cross-section was chosen just above the hepatic veins entrance (i.e., caudal cross-section), the second cross-section was just below the pulmonary artery bifurcation (i.e., cranial cross-section). The quantification of mixing between the IVC and hepatic blood flow relies on the spatial distribution of both flows at both cross-sections using the Lagrangian particle tracking tool of Paraview. Based on these velocity magnitude vector files, Paraview created path lines, which are the trajectories that the individual particles follow over time. At both cross-sections, the path line transsections for every time step were registered and used in the mixing analysis. Furthermore, we divided each cross-section in four section: left-anterior, right-anterior, left-posterior and right-posterior. For the assessment of mixing between hepatic and IVC blood flow, we used the time-averaged degree of mixing per each of the four sections over one respiratory cycle ($D_{mixing\_average}$) and the time-averaged degree of mixing of both entire caudal and cranial cross-sections over one respiratory cycle ($D_{mixing\_average\_CS}$), as explained in detail in chapter 3. The degree of mixing was subdivided into six categories: no mixing <0.1, poor mixing 0.1-0.3, mild mixing 0.3-0.5, moderate mixing 0.5-0.7, good mixing 0.7-0.9, uniform mixing >0.9.

Hepatic flow distribution (HFD) quantification (The Lagrangian method)

The second post-processing step was to analyze and compare the HFD towards the lungs between the novel and conventional HFD quantification methods using the Lagrangian particle tracking tool of Paraview. In the two *conventional methods* ($HFD_{caudal\ tunnel}$ & $HFD_{cranial\ tunnel}$), hepatic blood flow particles were uniformly seeded from either a caudal or cranial cross-section, whereas in the *novel method*, particles were directly seeded from the level of the hepatic veins (HFD_{HV}). Chapter 3 explains both the conventional and novel HFD quantification approaches in detail. The HFD ($HFD_{caudal\ tunnel}$, $HFD_{cranial\ tunnel}$ and HFD_{HV}) towards the left and right lung was computed by counting the number of particles leaving the left pulmonary artery and right pulmonary artery and expressed as a percentage of the total particles that were seeded.

Hepatic flow distribution (HFD) quantification (The Eulerian method)

For one case in part B2, we evaluated the HFD_{HV} with the Eulerian method and compared its results with HFD_{HV} outcomes of the Lagrangian method. For both the Lagrangian and the Eulerian method, we used the inlet of the hepatic veins as starting point for HFD_{HV} quantification. So in the Lagrangian method we used the novel HFD quantification method, in which particles were seeded directly from the level of the hepatic veins. For the Eulerian method, we needed to model the hepatic blood flow and the remaining blood flows as two separate mass flow rates. The hepatic blood mass flow rate was prescribed as boundary condition at the inlets of the hepatic veins. The time-varying mass-fractions of both types of flow were written to file and used in the post-processing. For HFD_{HV} quantification, it was necessary to use TECPLOT instead of Paraview. TECPLOT calculated the time-varying hepatic (flow) mass leaving through the left and right pulmonary artery by integrating the mass-weighted flow rate over the time of one respiratory cycle. By calculating the average of the time-varying hepatic (flow) mass over the respiratory cycle's time steps, the HFD_{HV} towards the left and right lung was quantified.

Results

The assessment of mixing between hepatic and IVC blood flow

As illustrated in figures 45 and 46, there was a clear hepatic bloodstream pattern within both cross-sections during the entire respiratory cycle, leading to a uniform distribution of hepatic blood flow in the Fontan tunnel. Notice how small the proportion of hepatic flow is during expiration (figure 46) compared to inspiration (figure 45).

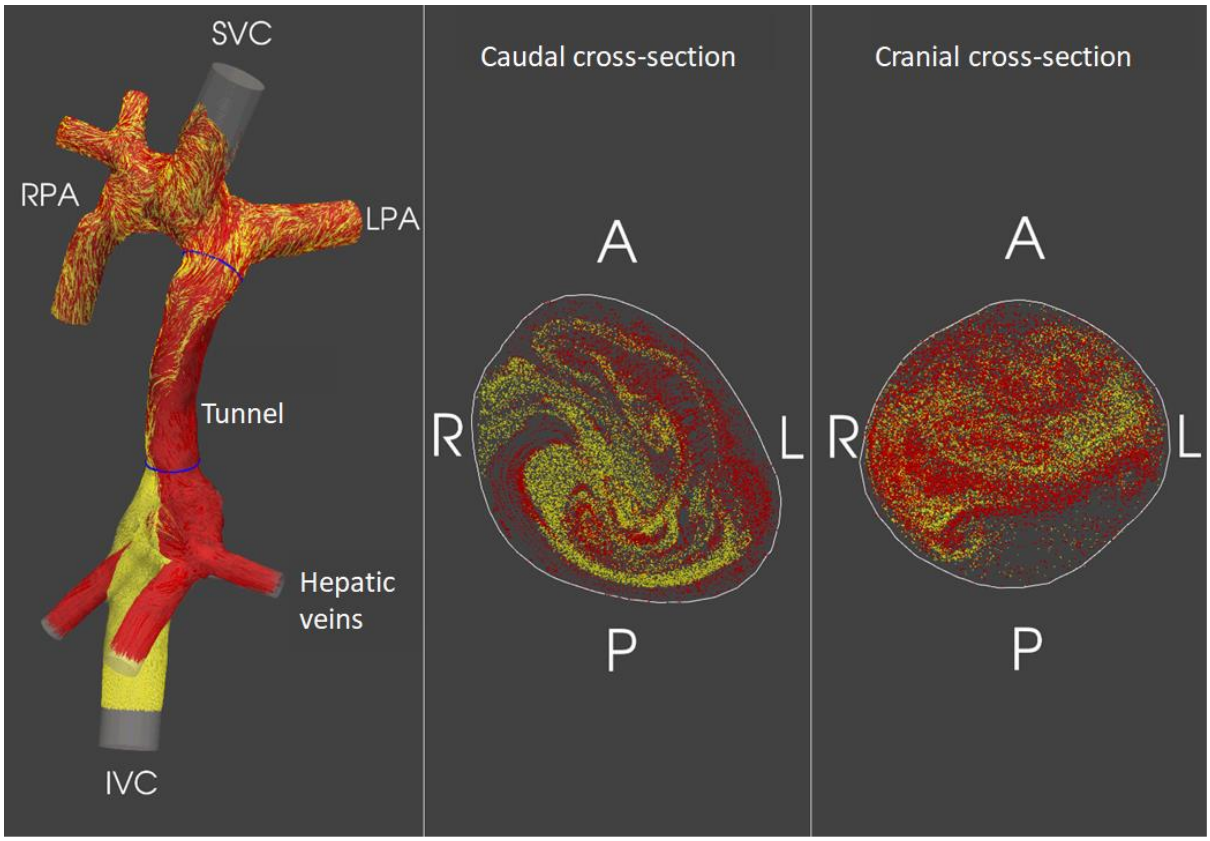

Figure 45: Hepatic (red) and IVC (yellow) bloodstreams at caudal and cranial level during inspiration

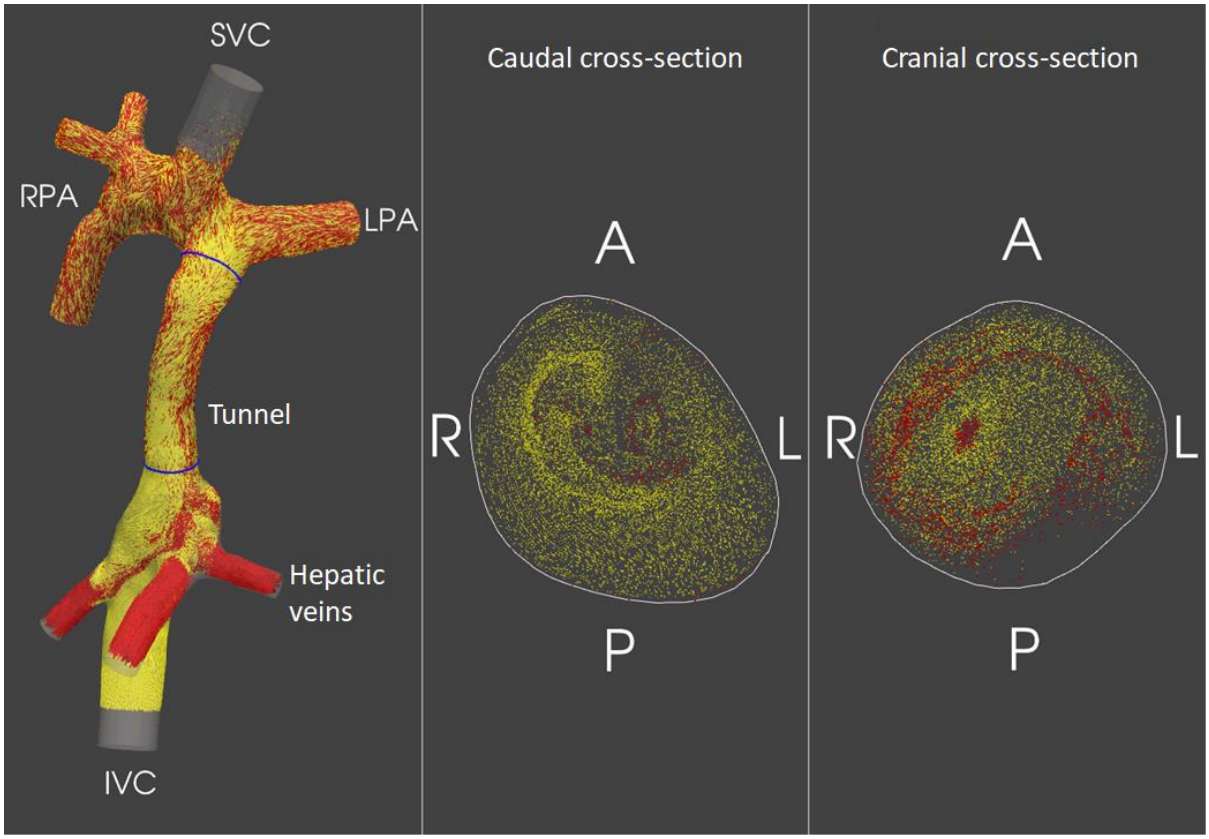

Figure 46: Hepatic (red) and IVC (yellow) bloodstreams at caudal and cranial level during expiration

Table 17 (right column) shows the outcomes of the time-averaged degree of mixing of the entire cross-section for cases 1, 2 and 3 over the respiratory cycle for CFD models that considered respiration. As shown from table 17 (right column), there was no uniformly mixing between the hepatic and IVC blood flow in the Fontan tunnel at the caudal and cranial levels. The caudal degree of mixing ranged from 0.56 to 0.76, whereas the cranial degree of mixing varied between 0.68 and 0.94. Nevertheless, all cases showed improved mixing at the cranial cross-section compared to the caudal cross-section. Figures 47 and 48 support this finding and demonstrate the outcomes of the time-varying degree of mixing of each of the four sections of the caudal and cranial cross-section over the respiratory cycle for the CFD models that incorporated respiration. These figures revealed a clear increase of mixing from the caudal cross-section towards the cranial cross-section.

Interestingly, when comparing the outcomes of CFD models that ignore and consider respiratory effects (part A1 versus part B2), it was found most of the cross-sections in part B2 showed a higher degree of mixing compared to the outcomes of similar cases in part A1, except for the caudal cross-section of case 2. The third column of table 17 demonstrates the previous mixing outcomes for CFD models that ignore respiration obtained in part A1. Although not statistically proven, it seems that respiratory effects on blood flow rates increased the overall degree of mixing at the caudal and cranial cross-sections within the Fontan tunnel.

Table 17: Time-averaged degree of mixing of the entire cross-section for three cases over the respiratory cycle for CFD models that consider respiration

CASE	Cross-section	Degree of mixing of entire cross-section for CFD models that consider only cardiac effects on blood flow (part A1)	Degree of mixing of entire cross-section for CFD models that consider both cardiac and respiratory effects on blood flow (part B2)
Case 1	Caudal	0.49	0.56
	Cranial	0.58	0.68
Case 2	Caudal	0.70	0.63
	Cranial	0.86	0.89
Case 3	Caudal	0.70	0.76
	Cranial	0.86	0.94

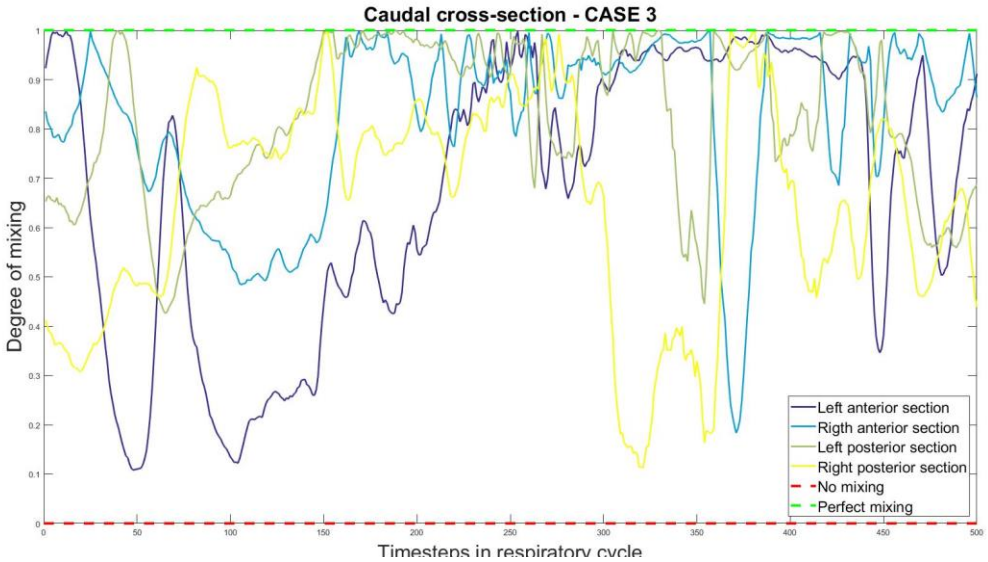

Figure 48: Time-varying degree of mixing for each of the four section of the caudal cross-section of Case 3 over the respiratory cycle

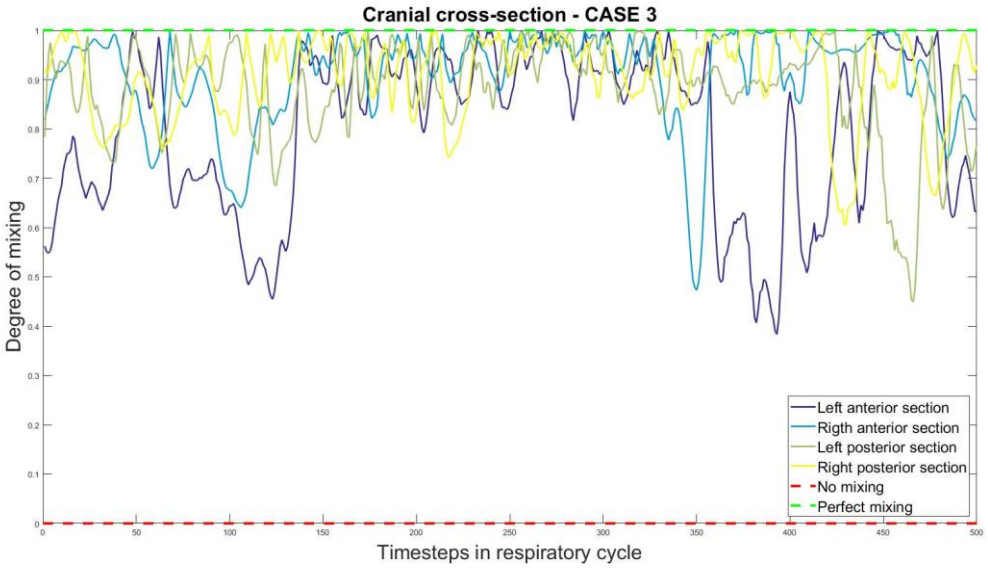

Figure 47: Time-varying degree of mixing for each of the four section of the cranial cross-section of Case 3 over the respiratory cycle

HFD quantification (The Lagrangian method)

The outcomes of HFD quantification of the conventional and novel methods for three cases are demonstrated in table 18. It is clearly visible that there were different HFD results between the conventional and novel HFD quantification methods. For example, concerning case 1, there was an 8.97% difference between the $HFD_{caudal\ tunnel}$ and HFD_{HV} contrary the to maximum variation between the two conventional methods ($HFD_{caudal\ tunnel}$ versus $HFD_{cranial\ tunnel}$) which was only 4.64% for case 3.

Furthermore, we compared the HFD outcomes of both the conventional and novel approaches between CFD models that consider only the cardiac effects on blood flow (part A1) and CFD models that include both the cardiac and respiratory effects (part B2). Table 19 demonstrates the percentage difference between the HFD quantification methods of both types of CFD models. It was captivating that the maximum difference between the conventional HFD quantification method computed with only cardiac dependent flow and cardiac and respiratory dependent flow was maximal 5.53 percent. In contrast, the novel HFD quantification method (HFD_{HV}) findings showed a difference as high as 13.34 percent between CFD models that ignore respiration and consider respiration.

Table 18: Outcomes of HFD quantification over the respiratory cycle of the two conventional and novel HFD quantification methods for CFD models that considered both the cardiac and respiratory effects (part B2)

	$HFD_{caudal\ tunnel}$ (LPA)	$HFD_{caudal\ tunnel}$ (RPA)	$HFD_{cranial\ tunnel}$ (LPA)	$HFD_{cranial\ tunnel}$ (RPA)	HFD_{HV} (LPA)	HFD_{HV} (RPA)
Case 1	62.14%	37.86%	62.25%	37.75%	53.28%	46.72%
Case 2	21.90%	78.10%	21.47%	78.53%	22.87%	77.13%
Case 3	50.94%	49.06%	55.58%	44.42%	50.77%	49.23%

Tabel 19: Differences of HFD quantification between the CFD models that ignore respiration (part A1) and considered respiration (part B2)

	$HFD_{caudal\ tunnel}$ (LPA)	$HFD_{cranial\ tunnel}$ (LPA)	HFD_{HV} (LPA)
Case 1	0.57%	1.50%	13.34%
Case 2	4.55%	3.78%	3.53%
Case 3	3.71%	5.53%	7.04%

HFD quantification using Convection Diffusion modeling (The Eulerian method)

Figure 49 demonstrates the time-varying hepatic flow leaving through the left and right pulmonary artery over the respiratory cycle quantified with the Eulerian method. It is interesting that most of the hepatic flow towards the pulmonary arteries occurs during the first part of the respiratory cycle (during inspiration). The results HFD_{HV} quantification using the Eulerian method for one case (case 3) are shown in table 20. Table 20 also demonstrates that the HFD_{HV} measured with the Eulerian method and Lagrangian method were almost identical. The HFD_{HV} difference between both methods was only 0.62%. Both the Eulerian and Langrangian methods showed their advantages and disadvantages, however, we have only compared one CFD case and definitely further optimization steps that increase efficiency will exist. The advantage of the Eulerian method was that it felt easier to use than the Lagrangian method because after the Fluent data files were uploaded and converted in TECPLOT, a built-in tool in TECPLOT evaluated the HFD_{HV} directly. Furthermore, since the issue of missing particles, however small it may be, does not apply for the Eulerian method, it seemed more sophisticated than the Lagrangian method from an engineering perspective. Another benefit of the Eulerian method was that it was convenient to plot the time-varying hepatic flow leaving through the pulmonary arteries over the respiratory cycle (figure 49). The disadvantages were that the duration of starting the simulation and obtaining the HFD_{HV} outcomes using the Eulerian method was much longer (around two days longer) than the Lagrangian method since the Eulerian method's simulation took more time. Besides, uploading the Eulerian method's data files from the TU Delft cluster and converting the large Fluent data files into TECPLOT lasted longer. Another disadvantage of the Eulerian method is that more data storage is required than for the Lagrangian method. For case 3, there were 508 GB (after converting) and 69,6 GB of data stored for the Eulerian and Lagrangian methods, respectively. Nevertheless, there may be a profit to be gained regarding the data storage by converting the data files to other types of files that are also suitable for TECPLOT.

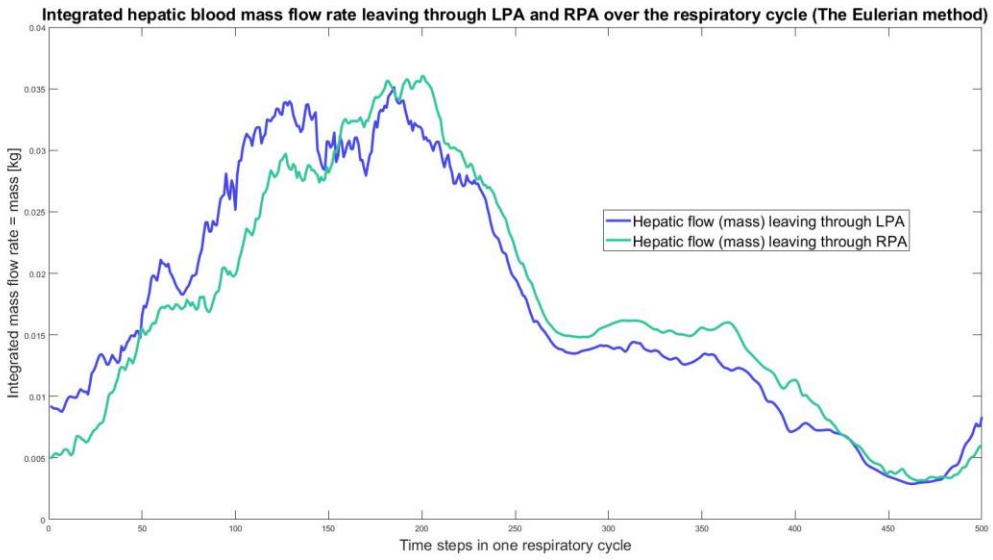

Figure 49: Integrated hepatic blood mass flow rate leaving through the left pulmonary artery (LPA) and right pulmonary artery (RPA) over the respiratory cycle for case 3 of part B2 (Convection-diffusion modeling - The Eulerian method)

Table 20: HFD_{HV} measured with the novel seeding approach and convection diffusion modeling (i.e., The Eulerian method) and HFD_{HV} measured with the Lagrangian method for one CFD case of part B2.

The Eulerian method	**HFD_{HV} (LPA)**	**HFD_{HV} (RPA)**
Case 3	50.15%	49.85 %
The Lagrangian method	**HFD_{HV} (LPA)**	**HFD_{HV} (RPA)**
Case 3	50.77%	49.23%
Difference:	0.62%	

Hepatic backflow analysis

The total hepatic average volumetric flow rate waveforms among the three different cases are shown in figure 50, 51 and 52. The unit of the y-axis is m^3 per second. The red dot in each of those three figures illustrates the end of inspiration and so the start of expiration. The hepatic flow curves of these three Fontan patients demonstrated that retrograde flow primarily occurred during expiration. This observation was supported by the percentages of the absolute sum of backward flow relative to the sum of forward flow. As shown in tables 21, 22, and 23, hepatic backflow was practically only found in the expiratory phase, with expiratory hepatic backflow percentages varying between 1.49% and 30.40%.

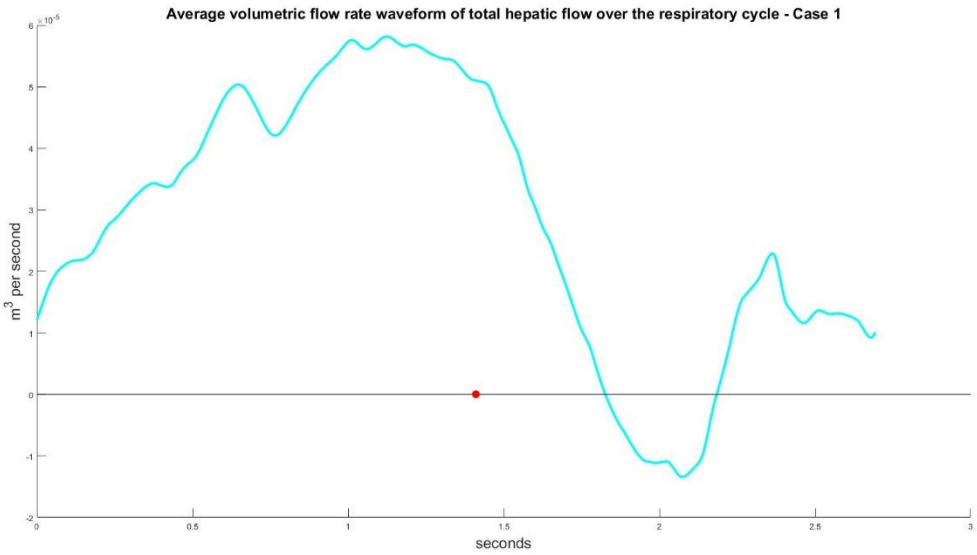

Figure 50: Average volumetric flow rate waveform of total hepatic flow over the respiratory cycle - Case 1 The red dot illustrates the end of inspiration and so the start of expiration

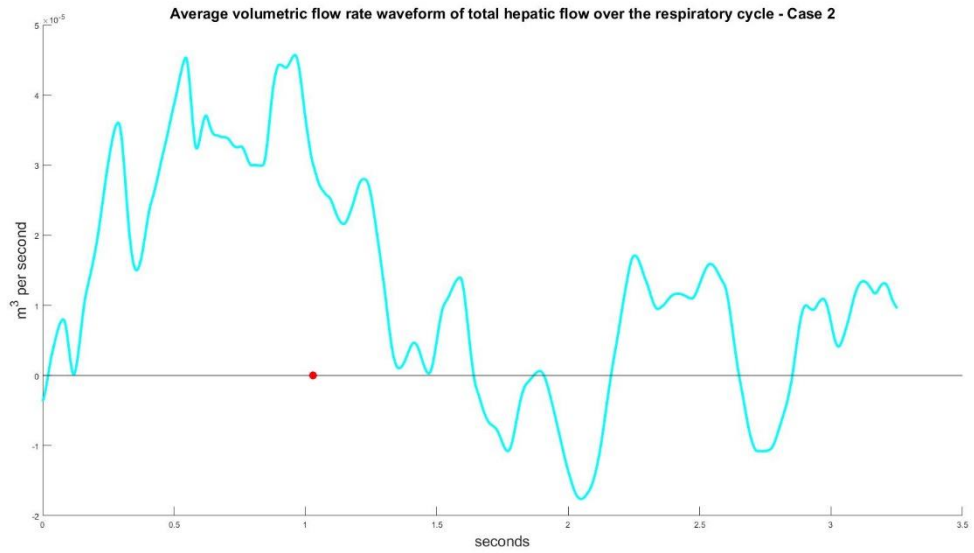

Figure 51: Average volumetric flow rate waveform of total hepatic flow over the respiratory cycle - Case 2 The red dot illustrates the end of inspiration and so the start of expiration

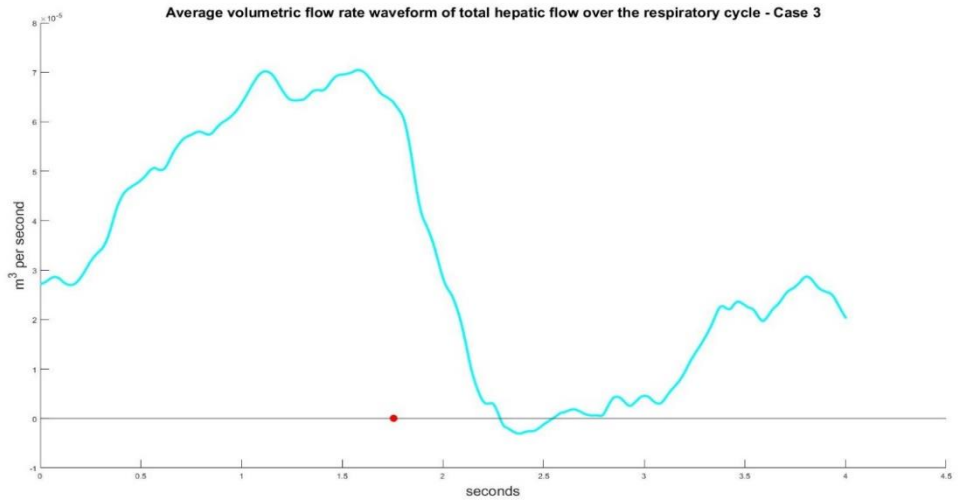

Figure 52: Average volumetric flow rate waveform of total hepatic flow over the respiratory cycle - Case 3 The red dot illustrates the end of inspiration and so the start of expiration

Table 21: Percentage of total backflow relative to total forward flow – Case 1

CASE 1	Percentage of total backflow relative to total forward flow
Full respiratory cycle	4.02%
During expiration	17.0%
During inspiration	0.00%

Table 22: Percentage of total backflow relative to total forward flow – Case 2

CASE 2	Percentage of total backflow relative to total forward flow
Full respiratory cycle	11.90%
During expiration	30.40%
During inspiration	0.17%

Table 23: Percentage of total backflow relative to total forward flow – Case 3

CASE 3	Percentage of total backflow relative to total forward flow
Full respiratory cycle	0.40%
During expiration	1.49%
During inspiration	0.00%

Discussion

In part B2, we wanted to re-examine the mixing assessment of hepatic with IVC blood flow within the Fontan tunnel and HFD values of part A1 using patient-specific CFD models that did consider the cardiac and the respiratory effects on blood flow. So, in part B2, we aimed to test the assessment of mixing between hepatic and IVC blood flow in the Fontan tunnel and the differences between the novel and conventional HFD quantification method again while taking respiration into account. Therefore, we used the same 3D geometrical Fontan models and meshes of three cases as used in part A1, except that part B2 used boundary conditions used that included both the cardiac and respiratory effects on blood flow. The first objectives of part B2 of the master thesis project were to 1. evaluate the degree of mixing of the hepatic blood with the IVC blood in the Fontan tunnel and 2.quantify HFD using particle tracing directly from the hepatic veins (the novel approach), and compare results with the conventional approach while using CFD models that consider both the cardiac and respiratory effects on blood flow.

Similar to chapter A1, the current chapter of this master thesis, there was also a non-uniformly distribution of hepatic blood in the Fontan tunnel when respiratory effects on blood flow were considered. Again, this non-uniform distribution of hepatic blood flow was most noticeable in the caudal cross-section (just above the junction of hepatic veins with the IVC).

In addition, we were also interested in comparing the CFD simulation outcomes of models that only consider the cardiac effects and models that include both the cardiac and the respiratory effects. Interestingly, when comparing the outcomes of CFD models that ignore and consider respiratory effects (part A1 versus part B2), most of the cross-sections in part B2 showed a higher degree of mixing than the outcomes of similar cases in part A1. However, in this proof-of-concept study, we could not statistically prove these differences. We believed that due to the fact that respiration provides more flow pulsatility than heartbeat alone, there was an overall increase of the degree of mixing when comparing these results with the cases of part A1. From previous research, it is known that pulsatile flow can improve the mixing between two separate laminar streams[98], as we find in the Fontan circulation.

Aside from the mixing quantification, we compared the HFD value quantified with a novel and the conventional HFD quantification methods. In the two conventional methods, hepatic blood flow particles were uniformly seeded from either a caudal or cranial cross-section, whereas in the novel method, particles were directly seeded from the level of the hepatic veins. Differences up to 8.97 percent were found between the conventional and novel HFD quantification methods when respiration was taken into account. Although we could not perform statistical analysis, these differences might have a clinical impact on individual patients.

Furthermore, as previously mentioned, clinicians use HFD as a crucial hemodynamic parameter to evaluate Fontan performance. A recent study by Tang et al. investigated the respiratory effects on HFD using the conventional HFD quantification approach, in which 'hepatic blood flow' particles were uniformly seeded from the caudal cross-section in the Fontan tunnel. This conventional method relies on the assumption that hepatic blood flow is uniformly distributed over the Fontan tunnel. Tang et al. compared the CFD-based average HFD of models with and without respiration and found no significant difference in values of the HFD between both the two methods. Therefore, they concluded that respiration did not significantly affect the HFD parameter (1%, with a range of -3% to 7 &, p=0.28)[22]. To test the conclusion of this article by Tang et al, we also compared the HFD outcomes of both the conventional and novel approaches between CFD models that consider only the cardiac effects on blood flow (part A1) and CFD models that include both the cardiac and respiratory effects (part B2). It was captivating that the maximum difference between the cardiac dependent and the cardiac and respiratory dependent outcomes of the conventional HFD quantification method was maximal 5.53 percent. In contrast, the novel HFD quantification method (HFD_{HV}) findings showed a difference as high as 13.34 percent between CFD models that ignored respiration and considered respiration. These findings suggest that the HFD might change substantially between CFD models with and without respiration if the novel HFD quantification approach is applied instead of the conventional HFD quantification method. In turn, this could imply that Tang et al. 's statement that respiration does not significantly affect HFD might not be valid if the novel HFD quantification method is being used. Since this current study only investigated three cases, more research is needed using the novel HFD quantification method in patient-specific CFD models that incorporate the hepatic veins for the evaluation of respiratory effects on the HFD.

Additionally, we also evaluated the Lagrangian and Eulerian method for HFD quantification. This sub-analysis was purely an analysis from a CFD modeling perspective to compare the results and both efficiency in terms of labor intensity and computational time. The main finding was that the difference between both HFD quantification methods was only 0.62% and almost identical. This practically similar result between both methods implies that the Eulerian method could be used as an alternative for HFD quantification; however a larger study is needed to confirm this finding. The minimal difference between the Lagrangian and Eulerian method might be explained by the fact that we had to prescribe a mass diffusivity of 1.54e-09 m2/s as material property for the blood to achieve convection-diffusion modeling (the Eulerian method). The massless particles that we used in the Lagrangian method had no mass diffusivity prescription. Another explanation could be that we missed 1.87% of the hepatic flow particles in the HFD quantification with the Lagrangian method. However, we have

verified that if we provided more time for the particles to reach both PAs, which reduces the percentage of missing particles, it did not affect the HFD_{HV} anymore. With regard to computational efficiency, the Lagrangian method was by far the fastest and required considerably fewer data storage than the Eulerian method. However, the Lagrangian method needed more manual steps and was, therefore, more labor-intensive. The Eulerian method felt intuitively more convenient and sophistaticated than the Lagrangian method. Furthermore, with the Eulerian method, it was quite easy to plot the time-varying hepatic flow leaving through the pulmonary arteries over the respiratory cycle, providing more insight into the hepatic flow streams towards both lungs over the respiratory cycle.

Another fascinating aspect that has been investigated in this current chapter is the respiratory effects on the hepatic backflow analysis. We confirmed the findings of previous clinical imaging studies that retrograde hepatic flow in Fontan patients primarily occurred during expiration. During expiration, the diaphragm moves up and the thoracic pressure increases, leading to a decrease in forward hepatic blood flow[43], which could even turn into reverse hepatic backflow. However, the percentages of hepatic backflow throughout the complete respiratory cycle did not fully match the previous findings of Hsia et al., who found a backflow-to-forward flow ratio of 0.27 ± 0.17[24]. This difference in the amount of hepatic backflow could be explained by the fact that Hsia and colleagues included mainly ILT-type Fontan tunnels (inclusion ILT : ECC was 27 : 6)[24], whereas all patients in our study (of part B2) had an ECC-type Fontan tunnel. Hsia did not subdivide this group but analyzed the entire group as the TCPC (Fontan) group. Although both the ECC-type and ILT-type tunnels are both categorized as TCPC (Fontan) tunnels, it is known that the patients with an ILT-type connection still experience some hepatic backflow due to the contractility of the atrium since the ILT-type connection uses native tissue of right atrial posterior wall to construct the ILT-type Fontan tunnel[31]. The right atrium provides physiological retrograde hepatic backflow patterns during atrial systole, which also occur in healthy subjects[24]. Contrary to the ILT type Fontan tunnel, the ECC-type connection uses a Fontan tunnel that is entirely located outside the atrium, and therefore ECC-type Fontan patients are not subjected to hepatic backflow caused by atrial systolic contractions[31]. Moreover, Hsia et al. used the Doppler signal's velocity-time integral as a surrogate for the flow rate. However, by doing this, they assumed a constant cross-sectional area of the hepatic veins over time. During our clinical imaging acquisitions, we noticed that hepatic veins' cross-sectional areas were not constant over the respiratory cycle because the areas could increase during inspiration and reduce during expiration. Contrary to Hsia et al., we used velocity segmentation, in which the velocity over the vessel's segmented area is integrated over the area to acquire volumetric flow rate waveforms. Although we did not measure the hepatic blood flow directly, we believe that because we used velocity segmentation for the IVC and Fontan tunnel and thereby considered the periodic area changes, the flow quantifications in this study were more reliable than without any consideration of the changing cross-sectional blood vessel areas.

Limitations

Similar to part B1, the findings of part B2 were only based on three Fontan patients. A larger group of Fontan patients is needed for being able to translate results into generalizable insights.

Besides, since the hepatic veins are too small for real-time PC-MRI acquisitions, we indirectly measured the total hepatic blood flow by subtracting the IVC flow (below the entrance of the hepatic veins) from the Fontan tunnel flow. Additionally, we assumed that the total hepatic blood flow was distributed over the different hepatic veins based on the ratio of their respective cross-sectional areas. The validation study, as shown in chapter 3, showed that due phase-correction and interpolation steps in order to acquire volumetric flow rate vectors for all inlets of one respiratory cycle, the absolute magnitude of the flow of the individual blood vessels can change a little compared to raw real-time PC-MRI data. Although we validated that the pulmonary flow distribution between the left and right lung computed with CFD did not change, we adjusted the programming code also to ensure that the computed flow magnitude of all vessels were less than 2 percent different from the flow magnitudes extracted from the real-time PC-MRI flow data. We applied this adjustment from (cardiac and respiratory dependent) case 4 onward, which cases are unfortunately not included in this master thesis report. The adjustment was that we did not use the IVC as a reference blood vessel for the third and final interpolation but created an average respiratory time vector with an average end-inspiration index for interpolation of the Fontan tunnel, SVC and IVC flow on each other. Furthermore, the heart rate could increase during the inspiratory phase and decrease during the expiratory phase, however this phenomenon, generally known as respiratory sinus arrhythmia, mainly occurs in young and healthy subjects. Although it is known that heartbeat barely affects the periodic flow rate changes in Fontan patients, it would have been even more correct if the inlet boundary conditions were also in phase with regard to the cardiac cycle, just like the respiratory cycle. Another limitation concerns the outlet boundary conditions. We approximated the pulmonary vascular resistance of the left and right lung with a constant outflow ratio based on the average pulmonary flow distribution to the right and left lung measured with ECG-gated 2D-3dir PC-MRI. Unfortunately, it was impossible to acquire real-time PC-MRI data of high enough quality of the pulmonary arteries since these vessels were too small. Even though we believed this approach provides a reliable representation of the average pulmonary vascular resistances, these assumptions made could provoke inaccuracies. Furthermore, part B2 mainly focused on exploring the influences of respiration on the assessment of mixing between hepatic and IVC blood flow and HFD quantification. In order to isolate these respiratory influences, we used in part B2 the same geometrical 3D models, meshes and assumptions made in part A1 except that we implemented boundary conditions that consider heartbeat and respiration. Therefore, we assumed a rigid vessel wall in the CFD models similar to part A1. A previously performed study showed that wall compliance barely affects the time-averaged HFD; however, this study did not include the respiratory effects on blood flow. Further research is needed, whether this still holds under the impact of intrathoracic pressure variations related to breathing. Besides, a relatively coarse mixing evaluation was conducted by subdividing the entire cross-sections at the cranial and caudal levels into only four sections. Unfortunately, we did not consider the degree of mixing on smaller scales. Additionally, most Fontan patients included in this study had an ECC-type Fontan tunnel. Although the ECC and ILT-type Fontan tunnel are both TCPC connections, little different flow patterns may exist within the ITL-type tunnel compared to the ECC-type tunnel.

Conclusion

In conclusion, the hepatic blood flow was non-uniformly distributed in the Fontan tunnel when respiration was taken into account. This was most noticeable in the caudal part of the Fontan tunnel. When we compared the CFD simulation results between CFD models that considered only the cardiac effects and both the cardiac and respiratory effects, several exciting findings were found. First of all, most cross-sections in the CFD cases that incorporated the respiratory effects showed a higher degree of mixing than the outcomes of similar cases that ignore the respiratory effects on blood flow. The increased flow pulsatility related to respiration might provide an overall higher degree of mixing of hepatic with IVC blood flow in the Fontan tunnel. Furthermore, the differences between only cardiac and cardiac and respiratory dependent outcomes of the conventional HFD quantification methods were minimal. In contrast, the findings of the novel HFD quantification method showed a difference as high as 13.34 percent between CFD models that ignored respiration and considered respiration. These findings suggest that the HFD might change substantially between CFD models with and without respiration if the novel HFD quantification approach is applied instead of the conventional HFD methods. Additionally, we showed that the Eulerian method could be used as an alternative for HFD quantification; however a larger study is needed to confirm this finding. Lastly, we confirmed the findings of previous clinical imaging studies that hepatic backflow in Fontan patients primarily occur during expiration.

4. General discussion

In this master thesis, we have looked at the hemodynamics in Fontan circulations. Patients with a Fontan circulation still suffer from various long-term complications. One of these long-term complications is pulmonary artery venous malformations (PAVMs) formation. PAVMs are dysfunctional regions in the lungs that cause poor blood oxygenation, resulting in hypoxia, cyanosis, and exercise intolerance. The exact pathogenesis of PAVMs is still unknown, but it is assumed that hepatic blood flow contains a group of molecules 'the hepatic factors' which are crucial for the prevention of the development of PAVMs[13–15]. In other words, a lack of hepatic factors in one of the lungs is associated with PAVMs formation. The liver secretes the hepatic factors into the hepatic blood flow. The hepatic blood flow drains into IVC and is via the Fontan tunnel distributed in both lungs. Therefore, a balanced hepatic flow distribution (HFD) towards both lungs is an important parameter and used by clinicians to evaluate the Fontan performances. This study used computational fluid dynamic (CFD) modeling and phase-contrast magnetic resonance imaging (PC-MRI) to evaluate the HFD. **In part A1** of this master thesis, we performed CFD simulations of 15 Fontan patients. The boundary conditions of the CFD models in part A1 only considered the cardiac effects on blood flow. **In part B2** of this master thesis, we carried out CFD simulations of three Fontan cases and used boundary conditions that incorporated both the cardiac and respiratory effects. We included the respiratory effects into boundary conditions since previous clinical imaging studies showed that respiration profoundly affects the blood flow in the hepatic veins and Fontan tunnel[23–27,29–36,38–41]. The comparison of HFD outcomes between CFD models that ignored respiratory effects on blood flow and considered the impact of respiration gave insight into the influence of respiration on hepatic blood flow and HFD. Besides, we also tested a few assumptions made in previous CFD studies that have investigated HFD in Fontan patients. Moreover, since previous clinical imaging studies reported that the hepatic blood flow in Fontan patients was heavily affected by respiration, we also aimed at studying the impact of respiration on blood flow in Fontan patients ourselves[23–27,29–36,38–41]. Therefore, in addition to CFD modeling used in part A1 and part B2, we also performed an in-depth flow analysis **in part B1**, in which we investigated the respiratory effects on the blood flow waveforms of the inferior vena cava (IVC), superior vena cava (SVC), Fontan tunnel and hepatic veins for three Fontan cases using real-time PC-MRI flow acquisitions. Furthermore, part B1 also studied the impact of respiration on the blood velocity waveforms of the IVC and the Fontan tunnel. The main findings and corresponding discussion points of this master thesis are set out below.

Evaluation of mixing between hepatic and IVC blood flow in the Fontan tunnel

Recent CFD studies indirectly quantify HFD to the left pulmonary artery and right pulmonary artery by tracking 'hepatic flow' particles that are uniformly seeded in the Fontan tunnel and analyzing these particles' distribution towards both lungs (which we called the *conventional approach*) [18–22]. However, this conventional approach is based on an unvalidated assumption that there is a uniform distribution of hepatic blood in the Fontan tunnel. Because Reynolds numbers in the Fontan tunnel are usually low, the Fontan tunnel's blood flow behaves laminar. Due to this laminar flow behavior, the mixing of blood from the hepatic veins and the IVC

might be far from optimal contrary to what is generally assumed and so the question rises whether this assumption of uniform hepatic flow distribution within the Fontan tunnel is correct. Therefore, this study aimed to test this assumption of uniform distribution of hepatic blood flow within the Fontan tunnel. To achieve this, we created patient-specific CFD models that included the geometry of the hepatic veins into the computational fluid domain. These CFD models that incorporated the hepatic veins made it possible to seed 'hepatic flow' particles directly from the level of the hepatic veins (*the novel approach*). We believed that seeding 'hepatic flow 'particles directly from the hepatic veins would provide physiologically more realistic hepatic blood flow patterns. Hereafter, we evaluated the degree of mixing between hepatic and IVC blood flow in the Fontan tunnel at two cross-sections within the Fontan tunnel: the caudal cross-section (just above the entrance of the hepatic veins into the IVC) and the cranial cross-section (just below the pulmonary artery bifurcation). First, in part A1, we quantified the degree of mixing between hepatic and IVC blood flow at the two cross-sections using CFD models that only took the cardiac effects on blood flow into account, but ignored the respiratory effects on blood flow. Secondly, in part B2, we evaluated the degree of mixing between hepatic and IVC blood flow at similar cross-sections but using CFD models that considered both the cardiac and respiratory effects on blood flow. One of the key findings of this master thesis was that the 15 CFD simulations with boundary conditions that only considered cardiac effects on blood flow in part A1, statistically proved that hepatic blood flow was non-uniformly distributed within the Fontan tunnel. Furthermore, there was a significantly better mixing between hepatic blood and IVC blood flow at the cranial level than at caudal level, but the hepatic blood flow was still not uniformly mixed over the Fontan tunnel. The explanation of this non-uniform mixing of hepatic with IVC blood flow in the Fontan tunnel is that both bloodstreams have a laminar behavior with low pulsatility throughout the cardiac cycle, resulting in less ideal mixing. The clarification for the higher degree of mixing of hepatic with IVC blood flow at the cranial level is that both the hepatic and IVC bloodstreams had more time to mix at this more upstream level. Based on these findings of part A1, it can be concluded that the previously used assumption of an even distribution of hepatic blood flow within the Fontan tunnel is not valid [18–21], at least in CFD models with only cardiac-dependent boundary conditions.

Similar to the findings of part A1, the outcomes of CFD simulations that considered both the cardiac and respiratory effects on blood flow (part B2) also showed that the hepatic blood flow was non-uniformly distributed in the Fontan tunnel. Besides, part B2 also demonstrated a higher degree of mixing between hepatic and IVC blood flow in the cranial cross-section than in the caudal cross-section. Interestingly, it seems that the respiratory effects increased the overall degree of mixing between hepatic and IVC blood flow compared to CFD models that only considered the cardiac effects on blood flow. The improved mixing properties between hepatic and IVC blood flow when respiration is taken into account might be because respiration is primarily responsible for the flow pulsatility in Fontan tunnel and hepatic veins in Fontan patients[24,26,27,29–31,34–37]. It is known that pulsatile flow can enhance the mixing between two separate laminar streams[98], as we find in the Fontan circulation. The assessment of the mixing of hepatic with IVC blood flow within the Fontan tunnel, when taken respiration into account in this proof of concept, has only been investigated for three cases. Therefore, more research

is needed to evaluate if there is a truly significant respiration role on the mixing properties between hepatic and IVC blood flow within the Fontan tunnel.

Blood **flow** analysis of the SVC, IVC, Fontan tunnel and hepatic veins

In part B1, we used real-time PC-MRI flow acquisitions to evaluate the respiratory effects on blood flow waveforms. In part B1, we performed purely in-depth flow (and velocity) analysis without CFD. Real-time PC-MRI stands for free-breathing non-ECG gated non-navigator gated two-dimensional through-plane PC-MR imaging. Due to the absence of navigator and ECG-gating, and the fact that the patient could breathe freely during MRI acquisitions, real-time PC-MRI data contains full information about the respiratory impact on blood flow waveforms. Although it is not possible to measure the blood flow in the hepatic veins directly, real-time PC-MRI has multiple advantages over Doppler Ultrasound. First, PC-MRI is less dependent on the examiner and has, therefore, a higher inter-observer reproducibility[44,45]. Secondly, when using Doppler Ultrasound, assumptions about basic flow profiles and cross-sectional vessel areas, need to be made to calculate mean velocities and net flow rates. These assumptions may produce imprecise flow calculations in the presence of complicated vessel geometry or flow[46], which does not apply to PC-MRI measurements. Despite the fact that the resolution of real-time PC-MRI is not yet good enough for the hepatic flow distribution, in this master thesis, we introduced a novel approach to indirectly measure the hepatic flow in the hepatic veins during the respiratory cycle using real-time PC-MRI. First, we measure the blood flow in the Fontan tunnel, just proximal to the hepatic veins' entrance. Second, we derive the IVC blood flow caudal from the hepatic veins. By subtracting these mean flows, we indirectly quantified the mean hepatic blood flow. Using this method, we were able to investigate the respiratory effects on the blood flow of the SVC, IVC, Fontan tunnel and the hepatic veins while using real-time PC-MRI (part B1). The main finding was that we confirmed what has previously been described that respiration heavily influences the blood flow in the hepatic veins and Fontan tunnel. The flow rates in the Fontan tunnel and hepatic veins increased dramatically during inspiration, then decreased during expiration. The inspiration-to-expiration flow ratio of the Fontan tunnel and hepatic veins varied, respectively, from 1.82 to 1.97 and from 3.53 to 4.88. Interestingly, the hepatic veins' inspiratory-to-expiratory flow ratios were in close agreement to previous Doppler studies that revealed a hepatic inspiratory-to-expiratory flow ratio, varying between 2.9 and 4.3[24,34–36,41]. If we compare the obtained inspiration-to-expiration flow ratio of the hepatic veins in this study to the only the outcomes Hsia et al, our findings fell exactly within their described standard deviation (3.4 +/- 1.5). Besides, we did investigate not only the flow rate changes over the respiratory cycle but also studied the percentage of flow that was solely depending on inspiration. Closely in line with the Doppler Ultrasound measurements of Hsia et al., who described a 55 percentage of hepatic inspiratory dependency, we found that the hepatic blood flow was for 55.0 % to 66.0% dependent on inspiration. These results means the hepatic blood flow is dominated by inspiration. Not only the measurements of the hepatic blood This study's Fontan tunnel flow was for 29.2% and 32.7% dependent on inspiration, similar to what has been previously described[24,25]. Furthermore, the IVC and SVC flow were less affected by respiration, similar to earlier described. Although the in-depth flow analyses of part B1 have been conducted for only three

Fontan cases, the findings suggested two essential points: 1. Respiration is indeed important and plays a major role in the flow dynamics of the Fontan tunnel and especially the hepatic veins in Fontan patients, 2. The feasibility of deriving hepatic flow from real-time PC-MRI acquisitions. Therefore, real-time PC-MRI might be a new opportunity for evaluating the hepatic blood flow in Fontan patients and the respiratory effects on it instead of using the gold standard Doppler Ultrasound. However, a drawback of using real-time PC-MRI to quantify hepatic blood flow is that a MATLAB programming code is needed to extract and analyze the respiratory waveform and its corresponding flow rate waveform for each vessel. The current MATLAB code that we generated is semi-automatic and still consists of a few manual checks. However, it is possible to professionally optimize the code to a software program that fully automatically evaluates the real-time PC-MRI data and its corresponding respiratory signal. Nevertheless, future research is needed to elucidate the potential of deriving hepatic blood flow from real-time PC-MRI on a clinically routine basis. Another disadvantage, in contrast to Doppler Ultrasound, the MRI machine is not portable, and therefore, the patient should always come to the MRI scan if real-time PC-MRI acquisitions are desirable.

Blood **velocity** analysis of the IVC and Fontan tunnel using real-time PC-MRI

Apart from the in-depth flow analysis, as described above, we also studied the respiratory effects on the blood flow velocity in the IVC and Fontan tunnel while using real-time PC-MRI. We analyzed the blood velocity in the IVC and Fontan tunnel because we used these velocity values to calculate the so-called IVC-tunnel mismatch. The IVC-tunnel mismatch parameter was introduced by Rijnberg et al. and defined as an increase of mean velocity from the IVC towards the Fontan tunnel[92]. The relative difference between the mean velocity in the IVC and Fontan tunnel needed to be calculated to evaluate if there was an IVC-tunnel mismatch. This article stated that IVC-tunnel mismatch is highly correlated with energy loss. In its turn, energy loss is related to reduced exercise tolerance and hence more inferior clinical outcomes[93]. Unfortunately, Rijnberg et al. did not distinguish between inspiratory and expiratory flow data, and therefore they could not investigate the impact of respiration on the IVC-tunnel mismatch parameter. This study's strength is that we evaluated the IVC-tunnel mismatch parameter for three Fontan cases during inspiration, during expiration, and throughout the entire respiratory cycle. We discovered that IVC-tunnel mismatch during inspiration varied between 80.5% and 291.0%, meaning an increase of velocity between 80.5 and 291.0 percent from the IVC towards the Fontan tunnel during the inspiratory phase. Interestingly, although the IVC-tunnel mismatch was much less pronounced during expiration (ranging from 29.7% to 124.3%), there was still an IVC-tunnel mismatch during the expiratory phase. Although we only studied a small sample size, these findings suggested two important things: 1. When evaluating the IVC-tunnel mismatch, it is important to distinguish between the inspiratory and expiratory phase since the IVC-tunnel mismatch parameter showed large variations over the respiratory cycle, 2. There was an IVC-tunnel mismatch during the entire respiratory cycle in all three cases. This cannot be healthy from a fluid dynamic perspective since an IVC-tunnel mismatch is highly correlated with energy losses throughout the Fontan circulation and reduced exercise tolerance[92,93].

Hepatic flow distribution (HFD) quantification

Ultimately, the most important hemodynamic parameter investigated in this study was the HFD towards both lungs. An unbalanced HFD is associated with PAVMs formation in the affected lung. We wanted to understand the mixing between hepatic blood and IVC flow within the Fontan tunnel and the respiratory effects on the blood flow waveforms as described in the previous paragraphs since, after all, these aspects might influence the HFD or may invalidate the way HFD was quantified in previous research. CFD simulations were performed to acquire the time-varying velocity field. Based on the time-varying velocity data, particle tracking was conducted using ParaView software (the Lagrangian method). We used three different HFD quantification methods; In the two conventional methods, hepatic blood flow particles were uniformly seeded from either a caudal or cranial cross-section similar to what has been done in previous research. In our novel invented method, particles were directly seeded from the inlets of the hepatic veins. The HFD towards the left and right lung was computed by counting the number of particles leaving the left pulmonary artery and right pulmonary over time. In part A1, we used boundary conditions that only considered the cardiac effects on blood flow, whereas in part B2, both the cardiac and the respiratory effects on blood flow were taken into account at the boundary conditions. Since we performed 15 CFD simulations in part A1, we were able to carry out additional statistical analysis. However, in part B2, we only investigated three CFD cases.

HFD results of CFD simulations that only consider the cardiac effects on blood flow (part A1)

A significant difference was found in HFD between the conventional method, in which hepatic blood flow particles were uniformly seeded from either a caudal or cranial cross-section, and the novel method, in which particles are directly seeded from the level of the hepatic veins. However, although significant, these differences were relatively small and had no clinical relevance on-group level. For this reason, the fact that there was a non-uniform distribution of hepatic blood flow in the Fontan tunnel did, in general terms, not affect the HFD quantification with clinical significance. Therefore, the findings of previously performed CFD studies that only considered cardiac effects on blood flow are on group-level still valid[18–21]. Nevertheless, it should be emphasized that on individual basis differences, as high as 14.9% were found in patients, which may have implications for the patient-specific decision making about the need for intervention and therefore, could have a meaningful clinical impact on individual patients.

HFD results of CFD simulations that consider both the cardiac and respiratory effects on blood flow (part B2)

Similar to part A1, it was clearly visible that there were different HFD results between the conventional and novel HFD quantification methods using CFD models with respiration. Differences up to 8.97 percent were found between the conventional and novel HFD quantification methods when respiration was taken into account. Although we could not perform statistical analysis, these differences might have a clinical impact on individual patients. Furthermore, as previously mentioned, clinicians use HFD as a crucial hemodynamic parameter to evaluate Fontan performance. A recent study by Tang et al. investigated the

respiratory effects on HFD using the conventional HFD quantification approach, in which 'hepatic blood flow' particles were uniformly seeded from the caudal cross-section in the Fontan tunnel. This conventional method relies on the assumption that hepatic blood flow is uniformly distributed over the Fontan tunnel. Tang et al. compared the CFD-based average HFD of models with and without respiration and found no significant difference in values of the HFD between both the two methods. Therefore, they concluded that respiration did not significantly affect the HFD parameter (1%, with a range of -3% to 7 &, p=0.28)[22]. To test the conclusion of this article by Tang et al, we also compared the HFD outcomes of both the conventional and novel approaches between CFD models that consider only the cardiac effects on blood flow (part A1) and CFD models that include both the cardiac and respiratory effects (part B2). It was captivating that the maximum difference between the cardiac dependent and the cardiac and respiratory dependent outcomes of the conventional HFD quantification method was maximal 5.53 percent. In contrast, the novel HFD quantification method (HFD_{HV}) findings showed a difference as high as 13.34 percent between CFD models that ignored respiration and considered respiration. These findings suggest that the HFD might change substantially between CFD models with and without respiration if the novel HFD quantification approach is applied instead of the conventional HFD quantification method. In turn, this could imply that Tang et al. 's statement that respiration does not significantly affect HFD might not be valid if the novel HFD quantification method is being used. Since this current study only investigated three cases, more research is needed using the novel HFD quantification method in patient-specific CFD models that incorporate the hepatic veins for the evaluation of respiratory effects on the HFD.

Additionally, we also evaluated the Lagrangian and Eulerian method for HFD quantification for one CFD case that incorporated the respiratory effects on blood flow. The Eulerian method uses the concentration of particles and computes the overall convection and diffusion of a number of particles. This sub-analysis was purely an analysis from a CFD modeling perspective to compare the results and efficiency in labor intensity and computational time. The main finding was that the difference between both HFD quantification methods was only 0.62% and almost identical. This practically similar result between both methods implies that the Eulerian method could be used as an alternative for HFD quantification; however a larger study is needed to confirm this finding.

5. Future research and recommendations

Future research could focus on different aspects. Future investigations can extend the current findings of the in-depth flow analysis using real-time PC-MRI in chapter B1 or the current outcomes of CFD simulations using boundary conditions that considered both the cardiac and respiratory effects on blood flow in chapter B2. Both parts B1 and B2 only investigated three cases, so more research is needed to perform statistical analysis and translate results into generalizable insights. These insights will hopefully give answers to the following questions: 1. Is there a truly significant respiration role on the mixing properties between hepatic and IVC blood flow within the Fontan tunnel, 2. What is the effect of respiration on the HFD using the novel HFD quantification method in CFD models that consider both the cardiac and respiratory effects on blood flow? 3. What is the exact impact of respiration on blood flow in the SVC, IVC, Fontan tunnel and hepatic veins using real-time PC-MRI and flow analysis as developed in this study? 4. Could real-time PC-MRI be a reliable alternative imaging method to investigate the hepatic blood flow in Fontan patients instead of using Doppler Ultrasound?

Future research can also explore the impact of various Fontan patient characteristics on hemodynamic parameters such as inspiration-to-expiration flow ratio, IVC-tunnel mismatch, and HFD. Examples of different Fontan characteristics are the type of TCPC connection (ILT versus ECC-type Fontan tunnel), Fontan tunnel diameter size (small versus large diameters), and well versus poor functioning Fontan patients. Besides, we have made some assumptions in the CFD simulations. These assumptions are well-founded and commonly used in Fontan hemodynamic modeling, but it would be interesting to analyze the impact of these assumptions. Some specific recommendations are set out below in more detail.

Specific recommendations

Type of TCPC (Fontan) tunnel (ECC versus ILT)

It would be interesting to investigate whether the type of TCPC tunnel influences important hemodynamic parameters, as investigated in this study. Both the ECC and ILT type tunnels are categorized as TCPC tunnels. However, there may exist little differences in flow patterns within the ITL-type tunnel compared to the ECC-type tunnel that could influence different hemodynamic parameters such as HFD, mixing properties between hepatic and IVC blood flow in the Fontan tunnel and the IVC-tunnel mismatch parameter.

Diameter size of Fontan tunnel

The study of Rijnberg et al. showed that the IVC-tunnel mismatch depends on the Fontan tunnel's diameter. However, this article did not investigate the role of respiration on the IVC-tunnel mismatch[92]. Therefore, it would be worthwhile to study the influences of Fontan tunnel diameter size and respiration on the IVC-tunnel mismatch parameter. A next step could be to evaluate the energy losses within the Fontan tunnel using CFD and relate this to the IVC-tunnel mismatch. Hereafter, the poor functioning Fontan patients (i.e., energy losses) can be selected.

With the usage of virtual surgery (also known as virtual surgical planning), the Fontan tunnel can be 'virtually' adjusted to a desirable diameter size. With virtual surgery, it is possible to 'virtually' change the patient-specific geometrical model using software programs. These adapted geometrical models can be used in new CFD simulations to investigate whether or not energy losses improve.

Compliance of vessel wall

In order to isolate the respiratory influences on HFD quantification, we used a rigid vessel wall assumption in both CFD models that ignored (part A1) and considered (part B2) the respiratory effects on blood flow because we wanted to make a proper comparison between both types of CFD models. A previously performed study showed that wall compliance barely affects the time-averaged HFD; however, this study did not include the respiratory effects on blood flow. Further research is needed, whether this still holds under the impact of intrathoracic pressure changes related to respiration. A novel study could, for instance, implement wall compliances at the wall of the following veins: IVC, Fontan tunnel, hepatic veins and SVC. The left and right pulmonary arteries are arteries instead of veins and therefore contain elastic fibers. Therefore, arteries are more elastic than veins. To account for these elastic properties of the pulmonary arteries, a commonly used three-element Windkessel (resistor-capacitor-resistor) could be prescribed at the left and right pulmonary arteries. The first resistor represents the pulmonary artery's resistance, whereas the second resistor accounts for the peripheral resistance. The capacitor signifies the compliance of the pulmonary artery. Unfortunately, pressure data or assumptions about the pressure field are necessary to be able to calculate the compliance[57,99]. Pressure data are obtained using invasive cardiac interventions named catheterizations, which are not conducted for research purposes only in the Netherlands. However, some Fontan patients might have recent pressure data obtained from clinical catheterizations that can be used to determine compliance. Otherwise, assumptions about the pressure field or wall compliance based on literature may be used instead. Another word for simultaneously modeling of the blood flow and wall deformation is fluid-solid interaction modeling. After the determination of the compliances, the respiratory effects on HFD could be examined. Hereafter, the assumption that wall compliance barely affects the time-averaged HFD can be validated, also when respiratory effects on blood flow are taken into account.

Analyzing of the cardiac and respiratory effects on blood flow when using real-time PC-MRI

Although the real-time PC-MRI flow data include both cardiac and respiratory effects on blood flow, we only investigated the respiratory effects on blood flow in part B1. Besides, we only corrected the inlet boundary conditions in the CFD simulations for the respiratory phase in part B2. Both the analyzed blood flow waveforms in part B1 and the inlet boundary conditions of part B2 also contain information about the cardiac effects on blood flow. Although the cardiac effects on blood flow were included in all calculations made in part B1 and B2, we did not analyze or visualize these cardiac effects separately. Since it is known that heart rate could vary with respiration, which is called respiratory sinus arrhythmia (RSA)[97], it would be interesting to study the cardiac and respiratory effects on blood flow separately from each other when using real-time PC-MRI. On the other hand, it is known that RSA mostly occurs in young and

healthy subjects[97], which Fontan patients are not. Moreover, previous research that studied the cardiac and respiratory effects on blood flow separately using real-time PC-MRI has already demonstrated that respiration is primarily responsible for the flow pulsatility in the Fontan tunnel and hepatic veins in Fontan patients[24,26,27,29–31,34–37]. Furthermore, these studies also showed that the cardiac cycle barely affects the flow rate changes in Fontan circulations, which is quite logical since the Fontan tunnel bypasses the heart and is directly connected to the lungs.

Flow instabilities at level of the pulmonary artery bifurcation

Blood flow is usually considered as laminar flow and therefore, most recent CFD studies assumed laminar flow behavior[79,100–102]. However, we discovered that peak Reynold's number within one case could reach values between roughly 1978 and 2748 for a short period during the cardiac and respiratory cycle. These Reynolds numbers identify regions that are in transition between laminar and turbulent flow behavior. Related to the latter observation, it was found that exactly at the locations where Reynolds numbers indicate that flow is in transition to turbulence, the periodic flow behavior was not achieved probably due to the flow instabilities. Nevertheless, because there were low Reynolds numbers most of the time, representing the laminar flow, we assumed laminar behavior in our CFD simulations similar to previous CFD studies that investigate Fontan circulations[79,100–102]. However, it would be interesting to thoroughly investigate the time-varying Reynolds numbers throughout the entire Fontan geometry for multiple cases to understand the flow behavior within Fontan patients exactly. Based on these Reynolds numbers, it would be worthwhile to explore the possibility of turbulence modeling of the Fontan circulations.

6. General Conclusion

In this master thesis, we have looked at the hemodynamics in patients with a Fontan circulations. We showed that hepatic blood was non-uniformly distributed within the Fontan tunnel in CFD models that considered only the cardiac effects on blood flow and CFD models that took both the cardiac and respiratory effects on blood flow into account. The CFD models that included only the cardiac effects demonstrated a significantly higher degree of mixing between hepatic and IVC blood flow at the cranial level (just below the pulmonary artery bifurcation) than at the caudal level (just above the entrance of the hepatic veins into the IVC) within the Fontan tunnel. However, also at the cranial part of the Fontan tunnel, the hepatic blood flow was still not uniformly mixed. Similar to the CFD simulations that included only cardiac-dependent flow, the CFD models that considered both the cardiac and respiratory effects on blood also showed a higher degree of mixing at the cranial level compared to the caudal level; however, because of the small sample size, statistical analyses could not be performed. Interestingly, including respiratory effects into CFD modeling increased the overall degree of mixing between hepatic and IVC blood flow in the Fontan tunnel compared to CFD models that only considered the cardiac effects on blood flow. The improved mixing properties of hepatic with IVC flow when respiration is taken into account might be due to the fact that respiration is primarily responsible for the flow pulsatility in Fontan tunnel and hepatic veins. From previous research, it is known that pulsatile flow can improve the mixing between two separate laminar streams.

Regarding the HFD quantification, the CFD models that ignored respiration showed a significant difference in HFD between the conventional method, in which hepatic blood flow particles are uniformly seeded from either a caudal or cranial cross-section, and the novel method, in which particles are directly seeded from the level of the hepatic veins. However, although significant, these differences were relatively small and had no clinical relevance on-group level. For this reason, the fact that there was a non-uniform distribution of hepatic blood flow in the Fontan tunnel did, in general terms, not affect the HFD quantification with clinical significance. Therefore, the findings of previously performed CFD studies that only considered cardiac effects on blood flow are on the group-level still valid. Nevertheless, it should be emphasized that on an individual basis, differences as high as 14.9% were found in patients, which may have implications for the patient-specific decision making about the need for intervention and, therefore, could have a meaningful clinical impact on individual patients. When considering CFD models that include both the cardiac and respiratory effects on blood flow, also substantial differences were found in HFD between the conventional and novel HFD quantification approaches. Since this current study only investigated three CFD cases that included both the cardiac and respiratory effects at the boundary conditions, more research is needed using the novel HFD quantification method in patient-specific CFD models for the evaluation of respiratory effects on the HFD.

In addition to the CFD simulations, the in-depth flow analysis using real-time PC-MRI showed that respiration tremendously affected the blood flow in the Fontan tunnel and hepatic veins. Therefore, we could confirm that inspiration and expiration are responsible for

the large variations in hepatic and Fontan tunnel flow rate over the respiratory cycle. Besides, we demonstrated the feasibility of deriving hepatic flow from real-time PC-MRI acquisitions.

References

1. van der Wall EE, van de Werf F, Zijlstra F. *Cardiologie*. Tweede dru. Bohn Stafleu van Loghum; 2008.
2. Khiabani RH, Yoganathan AP, de Zelicourt D. Effect of Flow Pulsatility on Modeling the Hemodynamics in the Total Cavopulmonary Connection. *J Biomech*. 2012;45(14):2376-2381. doi:10.1161/CIRCULATIONAHA.110.956839
3. Helbing WA, van der Ven JPG, van den Bosch E, Bogers AJCC. State of the art of the Fontan strategy for treatment of univentricular heart disease [version 1; referees: 2 approved]. *F1000Research*. 2018;7. doi:10.12688/f1000research.13792.1
4. Rai V, Gładki M, Dudyńska M, Skalski J. Hypoplastic left heart syndrome [HLHS]: treatment options in present era. *Indian J Thorac Cardiovasc Surg*. 2019;35(2):196-202. doi:10.1007/s12055-018-0742-z
5. Maher KO, Pizarro C, Gidding SS, et al. Hemodynamic profile after the Norwood procedure with right ventricle to pulmonary artery conduit. *Circulation*. 2003;108(7):782-784. doi:10.1161/01.CIR.0000087338.09589.21
6. Tanoue Y, Kado H, Boku N, et al. Three hundred and thirty-three experiences with the bidirectional Glenn procedure in a single institute. In: *Interactive Cardiovascular and Thoracic Surgery*. Vol 6. Oxford Academic; 2007:97-101. doi:10.1510/icvts.2006.138560
7. Warrier G, Ch M, Dharan BS, et al. Bidirectional glenn operation in infancy. *Dep Cardiovasc Thorac Surgery,*. 2004;20:159-163.
8. Abdulla R-I. The Fontan Procedure: Now What? *Pediatr Cardiol*. 2014;35:1307-1308. doi:10.1007/s00246-014-1067-3
9. Jonas RA. The fenestrated Fontan procedure. *Herz*. 1997;17(4):242-245.
10. de Leval MR, Kilner P, Gewillig M, Bull C. Total cavopulmonary connection: a logical alternative to atriopulmonary connection for complex Fontan operations. Experimental studies and early clinical experience. *J Thorac Cardiovasc Surg*. 1988;96(5):682-695.
11. Fredenburg TB, Johnson TR, Cohen MD. The Fontan procedure: anatomy, complications, and manifestations of failure. *Radiographics*. 2011;31(2):453-463. doi:10.1148/rg.312105027
12. Khairy P, Poirier N. Is the extracardiac conduit the preferred fontan approach for patients with univentricular hearts?: The extracardiac conduit is not the preferred fontan approach for patients with univentricular hearts. *Circulation*. 2012;126(21):2516-2525. doi:10.1161/CIRCULATIONAHA.111.075036
13. Pike NA, Vricella LA, Feinstein JA, Black MD, Reitz BA. Regression of severe pulmonary arteriovenous malformations after Fontan revision and "hepatic factor" rerouting. *Ann Thorac Surg*. 2004;78(2):697-699. doi:10.1016/j.athoracsur.2004.02.003
14. Vettukattil JJ. Pathogenesis of pulmonary arteriovenous malformations: role of hepatopulmonary interactions. 2002:561-563.
15. Kavarana MN, Jones JA, Stroud RE, Bradley SM, Ikonomidis JS, Mukherjee R. Pulmonary arteriovenous malformations after the superior cavopulmonary shunt: mechanisms and clinical implications. *Expert Rev Cardiovasc Ther*. 2014;12(6):703-713. doi:10.1586/14779072.2014.912132
16. Haggerty CM, Restrepo M, Tang E, et al. Fontan hemodynamics from 100 patient-specific cardiac magnetic resonance studies : A computational fluid dynamics analysis. 148(4). doi:10.1016/j.jtcvs.2013.11.060
17. Yang W, Chan FP, Reddy VM, Marsden AL, Feinstein JA. Flow simulations and validation for the first cohort of patients undergoing the Y-graft Fontan procedure. *J Thorac Cardiovasc Surg*. 2015;149(1):247-255. doi:10.1016/j.jtcvs.2014.08.069
18. Dasi LP, Whitehead K, Pekkan K, et al. Pulmonary hepatic flow distribution in total cavopulmonary connections: extracardiac versus intracardiac. *J Thorac Cardiovasc Surg*. 2011;141(1):207-214. doi:10.1016/j.jtcvs.2010.06.009
19. Trusty PM, Restrepo M, Kanter KR, Yoganathan AP, Fogel MA, Slesnick TC. A pulsatile hemodynamic evaluation of the commercially available bifurcated Y-graft Fontan modification and comparison with the lateral tunnel and extracardiac conduits. *J Thorac Cardiovasc Surg*. 2016;151(6):1529-1536. doi:10.1016/j.jtcvs.2016.03.019
20. Yang W, Feinstein JA, Shadden SC, Vignon-Clementel IE, Marsden ALA. Optimization of a Y-Graft Design for Improved Hepatic Flow Distribution in the Fontan Circulation. *J Biomech Eng*. 2013;135(January):1-12. doi:10.1115/1.4023089
21. Tang E, Restrepo M, Haggerty CM, et al. Geometric characterization of patient-specific total cavopulmonary connections and its relationship to hemodynamics. *JACC Cardiovasc Imaging*. 2014;7(3):215-224. doi:10.1016/j.jcmg.2013.12.010

22. Tang E, Wei ZA, Trusty PM, et al. The effect of respiration-driven flow waveforms on hemodynamic metrics used in Fontan surgical planning. *J Biomech*. 2019;82:87-95. doi:10.1016/j.jbiomech.2018.10.013
23. Hjortdal VE, Emmertsen K, Stenbog E, et al. Effects of exercise and respiration on blood flow in total cavopulmonary connection: a real-time magnetic resonance flow study. *Circulation*. 2003;108(10):1227-1231. doi:10.1161/01.CIR.0000087406.27922.6B
24. Hsia T-YY, Khambadkone S, Redington AN, Migliavacca F, Deanfield JE, de Leval MR. Effects of respiration and gravity on infradiaphragmatic venous flow in normal and Fontan patients. *Circulation*. 2000;102(19 Suppl 3):III148-53. doi:10.1161/01.cir.102.suppl_3.iii-148
25. Fogel MA, Weinberg PM, Hoydu A, et al. The nature of flow in the systemic venous pathway measured by magnetic resonance blood tagging in patients having the Fontan operation. *J Thorac Cardiovasc Surg*. 1997;114(6):1032-1041. doi:10.1016/S0022-5223(97)70017-5
26. Gabbert DD, Hart C, Jerosch-Herold M, et al. Heart beat but not respiration is the main driving force of the systemic venous return in the Fontan circulation. *Sci Rep*. 2019;9(1):2034. doi:10.1038/s41598-019-38848-5
27. Wei Z, Whitehead KK, Khiabani RH, et al. Respiratory Effects on Fontan Circulation During Rest and Exercise Using Real-Time Cardiac Magnetic Resonance Imaging. *Ann Thorac Surg*. 2016;101(5):1818-1825. doi:10.1016/j.athoracsur.2015.11.011
28. Körperich H, Müller K, Barth P, et al. Differentiation of Impaired From Preserved Hemodynamics in Patients With Fontan Circulation Using Real-time Phase-velocity Cardiovascular Magnetic Resonance. *J Thorac Imaging*. 2017;32(3):159-168. doi:10.1097/RTI.0000000000000261
29. Korperich H, Barth P, Gieseke J, et al. Impact of respiration on stroke volumes in paediatric controls and in patients after Fontan procedure assessed by MR real-time phase-velocity mapping. *Eur Heart J Cardiovasc Imaging*. 2015;16(2):198-209. doi:10.1093/ehjci/jeu179
30. Ha KS, Choi JY, Jung JW, Kim NK. Impact of Flow Differentials According to Cardiac and Respiratory Cycles on Three Types of Fontan Operation. *Pediatr Cardiol*. 2018;39(6):1144-1155. doi:10.1007/s00246-018-1872-1
31. Ha KS, Choi JY, Jung SY, Park HK. Characterization of Flow Efficiency, Pulsatility, and Respiratory Variability in Different Types of Fontan Circuits Using Quantitative Parameters. *Yonsei Med J*. 2019;60(1):56-64. doi:10.3349/ymj.2019.60.1.56
32. Vukicevic M, Chiulli JA, Conover T, et al. Mock circulatory system of the Fontan circulation to study respiration effects on venous flow behavior. *ASAIO J*. 2013;59(3):253-260. doi:10.1097/MAT.0b013e318288a2ab
33. Vukicevic M, Conover T, Jaeggli M, et al. Control of respiration-driven retrograde flow in the subdiaphragmatic venous return of the Fontan circulation. *ASAIO J*. 2014;60(4):391-399. doi:10.1097/MAT.0000000000000093
34. Hsia TY, Khambadkone S, Deanfield JE, Taylor JFN, Migliavacca F, De Leval MR. Subdiaphragmatic venous hemodynamics in the Fontan circulation. *J Thorac Cardiovasc Surg*. 2001;121(3):436-447. doi:10.1067/mtc.2001.112527
35. Hsia T-YY, Khambadkone S, Redington AN, de Leval MR. Effect of fenestration on the sub-diaphragmatic venous hemodynamics in the total-cavopulmonary connection. *Eur J Cardiothorac Surg*. 2001;19(6):785-792. doi:10.1016/s1010-7940(01)00705-9
36. Hsia T-Y, Khambadkone S, Bradley SM, de Leval MR. Subdiaphragmatic venous hemodynamics in patients with biventricular and Fontan circulation after diaphragm plication. *J Thorac Cardiovasc Surg*. 2007;134(6):1397-1405; discussion 1405. doi:10.1016/j.jtcvs.2007.07.044
37. Korperich H, Muller K, Barth P, et al. Differentiation of Impaired From Preserved Hemodynamics in Patients With Fontan Circulation Using Real-time Phase-velocity Cardiovascular Magnetic Resonance. *J Thorac Imaging*. 2017;32(3):159-168. doi:10.1097/RTI.0000000000000261
38. Rutkowski DR, Barton G, Francois CJ, et al. Analysis of cavopulmonary and cardiac flow characteristics in fontan Patients: Comparison with healthy volunteers. *J Magn Reson Imaging*. 2019;49(6):1786-1799. doi:10.1002/jmri.26583
39. Hjortdal VE, Christensen TD, Larsen SH, Emmertsen K, Pedersen EM. Caval blood flow during supine exercise in normal and Fontan patients. *Ann Thorac Surg*. 2008;85(2):599-603. doi:10.1016/j.athoracsur.2007.08.062
40. Cordina RL, O'Meagher S, Karmali A, et al. Resistance training improves cardiac output, exercise capacity and tolerance to positive airway pressure in Fontan physiology. *Int J Cardiol*. 2013;168(2):780-788. doi:10.1016/j.ijcard.2012.10.012
41. Kaulitz R, Luhmer I, Kallfelz HC. Pulsed Doppler echocardiographic assessment of patterns of venous flow after the modified Fontan operation: potential clinical implications. *Cardiol Young*. 1998;8(1):54-62. doi:10.1017/s1047951100004637

42. Gabbert DD, Hart C, Jerosch-Herold M, et al. Heart beat but not respiration is the main driving force of the systemic venous return in the Fontan circulation. *Sci Rep*. 2019;9(1):2034. doi:10.1038/s41598-019-38848-5
43. Grossman P, Janssen KHL, Vaitl D, Division. NATOSA. *Cardiorespiratory and Cardiosomatic Psychophysiology*. New York SE - viii, 368 pages : illustrations ; 26 cm.: Plenum Press; 1986.
44. Dyverfeldt P, Bissell M, Barker AJ, et al. 4D flow cardiovascular magnetic resonance consensus statement. *J Cardiovasc Magn Reson*. 2015;17(1):72. doi:10.1186/s12968-015-0174-5
45. Allan PLP, Baxter GM, Weston MJTA-TT-. Clinical ultrasound. LK - https://tudelft.on.worldcat.org/oclc/710978719. 2011. http://www.clinicalkey.com/dura/browse/bookChapter/3-s2.0-C20101663912.
46. Gill RW. Measurement of blood flow by ultrasound: Accuracy and sources of error. *Ultrasound Med Biol*. 1985;11(4):625-641. doi:10.1016/0301-5629(85)90035-3
47. Kaulitz R, Luhmer I, Kallfelz HC. Pulsed Doppler echocardiographic assessment of patterns of venous flow after the modified Fontan operation: potential clinical implications. *Cardiol Young*. 1998;8(1):54-62. doi:10.1017/s1047951100004637
48. Kaulitz R, Bergman P, Luhmer I, Paul T, Hausdorf G. Instantaneous pressure-flow velocity relations of systemic venous return in patients with univentricular circulation. *Heart*. 1999;82(3):294-299. doi:10.1136/hrt.82.3.294
49. Park MK. *Pediatric Cardiology*. 5th editio.; 2008.
50. Senzaki H, Masutani S, Ishido H, et al. Cardiac Rest and Reserve Function in Patients With Fontan Circulation. *J Am Coll Cardiol*. 2006;47(12):2528-2535. doi:10.1016/j.jacc.2006.03.022
51. Szabo G, Buhmann V, Graf A, et al. Ventricular energetics after the Fontan operation: contractility-afterload mismatch. *J Thorac Cardiovasc Surg*. 2003;125(5):1061-1069. doi:10.1067/mtc.2003.405
52. Sundareswaran KS, Kanter KR, Kitajima HD, et al. Impaired power output and cardiac index with hypoplastic left heart syndrome: a magnetic resonance imaging study. *Ann Thorac Surg*. 2006;82(4):1267. doi:10.1016/j.athoracsur.2006.05.020
53. Elger D, Lebret B, Crowe C, Roberson J. *Engineering Fluid Mechanics*. eleventh e. WILEY; 2013.
54. Seo T, Schachter L, Barakat A. Computational Study of Fluid Mechanical Disturbance Induced by Endovascular Stents. 2005;33(4):444-456. doi:10.1007/s10439-005-2499-y
55. Siebert MW, Fodor PS. Newtonian and Non-Newtonian Blood Flow over a Backward-Facing Step – A Case Study. *Excerpt from Proc COMSOL Conf 2009 Bost*. 2009:5.
56. Bhaskaran R, Collins L. *Introduction to CFD Basics*.
57. van Bakel TMJJ, Lau KD, Hirsch-Romano J, Trimarchi S, Dorfman AL, Figueroa CA. Patient-Specific Modeling of Hemodynamics: Supporting Surgical Planning in a Fontan Circulation Correction. *J Cardiovasc Transl Res*. 2018;11(2):145-155. doi:10.1007/s12265-017-9781-x
58. VMTK tutorials. http://www.vmtk.org/tutorials/. Accessed July 21, 2020.
59. Woodward P, Freimarck R. *MRI for Technologists*. (McGraw-Hill I, ed.).; 1995.
60. Schubert T, Bieri O, Pansini M, Stippich C, Santini F. Peak velocity measurements in tortuous arteries with phase contrast magnetic resonance imaging: The effect of multidirectional velocity encoding. *Invest Radiol*. 2014;49(4):189-194. doi:10.1097/RLI.0000000000000013
61. Bollache E, van Ooij P, Powell A, Carr J, Markl M, Barker AJ. Comparison of 4D flow and 2D velocity-encoded phase contrast MRI sequences for the evaluation of aortic hemodynamics. *Int J Cardiovasc Imaging*. 2016;32(10):1529-1541. doi:10.1007/s10554-016-0938-5
62. Markl M, Schnell S, Wu C, et al. Advanced flow MRI: emerging techniques and applications. *Clin Radiol*. 2016;71(8):779-795. doi:10.1016/j.crad.2016.01.011
63. Mushabbar AS. *Basic Principles of Cardiovascular MRI*.; 2015.
64. Nacif MS, Zavodni A, Kawel N, Choi EY, Lima JAC, Bluemke DA. Cardiac magnetic resonance imaging and its electrocardiographs (ECG): Tips and tricks. *Int J Cardiovasc Imaging*. 2012;28(6):1465-1475. doi:10.1007/s10554-011-9957-4
65. Dyverfeldt P, Ebbers T. Comparison of respiratory motion suppression techniques for 4D flow MRI. *Magn Reson Med*. 2018;78:1877-1882. doi:10.1002/mrm.26574
66. Van Ooij P, Semaan E, Schnell S, et al. Improved Respiratory Navigator Gating for Thoracic 4D flow MRI. doi:10.1016/j.mri.2015.04.008
67. Bogaert J, Dymarkowski S, Taylor AM. *Clinical Cardiac MRI*.; 2005.
68. Akçakaya M, Gulaka P, Basha TA, Ngo LH, Manning WJ, Nezafat R. Free-breathing phase contrast MRI with near 100% respiratory navigator efficiency using k-space-dependent respiratory gating. *Magn Reson Med*. 2014;71(6):2172-2179. doi:10.1002/mrm.24874
69. de Zélicourt DA, Marsden A, Fogel MA, Yoganathan AP. Imaging and patient-specific simulations for the Fontan surgery: Current methodologies and clinical applications. *Prog Pediatr Cardiol*. 2010;30(1-2):31-44. doi:10.1016/j.ppedcard.2010.09.005

70. Haggerty CM, de Zelicourt DA, Restrepo M, et al. Comparing pre- and post-operative Fontan hemodynamic simulations: implications for the reliability of surgical planning. *Ann Biomed Eng*. 2012;40(12):2639-2651. doi:10.1007/s10439-012-0614-4
71. Marsden AL, Bernstein AJ, Reddy VM, et al. Evaluation of a novel Y-shaped extracardiac Fontan baffle using computational fluid dynamics. *J Thorac Cardiovasc Surg*. 2009;137(2):394-403.e2. doi:10.1016/j.jtcvs.2008.06.043
72. Trusty PM, Wei Z, Sales M, et al. Y-graft modification to the Fontan procedure: Increasingly balanced flow over time. *J Thorac Cardiovasc Surg*. July 2019. doi:10.1016/j.jtcvs.2019.06.063
73. Comsol. *Particle Tracing Module*.; 2012. www.comsol.com/support/knowledgebase. Accessed July 21, 2020.
74. ANSYS FLUENT 12.0 Theory Guide - 15.2.1 Equations of Motion for Particles. https://www.afs.enea.it/project/neptunius/docs/fluent/html/th/node241.htm. Accessed July 21, 2020.
75. Benjan A. *Convection Heat Transfer*. (Wiley, ed.).; 2003. https://books.google.nl/books?hl=nl&lr=&id=9yC91-gpU8sC&oi=fnd&pg=PT7&dq=+Bejan+A+(2004).+Convection+Heat+Transfer.&ots=fyLjvODP0H&sig=FgqpQeu9ISl32_xNRRk8cfCJXGU&redir_esc=y#v=onepage&q=Bejan A (2004). Convection Heat Transfer.&f=false. Accessed July 21, 2020.
76. Funck C, Laun FB, Wetscherek A. Characterization of the Diffusion Coefficient of Blood. 2018. doi:10.1002/mrm.26919
77. Yushkevich PA, Piven J, Hazlett HC, et al. User-guided 3D active contour segmentation of anatomical structures: Significantly improved efficiency and reliability. *Neuroimage*. 2006;31(3):1116-1128. doi:10.1016/j.neuroimage.2006.01.015
78. Antiga L, Piccinelli M, Botti L, Ene-Iordache B, Remuzzi A, Steinman DA. An image-based modeling framework for patient-specific computational hemodynamics. *Med Biol Eng Comput*. 2008;46(11):1097-1112. doi:10.1007/s11517-008-0420-1
79. Wei ZA, Huddleston C, Trusty PM, et al. Analysis of Inlet Velocity Profiles in Numerical Assessment of Fontan Hemodynamics. *Ann Biomed Eng*. 2019. doi:10.1007/s10439-019-02307-z
80. Wei Z, Singh-Gryzbon S, Trusty PM, et al. Non-Newtonian Effects on Patient-Specific Modeling of Fontan Hemodynamics. *Ann Biomed Eng*. May 2020:1-14. doi:10.1007/s10439-020-02527-8
81. bulletin MP-E, 2004 undefined. Flow simulation using control volumes of arbitrary polyhedral shape.
82. Balafas G. Chair for Computation in Engineering Polyhedral Mesh Generation for CFD-Analysis of Complex Structures Georgios Balafas Master ' s thesis for the Master of Science program Computational Mechanics. 2014:1-78.
83. Corno AF, Owen MJ, Cangiani A, Hall EJCC, Rona A. Physiological Fontan Procedure. *Front Pediatr*. 2019;7(MAY):196. doi:10.3389/fped.2019.00196
84. Spiegel M, Redel T, Zhang JJ, et al. Tetrahedral vs. polyhedral mesh size evaluation on flow velocity and wall shear stress for cerebral hemodynamic simulation. *Comput Methods Biomech Biomed Engin*. 2011;14(1):9-22. doi:10.1080/10255842.2010.518565
85. Yang W, Feinstein JA, Marsden AL. Constrained optimization of an idealized Y-shaped baffle for the Fontan surgery at rest and exercise. *Comput Methods Appl Mech Eng*. 2010;199(33-36):2135-2149. doi:10.1016/j.cma.2010.03.012
86. Long CC, Hsu M-C, Bazilevs Y, Feinstein JA, Marsden AL. Fluid-structure interaction simulations of the Fontan procedure using variable wall properties. *Int j numer method biomed eng*. 2012;28(5):513-527. doi:10.1002/cnm.1485
87. Yang W, Vignon-Clementel IE, Troianowski G, Reddy VM, Feinstein JA, Marsden AL. Hepatic blood flow distribution and performance in conventional and novel Y-graft Fontan geometries: A case series computational fluid dynamics study. *J Thorac Cardiovasc Surg*. 2012;143(5):1086-1097. doi:10.1016/j.jtcvs.2011.06.042
88. McElhinney DB, Kreutzer J, Lang P, Mayer JEJ, del Nido PJ, Lock JE. Incorporation of the hepatic veins into the cavopulmonary circulation in patients with heterotaxy and pulmonary arteriovenous malformations after a Kawashima procedure. *Ann Thorac Surg*. 2005;80(5):1597-1603. doi:10.1016/j.athoracsur.2005.05.101
89. Sundareswaran KS, de Zélicourt D, Sharma S, et al. Correction of Pulmonary Arteriovenous Malformation Using Image-Based Surgical Planning. *JACC Cardiovasc Imaging*. 2009;2(8):1024-1030. doi:10.1016/j.jcmg.2009.03.019
90. Wei ZA, Trusty PM, Tree M, et al. Can time-averaged flow boundary conditions be used to meet the clinical timeline for Fontan surgical planning? *J Biomech*. 2017;50:172-179. doi:10.1016/j.jbiomech.2016.11.025
91. Ota H, Takase K, Rikimaru H, et al. Quantitative vascular measurements in arterial occlusive disease. *Radiographics*. 2005;25(5):1141-1158. doi:10.1148/rg.255055014

92. Rijnberg FM, Elbaz MSMM, Westenberg JJMM, et al. Four-dimensional flow magnetic resonance imaging-derived blood flow energetics of the inferior vena cava-to-extracardiac conduit junction in Fontan patients. *Eur J Cardiothorac Surg*. 2019;55(6):1202-1210. doi:10.1093/ejcts/ezy426
93. Khiabani RH, Whitehead KK, Han D, et al. Exercise capacity in single-ventricle patients after Fontan correlates with haemodynamic energy loss in TCPC. *Heart*. 2015;101(2):139-143. doi:10.1136/heartjnl-2014-306337
94. Hjortdal VE, Emmertsen K, Stenbog E, et al. Effects of exercise and respiration on blood flow in total cavopulmonary connection: a real-time magnetic resonance flow study. *Circulation*. 2003;108(10):1227-1231. doi:10.1161/01.CIR.0000087406.27922.6B
95. Owen B, Bojdo N, Jivkov A, Keavney B, Revell A. Structural modelling of the cardiovascular system. *Biomech Model Mechanobiol*. 2018;17(5):1217-1242. doi:10.1007/s10237-018-1024-9
96. Fadel BM, Alkalbani A, Husain A, Dahdouh Z, Di Salvo G. Respiratory hemodynamics in the hepatic veins - Normal pattern. *Echocardiography*. 2015;32(3):585-588. doi:10.1111/echo.12744
97. Ben-Tal A, Shamailov SS, Paton JFR. Evaluating the physiological significance of respiratory sinus arrhythmia: Looking beyond ventilation-perfusion efficiency. *J Physiol*. 2012;590(8):1989-2008. doi:10.1113/jphysiol.2011.222422
98. Truesdell RA, Bartsch JW, Buranda T, Sklar LA, Mammoli AA. Direct measurement of mixing quality in a pulsatile flow micromixer. *Exp Fluids*. 2005;39(5):819-827. doi:10.1007/s00348-005-0015-7
99. Baretta A, Corsini C, Marsden AL, et al. Respiratory effects on hemodynamics in patient-specific CFD models of the Fontan circulation under exercise conditions. *Eur J Mech B/Fluids*. 2012;35:61-69. doi:10.1016/j.euromechflu.2012.01.012
100. Cibis M, Jarvis K, Markl M, et al. The effect of resolution on viscous dissipation measured with 4D flow MRI in patients with Fontan circulation: Evaluation using computational fluid dynamics. *J Biomech*. 2016;48(12):2984-2989. doi:10.1016/j.jbiomech.2015.07.039.The
101. Bossers SSMM, Cibis M, Gijsen FJ, et al. Computational fluid dynamics in Fontan patients to evaluate power loss during simulated exercise. *Heart*. 2014;100(9):696-701. doi:10.1136/heartjnl-2013-304969
102. Marsden AL, Vignon-Clementel IE, Chan FP, Feinstein JA, Taylor CA. Effects of exercise and respiration on hemodynamic efficiency in CFD simulations of the total cavopulmonary connection. *Ann Biomed Eng*. 2007;35(2):250-263. doi:10.1007/s10439-006-9224-3

Supplement

A. Example of user defined function for IVC

```
/*********************************************************************/
/* Unsteady_parabolic velocity profile
*/
/* UDFs for specifying time dependent, parabolic velocity profile boundary condition
*/
/*********************************************************************/
#include "udf.h"

DEFINE_PROFILE(IVC_unsteady,thread,position)
{
real A,Q;
real x,y,z;
real posvec[ND_ND]; /* this will hold the position vector */
real x0,y0,z0;
real vmean,vmax;
real pi,r,r2,w,T;
real a0,a1,b1,a2,b2,a3,b3,a4,b4,a5,b5,a6,b6,a7,b7,a8,b8;/*Fourier coeffiecients*/
real flow_time;
face_t f;
f=0;
pi= 3.14159265358979;
#if !RP_HOST /*SERIAL or NODE*/
flow_time = RP_Get_Real("flow-time");

/*************************************************************/
/* CASE SPECIFIC PARAMETERS
MAKE SURE TO ADAPT TO THE CURRENT CASE */
   A = 434.675903e-6; /* inlet area (m^3) */
   x0 = 26.0896560452961e-3; /* x coordinate of inlet center */
   y0 = -51.4629509276748e-3; /* y coordinate of inlet center */
   z0 = -104.2060524545644e-3; /* z coordinate of inlet center */
/*************************************************************/

/*Fourier series, order 8*/

        a0 = 3.433721e-5;
        a1 = 3.743449e-6;
        b1 = -8.804122e-7;
        a2 = -2.739592e-6;
        b2 = -4.780673e-7;
        a3 = 6.527257e-7;
        b3 = 3.247201e-7;
        a4 = -7.809801e-8;
```

```
        b4 = -9.915715e-8;
        a5 = 9.976531e-7;
        b5 = -7.600093e-7;
        a6 = -1.764704e-6;
        b6 = -7.900711e-7;
        a7 = -2.819482e-7;
        b7 = -3.447752e-7;
        a8 = -3.445331e-7;
        b8 = -3.041645e-7;

        w = 2.137490e+0;

Q = a0 + a1*cos(flow_time*w) + b1*sin(flow_time*w) +a2*cos(2*flow_time*w) +
        b2*sin(2*flow_time*w) +a3*cos(3*flow_time*w) + b3*sin(3*flow_time*w)
        +a4*cos(4*flow_time*w) + b4*sin(4*flow_time*w) +a5*cos(5*flow_time*w) +
        b5*sin(5*flow_time*w) +a6*cos(6*flow_time*w) + b6*sin(6*flow_time*w)
        +a7*cos(7*flow_time*w) + b7*sin(7*flow_time*w) +a8*cos(8*flow_time*w) +
        b8*sin(8*flow_time*w);
vmean = Q/A;
vmax = 2*vmean;
r = sqrt(A/pi);
r2 = (pow((r),2));

/* PARABOLOID-SHAPED VELOCITY PROFILE */
begin_f_loop (f,thread)
      {
        F_CENTROID(posvec,f,thread);
        x=posvec[0];
        y=posvec[1];
        z=posvec[2];


        F_PROFILE(f,thread,position)= - (vmax/r2)*(  (pow((x-x0),2))+(pow((y-
        y0),2))+(pow((z-z0),2))  ) + vmax;

      }
   end_f_loop(f,thread)


#endif/*!RP_HOST*/

}
```

B. Additional figures of part B1

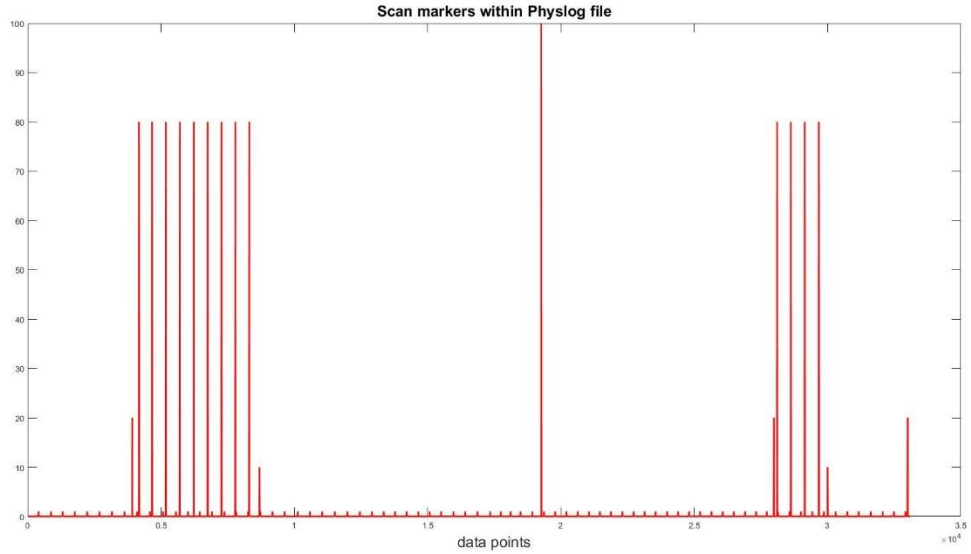

Figure 53: Scan markers within Physlog file. Scan marker equal to 100 is the start marker. Scan marker equal to 20 is the stop marker

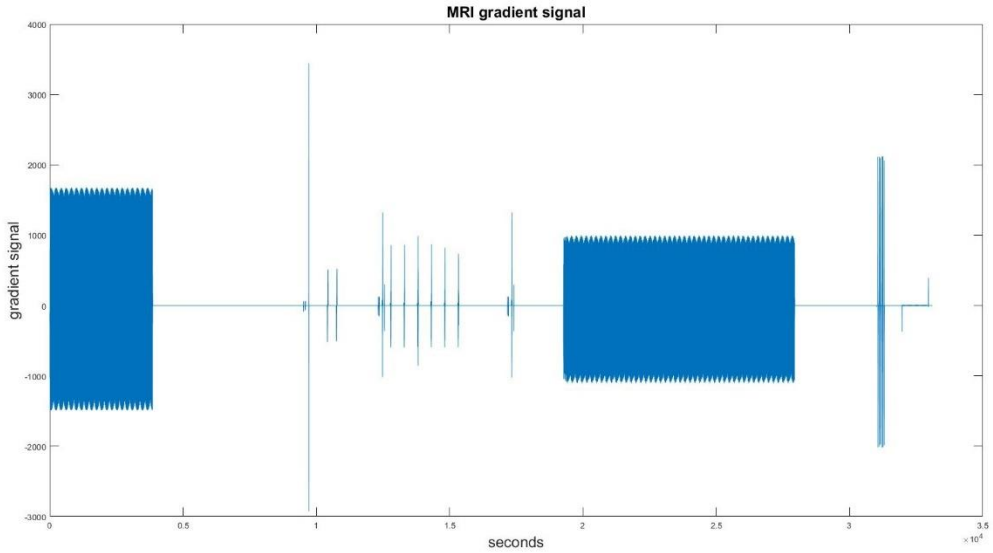

Figure 54: MRI gradient signal within Physlog file

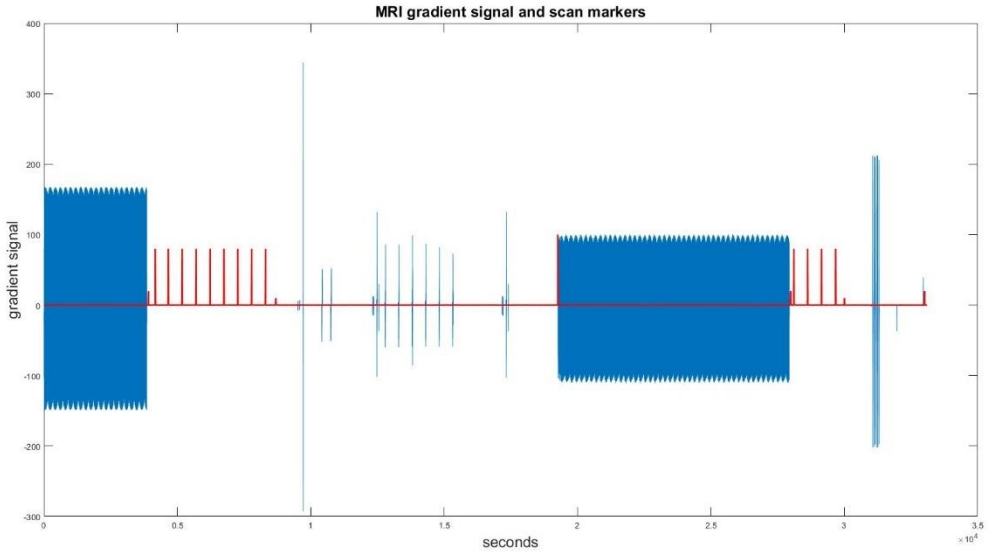

Figure 55: MRI gradient signal and scan markers within Physlog file in one figure

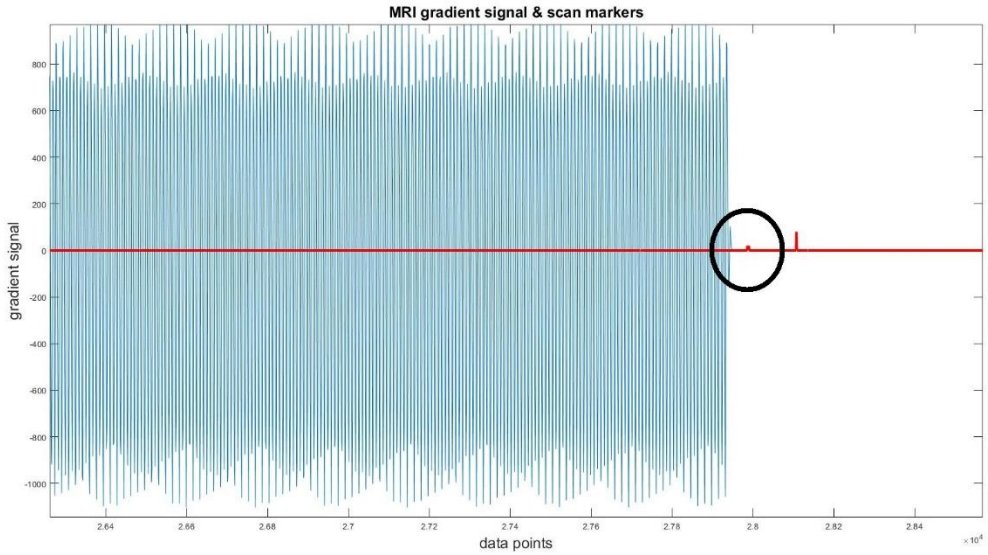

Figure 56: Close-up of MRI gradient signal and stop marker identified with the black circle. As you can see, the stop-marker does not fully match the end of the MRI gradient. Therefore, start- and stop-markers were not accurate enough to extract the respiratory waveform.

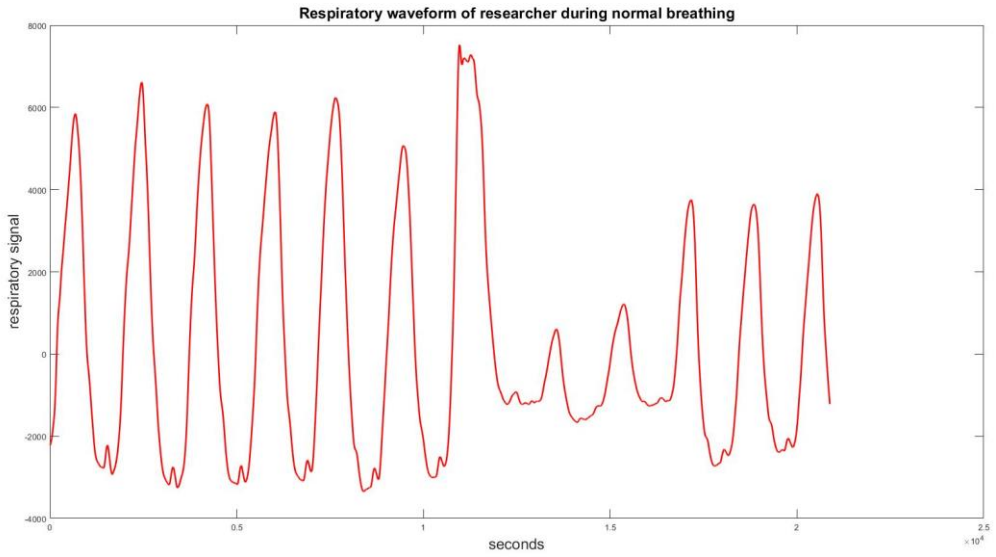

Figure 57: Respiratory waveform of a researcher of our group during normal breathing. As you can see, there is a short drift period during expiration

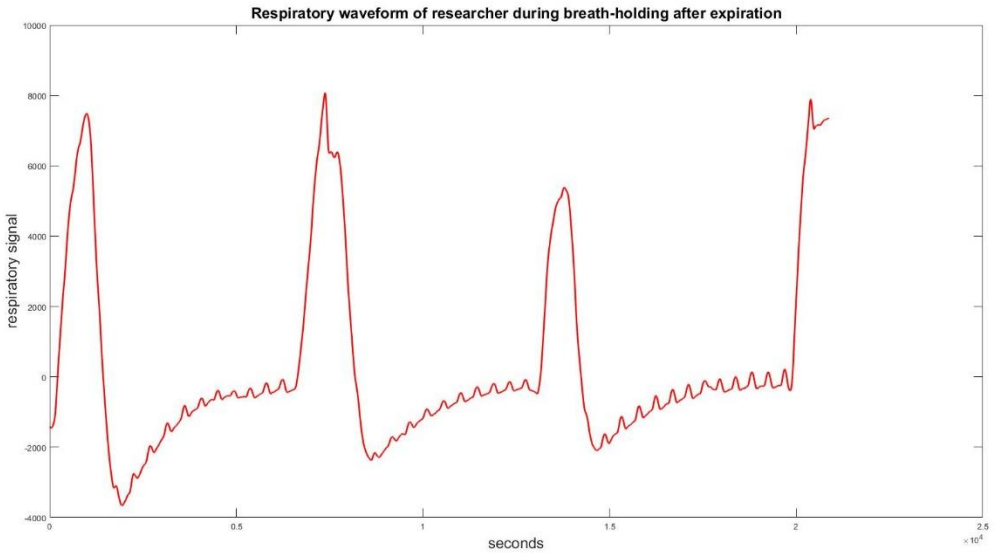

Figure 58: Respiratory waveform of a researcher of our group during breath-holding after expiration. As you can see, the expiratory drift period increases compared to normal breathing in figure 34. Therefore, we concluded that expiration indeed could cause a drift period in the respiratory signal

C. MATLAB script for finding the different respiratory cycles on the respiratory waveform

```
clear all
clc

%% %Finding respiration curve and ecg curve on the basis of gz MRI GRADIENT
fname =
E:\MASTERTHESISPROJECT\MATLABfiles\CASE1\Tunnel\SCANPHYSLOG20190116184604_t
unnel.log'
DATA =read_physio_SLF_nontrigdata_SW(fname) % Reading PHYSLOG FILE


% DATA marker 100 is start-marker real-time PC-MRI scan
b= find(DATA.mark(:)== 100,1,'first')

% DATA marker  20 is stop-marker real-time PC-MRI scan
c= find(DATA.mark(:)==20)

ix=find(c>b,1,'first')    % Searching first start-marker
d=c(ix)                   % d is index of first stop-marker after start
marker

base=DATA(:);             % Creating new data structure named base
base.gz(1:b,:) = 0;       % Searching for MRI gradient
base.gz(d:end,:)= 0;
r=find(base.gz(:)~= 0,1,'first')
s=find(base.gz(:)~= 0,1,'last')

respiration=base.resp(r:s)  % respiratory waveform signal

%plot Respiratory Curve
figure(1)
plot(respiration,'linewidth',2)
title('Respiration Curve')

freq=1/496;
duration_scan=freq*length(respiration)

%% %% Smoothing curve
% smooth function does not work on int32 data file, so you need to convert

K = cast(respiration,'single');     % convert to single file
F=1:length(respiration)
Time_respiration=F.*freq

Respiration_smooth = smooth(Time_respiration,K,0.05,'loess')
plot(Time_respiration, Respiration_smooth,'r','linewidth',2)
T=cast(Respiration_smooth,'single')
title('Respiratory waveform of Case 1', 'Fontsize', 16)
xlabel('Seconds', 'Fontsize', 16)
ylabel('Respiratory signal', 'Fontsize', 16)


%% First and second serivative of smooth respiration curve
% first derivative
dydx=gradient(Respiration_smooth(:))./gradient(Time_respiration(:))
```

```
% second derivative
dydx2=gradient(dydx(:))./gradient(Time_respiration(:))

%plot first and second derivative
p1 = plot(Time_respiration,Respiration_smooth,'r','linewidth',2)
hold on
p2 = plot(Time_respiration, dydx./10,'b','linewidth',2)  %/10 for plotting
hold on
p3 = plot(Time_respiration, dydx2./50,'g','linewidth',2) %/50 for plotting

title('Respiratory waveform and its first and second derivative - Case 1',
'Fontsize',16)
xlabel('Seconds', 'Fontsize', 16)
ylabel('Respiratory signal', 'Fontsize', 16)
hline = refline(0, 0);
hline.Color = 'k'
legend([p1 p2 p3], {'Repiratory waveform', 'First derivative', 'Second
derivative'},'Fontsize',18)

%finding 2nd derivative equal to zero: inflection points of respiratory
curve
m=linspace(0,length(dydx2),1)

for N=2:length(dydx2)
    if sign(dydx2(N-1))*sign(dydx2(N))~= 1
        m(N)=1
    elseif sign(dydx2(N-1))*sign(dydx2(N))== 1
        m(N)=0;
    end
end

points_zero=find(m(:)==1);     % find indices for which m = 1
val_d2_pzero=dydx2(points_zero) % find values of second derivative for m=1
val_d1_pzero=dydx(points_zero)% find values of first derivative for m=1

% find values second derivative (for m=1) positive and first derivative
(for m=1) almost negative < 0.2e4
d2_pos_d1_neg=find(val_d2_pzero>0 & val_d1_pzero <=0.2e4)
ind_final=points_zero(d2_pos_d1_neg)


%% %% Finding maximum and minima of Respiration curve

[PKS_max,LOCS_max]=findpeaks(Respiration_smooth,'MinPeakHeight',2000,
'MinPeakDistance', 1000);

[PKS_min,LOCS_min]=findpeaks(-Respiration_smooth, 'MinPeakDistance', 1000);

is=find(LOCS_max(:)>LOCS_min(1),1,'first')%Start respiratory cuve at
minimum
it=find(LOCS_min(:)<LOCS_max(end),1,'last')%End respiratory curve at
maximum

LOCS_max_fin=LOCS_max(is:end)
LOCS_min_fin=LOCS_min(1:it)
```

```
%% %% Checking if ind_final are within increasing part of Respiratory
curve.

HH=cell(length(LOCS_min_fin),1)
for N=1:length(LOCS_min_fin)  % finding increasing parts of respiratory
curve
HH{N} =LOCS_min_fin(N):1:LOCS_max_fin(N)-400
end

[v1, v2, v3, v4,v5] = deal(HH{:})
V_final=transpose([v1,v2,v3,v4,v5])


% Give "true" if the element in "V_final" is a member of "ind_final".
ind_final_increas.part = ismember(V_final, ind_final)

% Extract the elements of a at those indexes.
indexes = find(ind_final_increas.part)
Start_insp=V_final(ind_final_increas.part(:))

jump=diff(Start_insp)>500;          % if more drifts exist
index_jump=Start_insp([jump;true]);

%% Checking if we need LOCS_min_fin as start inspiration if no expiratory
drifts exist

ll=[]
for jj=1:5
tt=ismember(HH{jj}, index_jump)
if any(ismember(tt, 1))==1
    disp('YES')
    ll(jj)=0
else
    disp('no variable')
    ll(jj)=1
end
end

ll_T=transpose(ll)
ll_T_l=logical(ll_T)
LOCS_min_add=LOCS_min_fin([ll_T_l])

% Adding LOCS_min_add
Index_jump_2=[index_jump;LOCS_min_add]
Inspiration_start_idx=sort(Index_jump_2)%final indices of start inspiration
```

```
%% Checking Inspiration_start_idx by plotting
plot(Time_respiration, Respiration_smooth./100,'r', 'linewidth', 1)
%respiratory waveform divided by 100 --> allows plotting of flow and
respiratory curve in one figure

hold on
C = {'y','c','m','g','y',[.5 .6 .7],[.8 .2 .6]}
hline = refline(0, 0);
hline.Color = 'k'
hold on
for N=1: length(Inspiration_start_idx)-1
    hold on
    plot(Time_respiration((Inspiration_start_idx(N)+1):
Inspiration_start_idx(N+1)),
Respiration_smooth((Inspiration_start_idx(N)+1):
Inspiration_start_idx(N+1))./100,'Color',C{N}, 'linewidth',2)
end
hold on

plot(Time_respiration, Flow_tunnel_interpoleerd1,'b', 'linewidth', 1)
for N=1: length(Inspiration_start_idx)-1
    hold on
    plot(Time_respiration((Inspiration_start_idx(N)+1):
Inspiration_start_idx(N+1)),
Flow_tunnel_interpoleerd1((Inspiration_start_idx(N)+1):
Inspiration_start_idx(N+1)),'color',C{N}, 'linewidth',2)
end

title('Interpolated volumetric flow rate waveform and its corresponding
respiratory waveform - of Fontan tunnel Case 1','Fontsize', 18)
xlabel('seconds', 'Fontsize',18)
ylabel('Milliliter per second', 'Fontsize', 18)

legend({'Respiratory waveform','First respiratory cycle', 'Second
respiratory cycle', 'Third respiratory cycle', 'Fourth respiratory cycle',
'Volumetric flow rate waveform'}, 'Fontsize', 18)
```